

Modeling and Characterization of Fracture and Fluid Flow in Porous Media

THESIS SUBMITTED FOR THE DEGREE OF
DOCTOR OF PHILOSOPHY (SCIENCE)
IN PHYSICS

By

Ruhul Amin Ibne Haque



Post Graduate and Research Department of Physics
St. Xavier's College (Autonomous)
Kolkata
Affiliated to the University of Calcutta

2024

Certificate

I certify that the thesis entitled “**Modeling and Characterization of Fracture and Fluid Flow in Porous Media**” submitted by **Ruhul Amin Ibne Haque** for the degree of Doctor of Philosophy (Ph.D.) in Physics in the area of Soft Matter Physics is the record of research work carried out by him during the period from 12.11.2018 to 27.09.2024 under my guidance and supervision and that this work has not formed the basis for the award of any Degree, Diploma, Associateship, Fellowship, Titles in this University or any other University or other similar institution of Higher learning.

Overall similarity percentage : **8%**

Signature of Supervisor :

Signature of Ph.D Coordinator :

I dedicate this thesis to my loving parents.

Acknowledgements

First and foremost, I am deeply thankful to the almighty God for granting me the strength, patience, and wisdom needed to complete this research.

I am profoundly grateful to my supervisor, **Dr. Tapati Dutta**, for her unwavering guidance, insightful feedback, and constant encouragement throughout this journey. Her expertise has been invaluable at every stage, and I will always cherish the immense growth I've experienced under her mentorship. I also wish to extend my sincere thanks to my Research Advisory Committee (RAC) members, **Prof. Sujata Tarafdar** and **Prof. Parongama Sen**, whose thoughtful suggestions significantly enhanced the quality of this work.

A special thanks to **Dr. Shashwati Roy Majumder**, whose early guidance and encouragement were instrumental to the initial stages of this research, and to **Prof. Atish J. Mitra** for introducing me to key mathematical concepts that helped strengthen the theoretical foundation of my work.

I would also like to express my deep appreciation to my friends and colleagues at St. Xavier's College for their support. In particular, I am grateful to **Samiul Haque** and **Anamika Roy** for their collaboration and constant feedback, which helped shape the direction of this study.

I am also thankful to the University Grants Commission (UGC) for providing financial support through the JRF/SRF scholarships (UGC Ref. No. 1435/CSIR-UGC NET JUNE 2017), which made this research possible.

Finally, I owe my deepest gratitude to my family for their unwavering love and support. Their belief in me has been my greatest source of motivation and strength throughout this journey.

Abstract

This dissertation presents a comprehensive study of fracture networks in porous media and the polygonal patterns they form in various natural systems. Our approach utilizes a combination of mathematical modeling, simulation, and empirical analysis. A novel four-parameter map is introduced to characterize planar surface fracture networks, summarizing their topological and geometrical properties. This map classifies different materials by grouping them according to similar characteristics of their crack patterns. Columnar joint systems, crack networks in drying colloidal materials, and salt ridge mosaics are also explored on the basis of evolving crack patterns mapped as trajectories in a domain defined by the geometry and topology of the crack network. The dissertation proposes empirical relations between system energy and geometric parameters, demonstrating that many natural systems evolve toward energy minimization, often forming Voronoi-like structures. For 3-dimensional disordered porous materials, crack statistics and the dependence of micro-cracking behavior on elastic properties are analyzed. The analysis reveals two distinct cracking regimes and a power-law relation between critical strains. Additionally, the permeability of porous systems is shown to follow unique scaling relations with the Minkowski functionals, regardless of whether the system is ordered or disordered. These findings provide a deeper understanding of crack mechanics and material behavior across diverse natural systems.

Table of contents

List of figures	xv
List of tables	xxv
1 Introduction	1
1.1 Fracture Mechanics	1
1.1.1 Griffith's Theory	1
1.2 Patterns of Crack Networks	3
1.3 Fluid Flow in Fractured Media	3
1.4 Applications and Importance	4
1.5 Organization of the Thesis	4
2 Topology and Geometry of Fracture Networks	7
2.1 Introduction	7
2.2 Convex Planar Mosaics	8
2.2.1 Combinatorial Topology of Convex Planar Mosaics	8
2.2.2 Angular Defect D and the (n, v, D) Space	11
2.2.3 Isoperimetric Ratio λ and the (n, v, λ) Space	11
2.2.4 The Parameter Space of Quadruples (n, v, D, λ)	12
2.3 Geometric Simulations of Cracks	12
2.3.1 Gilbert Tessellation and Its Variations	12
2.3.2 Voronoi Tessellation	16
2.3.3 Iterative Cell Division	18
2.4 Real Crack Mosaics	19
2.5 Mapping the Topology of Simulated and Real Cracks on the (n, v) Plane	20
2.6 Features of the Crack Mosaics on the (n, v, D, λ) Space	21
2.7 Comparison Between Physical and Simulated Mosaics	21
2.8 Discussion	25

2.9	Conclusions	26
3	Columnar Joints	29
3.1	Introduction	29
3.1.1	Formation of Columnar Joints	31
3.2	Simulation of Columnar Joints	33
3.3	Energy Minimization and Evolving Columnar Joints	34
3.3.1	Geometrical Energy of Crack Planes	38
3.4	Results and Discussion	38
3.5	Conclusions	46
4	Voronoiness of Crack Patterns	49
4.1	Introduction	49
4.2	Theoretical Background	51
4.2.1	Quantification of Voronoi-ness	51
4.2.2	Construction of Voronoi Diagram From a Seed Scatter	52
4.2.3	Crack Evolution	53
4.3	Simulation of the Wetting-drying Process	54
4.4	Results and Discussion	57
4.4.1	Dynamic Progression of Crack Mosaics	58
4.4.2	Static Crack Mosaics	65
4.5	Conclusions	67
5	Simulation of Salt Playas	69
5.1	Introduction	69
5.2	Materials and Methods	70
5.2.1	The Simulation Model	73
5.3	Results and Discussion	77
5.3.1	System Energy and Voronoi-ness	84
5.4	Conclusions	85
6	Stress-Induced Fracture in Porous Systems	87
6.1	Introduction	87
6.2	Distinct Element Method	89
6.3	Structure Generation	92
6.4	Results and Discussion	93
6.4.1	Fracture in the Hexagonal Arrangement of Spheres	93

6.4.2	Fracture in Disordered Systems	94
6.5	Conclusions	99
7	Fluid Flow in Porous Media	101
7.1	Introduction	101
7.2	Porous Structure Generation	103
7.3	Geometric Characterization of Porous Medium	103
7.4	Fluid Transport	105
7.5	Results and Discussion	105
7.6	Conclusions	112
8	Summary and Future Directions	115
8.1	Future Directions	117
	References	119
	Appendix A Spring model and elasticity	133

List of figures

- 2.1 (a) Examples of regular nodes. (b) Examples of irregular nodes. (c) Presence of both regular and irregular nodes. (d) A, B, and C are typical polygons in a schematic mosaic; the nodes are marked by numbers 1 to 9, listing the nodes and vertices for every polygon, along with categorizing the mosaic’s nodes as either regular or irregular. 9
- 2.2 (a) The allowed (n, ν) domain of infinite convex planar mosaics, (b) Angular defect D is 1 for regular polygons and D decreases from 1 towards 0 as the polygons deviate from the regular one. (c) For a circle, $\lambda = 1$; and λ decreases from 1 towards 0 as the polygonal structures transform from shapes that are comparatively circular to needle-like forms. 10
- 2.3 The 4×5 matrix illustrates the Gilbert tessellation with a uniform seed distribution. The first four rows represent different selections of crack slopes: (1) random angles between 0° and 180° , (2) slopes aligned with the reference axes at 0° or 90° , (3) randomly chosen slopes from 0° , 45° , and 90° , and (4) randomly selected slopes within $0^\circ \pm 10^\circ$ or $90^\circ \pm 10^\circ$. The five columns display: (1) the crack mosaic, (2) the angular defect D_N histogram, (3) the histogram of the number of vertices in the polygons, (4) the crack length histogram, and (5) the polygon area histogram. 14
- 2.4 The 4×5 matrix illustrates the Gilbert tessellation with a normal seed distribution. Rows 1 to 4 correspond to four different selections of crack slopes: (1) random angles between 0° and 180° , (2) slopes aligned with the reference axes at 0° or 90° , (3) randomly chosen slopes from 0° , 45° , and 90° , and (4) randomly selected slopes within $0^\circ \pm 10^\circ$ and $90^\circ \pm 10^\circ$. Columns 1 to 5 display: (1) the crack mosaic, (2) the angular defect D_N histogram, (3) the polygon vertex count histogram, (4) the crack length histogram, and (5) the polygon area histogram. 15

2.5	The Gilbert tessellation with time-delayed crack initiation features: (a) a uniform distribution of initial cracks, and (b) a normal distribution of initial cracks.	16
2.6	The 2×4 matrix represents a Voronoi tessellation. Rows 1 and 2 correspond to uniform and normal seed distributions on the plane, respectively. Columns 1 to 4 display: (1) the crack mosaic, (2) the histogram of the angular defect D_N , (3) the histogram of polygon/tile areas (in arbitrary units), and (4) the histogram of the number of vertices for the polygons in the mosaic.	17
2.7	Crack mosaic generated through iterative cell division. Images (a), (b), and (c) correspond to the results after the 1 st , 4 th , and 8 th iterations, respectively. The newest cracks are highlighted with broken lines.	18
2.8	Measures of Crack Mosaic using Iterative Cell Division after 10 th iteration (a) Histogram of the angular defect D_N (b) Histogram of polygon/ tile area (c) Histogram of the number of vertices per polygon in the mosaic (d) Histogram of crack length.	19
2.9	The (n, v) data for real and simulated crack mosaics, with iso- p lines at $p = 0.3$ and $p = 0.5$ included as visual guides.	20
2.10	(a1) (n, v, D) data of real and simulated crack mosaics. (a2) Zoomed-in view of (n, v, D) data. (c1) (n, v, λ) data of real and simulated crack mosaics. (c2) Zoomed-in view of (n, v, λ) data. (b) Legends for (a1) and (a2) and (d) legends for (c1) and (c2)	23
2.11	Histogram of isoperimetric ratio λ for simulated crack mosaics: (a) Gilbert tessellations with random slopes, (b) slopes at 0° and 90° , (c) slopes at 0° , 45° , and 90° , (d) slopes at $0^\circ \pm 10^\circ$ and $90^\circ \pm 10^\circ$. For Voronoi tessellations, (e) uniform seed distribution, and (f) normal seed distribution. The average values of the λ parameter are presented in Tab. 2.1.	24
2.12	Histogram of isoperimetric ratio λ for real crack mosaics of: (a) TiO ₂ , (b) PDMS, (c) Laponite (pH 6.73), (d) Laponite (pH 13.45), (e) Tempered Glass, (f) Resin, (g) Corn starch, and (h) Mud cracks.	24
2.13	(a) Variation of isoperimetric ratio λ across different iteration stages in the cell division method. (b) Histogram of λ at the 10 th iteration step.	25
3.1	Columnar joint in Tsumekisaki Izu, Japan. Photo credit: hide. S [39]	30

- 3.2 (a) Convection flow cooling, represented by white arrows, occurs within the crack joints, while conduction cooling, shown by black arrows, takes place across the column's interior. The isotherms are indicated by dashed lines. *Figure adapted from [37]*. The red line illustrates the deviation of the growing crack toward the direction of the wider column. (b) A schematic diagram for estimating $d_{i(max)}$ in Eq. (3.1) is presented. The diagram represents a horizontal cross-section of adjacent columns meeting at a single point. Black circles depict the centroids of neighboring polygons surrounding the node, which is marked by a red circle. 32
- 3.3 (a) Simulated 3-dimensional columnar joints, with step-wise sections showing their time development. (b) Natural columnar joints located in Genbudo Geo-Park, Japan. (c) Time progression of several independent columns within the crack mesh. (d) The evolution of a single columnar joint, tracked from its initial polygonal shape (highlighted in green) to its final matured form (highlighted in red). 35
- 3.4 Characteristics of crack mosaic dynamics following Gilbert tessellation with uniform seed distribution. Variation in crack orientation with respect to the horizontal axis: (I) Random, (II) Parallel, (III) $\pm 10^\circ$, (IV) 45° and 90° . (a) Crack mosaic at the start ($t = 0$). (b) Crack mosaic at maturation. (c) Crack ped area distribution at $t = 0$, $t = 10$, and $t = 100$. (d) Distribution of average polygonal angle of crack ped at $t = 0$, $t = 10$, and $t = 100$. (e) Time development of average n , v , D , and λ . For figures in rows (c) and (d), green, red, and blue denote distributions at $t = 0$, $t = 10$, and $t = 100$, respectively. 39
- 3.5 Characteristics of crack mosaic dynamics following Gilbert tessellation with normal seed distribution. Variation in crack orientation with respect to the horizontal axis: (I) Random, (II) Parallel, (III) $\pm 10^\circ$, (IV) 45° and 90° . (a) Crack mosaic at the start ($t = 0$). (b) Crack mosaic at maturation. (c) Distribution of average polygonal angle of crack ped at $t = 0$, $t = 10$, and $t = 100$. (d) Time development of average n , v , D , and λ . For figures in row (c), green, red, and blue denote distributions at $t = 0$, $t = 10$, and $t = 100$, respectively. 40
- 3.6 Trajectory of the crack in the (n, v, D, λ) domain: Gilbert cracks with uniform seed distribution and crack orientation - (a) random (b) parallel (c) $\pm 10^\circ$ (d) 45° and 90° ; Gilbert cracks with normal seed distribution and crack orientation - (e) random (f) parallel (g) $\pm 10^\circ$ (h) 45° and 90° ; (i) Voronoi cracks. 42

3.7	Characteristics of crack mosaic dynamics following Voronoi tessellation with uniform seed distribution. (a) Mosaic at $t = 0$. (b) Mosaic at $t = 100$. (c) Time variation of the histogram of crack ped area. (d) Time variation of the histogram of the average internal angle of crack ped. (e) Time development of n , v , D , and λ	43
3.8	Power law fitting of (a) crack length, L and (b) λ	43
3.9	(a) Trajectory of energy E based on Eq. (3.5) for various initial mosaics. (b) Comparison of energy minimization trajectories using Eq. (3.2) and Eq. (3.5) for the initial mosaic generated with Gilbert tessellation, featuring a uniform seed distribution and random crack orientation.	44
3.10	(a) Plot of dE/dt against $d\lambda/dt$. (b) Comparison between the columnar joint pattern (dashed line) and the Voronoi mosaic (solid line) created from the centroids of matured columns. (c) Change in $\langle \Delta r \rangle$ over time t . (d) Geometric energy ε trajectory as described by Eq. (3.7).	45
4.1	A Voronoi diagram is the dual of a Delaunay triangulation: (a) The seeds used to create the Voronoi diagram, (b) The Delaunay triangulation formed by connecting the seeds, (c) Circumcircles around each triangle, ensuring no seed lies within the interior of any circumcircle. The red points represent the circumcenters of the triangles. (d) Connecting the circumcenters of triangles that share a common side results in the formation of the Voronoi diagram. . .	53
4.2	(a) Spring model used to simulate desiccation cracking. The vertices of the crack peds are represented by red circles, and the centroids of the peds are marked by blue circles. The natural spring length d_0 between the centroid (blue) and vertex (red) is indicated by an arrow. A red vertex experiences elastic forces from the surrounding polygons through the springs. After N desiccation steps, the vertex moves to a new position (orange circle) and remains connected to the polygon centroids by springs (shown as dotted lines) with new lengths d_N (also indicated by an arrow). (b) Initial crack network of a desiccation crack. (c) Final matured crack network pattern after repeated wetting-drying cycles. (d) Initial and final frequency distributions of the polygonal angles of crack peds. The final distribution shows a peak around 120° , marked by a blue dotted line.	55
4.3	Flow-chart of one complete wetting-drying cycle.	57

- 4.4 The trajectory of crack evolution under repeated wetting and drying cycles is shown in the (n, v, D, λ) domain. The green and red points represent the starting and ending positions of the crack mosaic's combinatorial trajectory, respectively. The positions of static crack mosaics for (i) Mud crack I, (ii) Mud crack II, and (iii) Honeycomb within the 4-tuple vector domain are also marked, as described in the legend. 58
- 4.5 Column I(a–c): The ratio of circles encompassing any seed, p , decreases with successive wetting-drying cycles. Column II(a–c): Variation in the Hausdorff Metric between the mud-crack pattern and the corresponding Voronoi diagram generated using the centroids. The metric decreases with wetting-drying cycles and stabilizes at a constant value of around 1.8. Column III(a–c): The Iso-perimetric ratio λ increases as the mud undergoes wetting-drying cycles, indicating that the peds become rounder with each cycle. In the first row (I(a)–III(a)), only the parameter 'a' is varied while the other parameters remain constant. In the second and third rows, the parameter 'b' and the number of desiccation time steps N per cycle are varied, respectively, with other parameters held constant. 60
- 4.6 (a) Reduction of elastic energy over successive wetting-drying cycles. (b) Distribution of linear stress within each polygon of the final mosaics. (c) Geometrical energy corresponding to various stress distributions within a polygon. (d) Normalized geometrical energies for different stress distributions converge onto a single curve. 62
- 4.7 (a) Change in Shannon (Voronoi) entropy over time t for a maturing crack mosaic. (b) Confirmation of Lewis' Law: the relationship between the average area A_v of a polygon with v sides and $(v - 2)$. (c) Confirmation of Aboav's Law: the variation in the average number of sides m_v of polygons adjacent to a v -sided polygon. 64
- 4.8 Verification of Voronoi-like patterns. Real mud-cracks: (a) Case I, with the crack network outlined in red. (b) Triangulation created by connecting centroids of adjacent polygons sharing a common edge. (c) Circumcircles drawn for each triangle, with red circles containing one or more centroids. (d) Case II of mud cracks. (e) Delaunay triangulation for the polygons. (f) Circumcircles for all triangles, showing no centroids inside the circles in this case. (g)–(i) illustrate the same schematic process for a honeycomb structure. 65

4.9	Measuring the Hausdorff Metric, d_H . (a) A real mud crack (solid black lines) is compared with the Voronoi diagram (dashed black lines) generated from the centroids of the polygons. The red arrow indicates the point of maximum deviation, which determines the Hausdorff Metric. (b) The Voronoi diagram aligns perfectly with the honeycomb structure, resulting in a Hausdorff Metric of zero.	66
5.1	Polygonal pattern formed by salt ridges at Salar de Uyuni, Bolivia. Photo credit: Anouchka Unel [111]	70
5.2	(a) Schematic illustration of a salt playa. The grey layer depicts a salt layer atop the clay surface. Polygonal salt ridges form along the edges of the polygonal cracks as saline water is transported from the subsurface water table through vertical crack channels. Red arrows indicate the direction of advection, while blue arrows represent the direction of evaporation flux. (b) Spring model for crack dynamics. Red dots signify the vertices of peds, and blue circles mark their centroids. The natural length d_0 of the springs connecting a centroid to a vertex is indicated by an arrow. A vertex (red) is connected via springs to the centroids of adjacent polygons to account for elastic forces. The updated position (green) of the vertex after one complete wetting-drying cycle is shown. Dotted springs have updated lengths d' , as indicated by arrows.	71
5.3	Flowchart of simulation.	77
5.4	(a) The shape evolution of an arbitrarily shaped polygon under cyclic wetting and drying, following the spring-network model, until it reaches maturation. (b) 3-D simulation of salt ridge patterns. Refer to supplemental video files for more details. (c) Experimental measurement of the angle of repose for a self-organized pile of wet NaCl salt (Tata Chemicals Ltd.), showing an angle of 58.5° . (d) A playa lake located in the Altiplano-Puna Plateau of the Andes. Adapted from Brooks[117].	78
5.5	Impact of evaporation-induced suction pressure on the salinity profile along the y-z plane of a typical crack channel after 2500 time-steps. Parameters $D = 0.5 \text{ cm}^2/\text{s}$ and $c_{in} = 0.1 \text{ gm/cc}$ are kept constant. Legends indicate the salinity range. Salinity profiles for (a) $P = 10 \text{ dyn/cm}^2$, $Ra = 18.3$; (b) $P = 15 \text{ dyn/cm}^2$, $Ra = 8.7$; (c) $P = 20 \text{ dyn/cm}^2$, $Ra = 6.1$	79

- 5.6 (a) Log-log plot showing the variation of τ_{cr} with P for different Δc values. The insets illustrate how the scale exponent $m_{\Delta c}$ and the y-axis intercept $n_{\Delta c}$ change with Δc . (b) Validation of the analytical relationship between τ_{cr} and Δc for varying P . The symbols indicate simulated data points, while the curves are derived from Eq. (5.12). (c) Plot of τ_{cr} versus D for various Δc values. The insets display the variation of the slope $m'_{\Delta c}$ and the y-axis intercept $n'_{\Delta c}$ with Δc . The color legend is the same as in (a). (d) Validation of the analytical relationship between τ_{cr} and Δc for varying D . The symbols represent simulated data points, and the curves are based on Eq. (5.18). 81
- 5.7 Effect of the model parameters P , D , and Δc on the crystal growth rate G versus dimensionless time τ , following crack maturation. The crystal growth rate G approaches a dynamic equilibrium value G_{eq} in each scenario. The variation of G_{eq} with each parameter is shown in the insets of the figures. (a) Effect of varying pressure P with constants $D = 0.1 \text{ cm}^2/\text{s}$ and $\Delta c = 0.2 \text{ gm/cc}$. (b) Effect of varying diffusion coefficient D with constants $P = 15 \text{ dyn/cm}^2$ and $\Delta c = 0.2 \text{ gm/cc}$. (c) Effect of varying Δc with constants $P = 15 \text{ dyn/cm}^2$ and $D = 0.1 \text{ cm}^2/\text{s}$ 83
- 5.8 (a) Change in system energy over time. (b) Changes in the Hausdorff metric between the salt ridge pattern and the corresponding Voronoi diagram during wetting-drying cycles. 85
- 6.1 Schematic diagram showing spherical grains constitute a porous system. The grains are cemented at their intersections. (b) Forces acting on particles in DEM. 90
- 6.2 (a) Material generated by hexagonal packing of monodispersed spheres with a radius of 0.036 cm. (b) 3-dimensional rectangular parallelepiped constructed from spheres with a log-normal distribution, mean radius of 0.04 cm, and standard deviation of 0.003 cm. 92
- 6.3 Snapshots of the material at different times under compressive loading. Stress on the particles is color-coded. 93
- 6.4 (a) Typical stress-strain behavior of the generated materials. The red bars represent the number of bonds broken. (b) Stress-strain curve for different Young modulus, Y . A higher Young modulus shows a steeper slope. 94
- 6.5 (a) Variation of the number of cracks N^{k_b} versus axial strain for different bond stiffness and constant bond strength σ_c . (b) Log-Log plot of strain at maximum crack number $N_{max}^{k_b}$ versus bond stiffness k_b . (c) Log-Log plot of strain at maximum crack number $N_{max}^{k_b}$ versus corresponding strain. 95

- 6.6 Crack statistics for constant spring threshold $\sigma_c = 100$ MPa, and variable bond stiffness constants $k_b = 50, 100, 200, 300, 600$. Values are in units of MPa m^{-1} .
 (a) Cumulative micro-cracks versus strain percentage. The dotted line is indicative of the transition between different cracking modes for $k_b = 300 \text{ MPa m}^{-1}$.
 (b) Variation of ε_{knee} with k_b follows a power law with exponent $m_{knee} = -0.397$
 (c) Variation of ε_{perc} with k_b follows a power law with exponent $m_{perc} = -0.294$ 96
- 6.7 Log-log plot of ε_{perc} versus ε_{knee} (a) For constant breaking threshold $\sigma_c = 100$ MPa and varying stiffness constant k_b . A power-law behavior is indicated with exponent $m = 0.739$. (b) For constant stiffness constant $k_b = 400 \text{ MPa m}^{-1}$ and varying breaking threshold σ_c . A power-law behavior is indicated with exponent $m = 0.721$ 97
- 6.8 Crack statistics for constant spring stiffness $k_b = 400$ MPa, and variable spring breaking thresholds $\sigma_c = 50, 100, 200, 400, 600, 800, 1000$. Values are in units of MPa. (a) Cumulative micro-cracks versus strain percentage. (b) Variation of ε'_{knee} with σ_c follows a power law with exponent $m'_{knee} = 0.274$ (c) Variation of ε'_{perc} with σ_c follows a power law with exponent $m'_{perc} = 0.206$ 98
- 7.1 3-dimensional porous structures generated using DEM. (a) Deterministic structure having cubic symmetry (b) Deterministic structure having hexagonal symmetry (c) Stochastic structure with particle size chosen from a log-normal distribution. (d) Stochastic structure with particle size chosen from a normal distribution. 106
- 7.2 Typical micro-geometric characteristic of 3-dimensional stochastic porous systems. Lognormal stochasticity is shown here. (a) Variation of 2-point correlation function $S_2(r)$ with r along principle axes. (b) Mean square displacement $\langle r^2 \rangle$ with time t shows subdiffusive behavior. 107
- 7.3 (a) Porous structure of a log-normal stochastic sample, (b) the system-spanning path through which a sphere of diameter l_c can move freely, (c) pressure distribution inside the porous space, and (d) steady-state velocity profile across the sample. The color legends provide value scales in CGS units. 108
- 7.4 (a) The log-log variation of permeability with A_c for the deterministic and stochastic 3-dimensional porous structures, (b) variation of permeability with porosity ϕ_0 , (c) the log-log variation of permeability with the Euler Characteristic χ , (d) the variation of permeability with the mean integral curvature. . . 109

-
- 7.5 (a) Variation of permeability k with F , a build-up function of the geometric invariants of the samples. (b) Variation of permeability k with F using regression shows a very good collapse on a single power-law scaling function irrespective of sample type. 110

List of tables

2.1	Measures of simulated and real crack mosaics	22
3.1	Values of α and β obtained from Eqs. (3.10) and (3.11) for the energy estimations.	45
4.1	Measures of Voronoi-ness and (n, v, D, λ) values for the static crack mosaics.	66

Chapter 1

Introduction

Fracture is a fundamental phenomenon in various disciplines, such as materials science, geomechanics, and structural engineering. It is a process of crack initiation and propagation in materials under stress. Understanding fractures is critical for predicting the failure of structures, optimizing resource extraction in petroleum engineering, and assessing natural hazards like earthquakes and landslides.

1.1 Fracture Mechanics

Fractures occur when the stress applied to a material exceeds its strength, separating the material into two or more parts. This phenomenon can be observed in both natural materials, such as rocks and minerals, and in engineered materials like metals, ceramics, and polymers.

1.1.1 Griffith's Theory

The systematic exploration of cracks commenced with the renowned Griffith theory[1]. This initial investigation has blossomed into a comprehensive discipline, complete with numerous books and reviews dedicated solely to its examination. [2–12]. When solid matter is stressed, the inherent elasticity of the solid tries to resist deformation. However, the system is often constrained by boundary conditions whereby it cannot release the internal strain and relax. It may also happen that the strain relaxation mechanism is slower than the straining rate. The plasticity of the material may be responsible for a permanent deformation in the solid, which raises its free energy G . Whatever the cause, if the strain energy crosses a critical threshold G_c characteristic of the solid, the solid releases the pent-up energy by creating a new surface area

by cracking. This criteria for cracking is summed up by

$$G = G_c \quad (1.1)$$

$$\frac{G}{A} > 0 \quad (1.2)$$

known as the Griffith criteria [1]. Here G is the total free energy, G_c is the critical strain energy release rate, the minimum energy required to initiate cracks, and A is surface area. Equation (1.1) defines the critical condition for cracks to initiate, and Eq. (1.2) the condition for crack growth.

As lines of force in an elastic body must be continuous, they will go around any micro-crack existing in the system, thus concentrating stress at crack tips [10]. The body chooses the most efficient strain release mechanism, and the crack proceeds along its tip. The creation of a crack releases strain energy perpendicular to the crack face, but there is an accumulation of strain energy parallel to the crack face. Any crack in the vicinity of a pre-existing crack will turn towards the latter and meet it perpendicularly, following the highest strain gradient.

Predicting crack path remains a research area with no clear theory. A stable path can follow any one of the potentially available paths on changes in loading conditions. The possible paths of crack propagation can become unstable if $G = G_c$ is satisfied. Since the remaining paths are still stable, they satisfy $G - G_c \leq 0$. Thus, the unstable path is also the path that maximizes the energy release rate.

The information on any changes in the loading of the material can be transmitted to a growing crack tip, at most, at the speed of sound. A moving crack can only feed off the area where this information reaches. In cases of dynamical fracture, e.g., directional drying or cooling, the strain energy that is available for cracking gets modified with crack speed changes. Where the crack advances at speeds much lower than the speed of sound, the crack advance may be assumed to occur in a quasi-static manner. The stress gradient selects a crack tip position where Eq. (1.1) is satisfied, but where $\frac{G}{A} > 0$, for Eq. (1.2) would take the advancing crack tip to a region of lower strain energy density. If there are several equally preferable paths, some symmetry-breaking mechanism by way of thermal noise or small-scale inhomogeneity determines the choice of one of the paths over the others, and the crack advances along the chosen path.

The principle of local symmetry [4, 8] suggests that crack advancement occurs along that path where the shear stress intensity factor is zero. This theory finds support in the wavy cracks in films that are guided by the orientation of the silicon crystal substrate [6], cracks guided by the memory of perturbative field direction [13–15].

1.2 Patterns of Crack Networks

Fracture patterns refer to the spatial arrangement and geometry of fractures within a material. These patterns are influenced by several factors, including the material's inherent properties (e.g., brittleness, ductility), the type and magnitude of the stress applied, and environmental conditions such as temperature and pressure. In geological formations, fractures often form in response to tectonic forces, thermal contraction, or changes in pore pressure [16, 17]. The resulting fracture networks can vary widely, from simple, isolated cracks to complex, interconnected systems.

Fracture patterns can be broadly categorized into two types: tensile (or mode I) fractures and shear (or mode II and mode III) fractures. Tensile fractures are typically perpendicular to the direction of the applied stress, while shear fractures develop at an angle to the stress direction, allowing for relative movement of the fracture surfaces [18]. The distribution and connectivity of fractures within a material significantly impact its mechanical properties and fluid transport behavior [19].

1.3 Fluid Flow in Fractured Media

Fluid flow through fractured media is a complex process governed by the geometry, connectivity, and aperture of the fractures. In geological formations, fractures often serve as primary pathways for fluid movement, especially in low-permeability rocks where the matrix itself offers little resistance to fluid flow [20]. This is particularly relevant in hydrogeology, petroleum engineering, and geothermal energy extraction, where the efficiency of resource extraction depends on the ability to predict and manage fluid flow through fractured reservoirs.

The study of fluid flow in fractured media involves understanding both single-phase and multiphase flow behaviors. In single-phase flow, a single fluid (e.g., water) moves through the fracture network, and the flow rate is primarily controlled by the fracture aperture and the pressure gradient. In multiphase flow, multiple fluids (e.g., oil, water, and gas) interact within the fracture network, leading to more complex flow patterns due to capillary forces, wettability, and relative permeability effects [21].

Mathematical models, such as Darcy's law and Navier Stokes equation, are often used to describe fluid flow through porous media, but in fractured systems, these models need to be adapted to account for the discrete nature of the fractures. Various approaches, such as the discrete fracture network (DFN) model and the dual-porosity model, have been developed to simulate fluid flow in fractured media more accurately [20].

1.4 Applications and Importance

Understanding fracture patterns and fluid flow in fractured media is essential for a wide range of applications. In the oil and gas industry, fractures play a critical role in determining the productivity of reservoirs. For example, hydraulic fracturing, a technique used to enhance oil and gas recovery, involves creating artificial fractures in rock formations to increase permeability and improve fluid flow. Similarly, in geothermal energy, fractures can enhance heat transfer by providing efficient pathways for the circulation of fluids [21].

In civil engineering, knowledge of fracture mechanics is vital for assessing the integrity of structures and preventing catastrophic failures. Fractures can compromise the strength and stability of materials, leading to potential hazards in buildings, bridges, and other infrastructure. Additionally, in environmental engineering, fractures in rocks and soils can influence the transport of contaminants, making it important to understand fracture patterns and fluid flow for effective groundwater management and pollution control.

In conclusion, the study of fractures, fracture patterns, and fluid flow is a multidisciplinary field that has significant implications for both natural and engineered systems. Advances in this area continue to improve our ability to predict and manage the behavior of fractured materials, contributing to safer infrastructure, more efficient resource extraction, and better environmental protection.

1.5 Organization of the Thesis

The work is structured into two distinct parts: (i) investigating pattern formation due to fracture and their topological and geometric behavior, and (ii) simulating and analyzing stress-induced fracture and fluid flow in porous systems.

In Chapter Two, various static experimental and simulated crack patterns are analyzed and characterized based on their topological properties, expressed as a 4-tuple (n, v, D, λ) , where n represents the average degree of nodes, v the vertices, D the angular defect, and λ the iso-perimetric ratio of all the polygons in the crack mosaic. The analysis reveals that the (n, v, D) and (n, v, λ) spaces are not uniformly dense with data points. Notably, crack patterns generated by the Gilbert and Iterative Cell Division methods cluster together in these spaces, while those generated by Voronoi tessellation form a separate cluster. This observation raises a natural question: can a simulated crack pattern transition between the Gilbert and Voronoi tessellations? To explore this, we examine dynamic systems such as the evolution of columnar joints, mud crack patterns under repeated wetting and drying cycles, and salt playa formations, which are discussed in the following three chapters.

Chapter Three delves into the formation of columnar joints and the evolution of crack fronts in their cross-sectional planes. The top surface of columnar joints initially displays random crack networks, which gradually evolve as the lava cools. This cooling process drives the cracks inward, guided by temperature gradients. The evolution of these crack fronts is traced in the n, v, D and n, v, λ spaces, revealing that the changes are directed toward finding a minimum energy configuration.

Chapter Four focuses on the evolution of mud cracks due to repeated wetting and drying cycles. The evolution of these cracks is modeled using spring networks, and the ‘Voronoi-ness’ of the patterns is measured for each cycle. Additionally, the Voronoi characteristics of real mud cracks and honeycombs are examined, revealing that honeycombs exhibit nearly perfect centroidal Voronoi patterns.

Chapter Five explores the intriguing patterns formed by salt ridges on salt playas. This chapter explains how fracture mechanics, hydrodynamics, and crystal formation and reorganization combine to produce these patterns. The dependence of crystallization time and crystal growth on various environmental conditions is also discussed.

Chapter Six presents simulations of granular porous systems, including the generation of porous structures and the development of fractures due to compressive mechanical stress. The discrete element method (DEM) is employed to model the porous structure and fractures resulting from externally applied compressive forces. This chapter also examines the statistics of micro-cracks and their percolation behavior.

Chapter Seven investigates the flow properties in the generated granular systems, providing insights into how permeability depends on the morphological properties, such as porosity, Euler number, and curvature, of these complex porous structures.

Finally, Chapter Eight presents a summary of the study’s key findings and outlines potential directions for future research.

Chapter 2

Topology and Geometry of Fracture Networks

2.1 Introduction

Cracks come in different shapes and sizes, pervading our world in various forms, such as linear cracks in one dimension, polygonal surface cracks in two dimensions, and even giant columnar joints in three dimensions. They can range from micro-scale microcracks in polycrystals to several kilometers in magnitude on the Earth's mantle. Cracks also exhibit a 'memory' of past history as they emerge along lines correlated with previous stress fields the system had experienced. Some cracks evolve over time, changing their topology and geometry and demonstrating great sensitivity to ambient conditions [22]. The study of cracks has been an active research area for decades due to their wide-ranging applications in engineering, industry, art, and craft, and as a scientific challenge [23–25]. Despite their variety, there is an apparent similarity among many crack patterns that sets them apart from others - for example, mud cracks share a similarity different from glass or concrete cracks.

From analytical arguments, we construct a topology-geometry-allowed domain of cracks. Crack mosaics are examined for their topological and geometrical combinatorics and represented as a point in this domain. It is expected that once a sufficiently large number of data points are collected in this geometry-topology domain of crack patterns, the domain will aid in identifying similarities and classifying crack patterns accordingly.

This work deals with understanding crack networks based on their topology and geometry, exploring various natural crack systems around us, referred to as 'experimental cracks', and simulated crack patterns generated using existing tiling algorithms and their variations. The crack networks are classified based on polygonal edges, vertices, and angles to determine

a representative point of the crack mesh. The crack peds are also examined based on the roundedness parameter λ that measures the constituent polygonal shape in comparison to a circle. The statistics on simulated crack networks are compared to the statistics obtained from experimental cracks in the topology geometry space. Such comparisons act as pointers to the understanding of crack systems in nature, drawing from the logic of simulated cracks. Together, both the experimental and simulated crack networks represented in the topology-geometry space, help to throw light on why crack patterns appear the way they do.

The following sections briefly introduce the basics of combinatorial topology and geometry of convex planar tiling, followed by a discussion on simulated crack mosaics - the different algorithms, results, and statistical quantification. Finally, a comparison of simulated and experimental crack mosaics is done to enable the classification of crack mosaics and gain an understanding of the underlying principles guiding cracking.

2.2 Convex Planar Mosaics

A two-dimensional (planar) mosaic is a set of compact polygonal regions that cover the plane and intersect pairwise only at their boundaries. To avoid trivialities, these regions have non-empty interiors. We consider convex normal planar mosaics. This means that each of the mentioned regions is convex, and there are fixed uniform upper and lower bounds on the diameters of the regions. Each such region is a convex polytope and, therefore, can be expressed as a convex hull of its vertices, which makes computations much more tractable than when convexity is broken.

Mosaics (also called tessellations) of the Euclidean plane by convex regular polygons have been extensively studied. These can be described either in terms of the combinatorics of the edge and vertex sets (Schläfli symbols) or in terms of the action of its symmetry group on the domain. However, as our goal is to understand cracks occurring in nature, we will need to include irregular (but convex) polygons.

2.2.1 Combinatorial Topology of Convex Planar Mosaics

In standard terminology used for polygonal regions, a vertex refers to each zero-dimensional face, while a one-dimensional face is known as an edge. The places where these edges converge are called nodes or junction points within the design. When a node has n edges connecting to it, it is said to have a degree of n . Nodes that are connected to 0 edges are excluded from this consideration. Furthermore, a polygon possessing v vertices is described as having a degree of v .

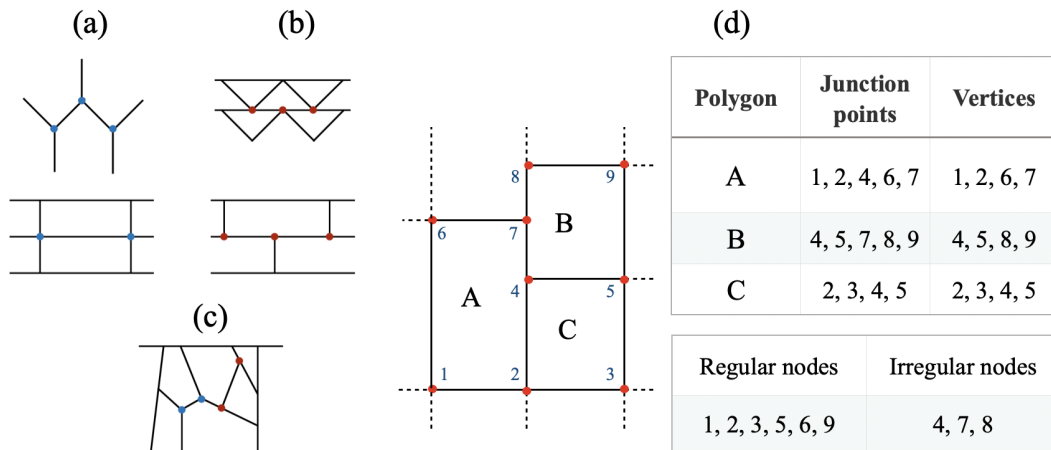


Fig. 2.1 (a) Examples of regular nodes. (b) Examples of irregular nodes. (c) Presence of both regular and irregular nodes. (d) A, B, and C are typical polygons in a schematic mosaic; the nodes are marked by numbers 1 to 9, listing the nodes and vertices for every polygon, along with categorizing the mosaic's nodes as either regular or irregular.

Figure 2.1(d) depicts a schematic of a polygonal mosaic with highlighted polygons A, B, and C. The junction points are numbered 1 to 9. It is important to note that all junction points of a polygon may not form its vertices, as shown in Fig. 2.1(b). For a planar convex mosaic, we calculate the average values, denoted as n and v , of the degrees n and v across the entire mosaic. In the case of an infinite mosaic covering an infinite area of the plane, we consider the limits of these average degrees over planar disks with a radius approaching infinity. Additionally, a node is considered regular if it serves as the vertex of each cell it lies on, as illustrated in Fig. 2.1(a) and (c). If a node does not meet this criterion, it is termed an irregular node of the mosaic. The regularity index p of the mosaic is determined by the ratio of regular nodes to the total number of nodes in the mosaic.

Figure 2.1(d) showcases a diagram featuring a polygonal mosaic with polygons A, B, and C emphasized. The nodes in the mosaic are labeled from 1 to 9. It is important to understand that not all nodes of a polygon necessarily correspond to its vertex, as illustrated in Fig. 2.1(b). When analyzing a convex planar mosaic, we assess the average degree values, labeled as n and v , for the degrees n and v throughout the mosaic. In the case of an infinite mosaic covering an infinite area of the plane, we consider the limits of these average degrees over planar disks with a radius approaching infinity. Furthermore, a node is deemed regular only if it acts as a vertex for every polygon it is part of, as shown in Fig. 2.1(a) and (c). Any node failing to meet this criterion is classified as an irregular node in the mosaic. The proportion of regular nodes to the overall node count in the mosaic gives us the regularity index, denoted as p .

Every convex normal mosaic resides within a bounded combinatorial area on the (n, v) plane. As all polygonal cells of a mosaic have at least three sides, it is clear that $v \geq 3$. To see the effect of the fraction of regularity, p , we compute the average internal angle of vertices of polygons at a node and compare this for both regular and irregular nodes. This relationship is computed as

$$\frac{p+1}{n} + \frac{2}{v} = 1 \tag{2.1}$$

This introduces a natural combinatorial categorization of mosaics based on their p -regularity, known as iso- p lines. Two distinct natural combinatorial curved boundaries within the (n, v) domain are created for the cases when $p = 0$ and $p = 1$. The final boundary of $v \leq 2n$ is obtained by noting the effect of the fraction of regularity on the degree of a node and the maximum possible value of $\frac{v}{2n}$ coming from the above iso- p lines. Figure 2.2(a) shows the allowed domains of infinite convex planar mosaics.

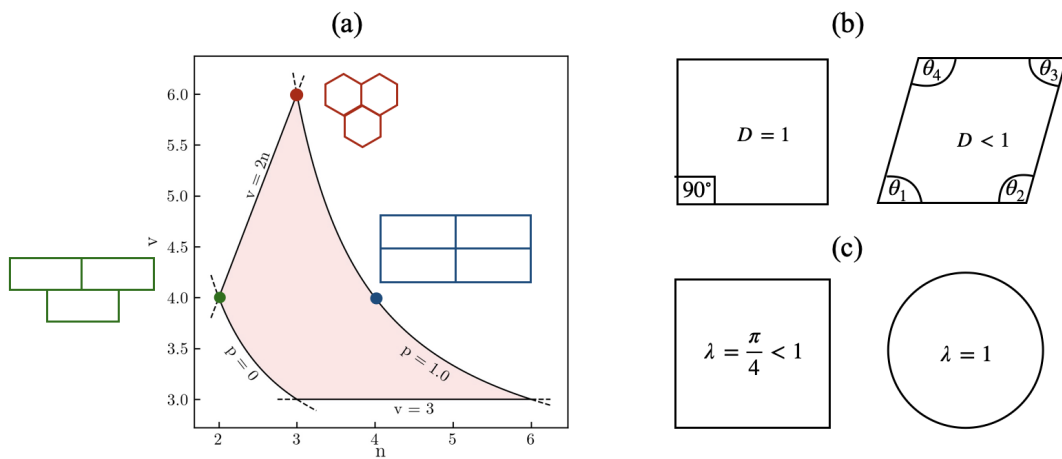


Fig. 2.2 (a) The allowed (n, v) domain of infinite convex planar mosaics, (b) Angular defect D is 1 for regular polygons and D decreases from 1 towards 0 as the polygons deviate from the regular one. (c) For a circle, $\lambda = 1$; and λ decreases from 1 towards 0 as the polygonal structures transform from shapes that are comparatively circular to needle-like forms.

The above analysis assumes that the mosaic is infinite and that the average values n and v come as limits over increasing disks. However, all mosaics encountered in the real world are constructed from images of finite systems. Therefore, representative points of mosaics of physical systems in the (n, v) domain have an inherent error from finite boundary effects. This error can be minimized if the fraction of boundary nodes is small.

2.2.2 Angular Defect D and the (n, v, D) Space

To further distinguish natural cracks, we introduce a measure of the geometric regularity of a mosaic in the form of its non-dimensionalized ‘angular defect’. For the N^{th} polygon, the ‘angular defect’ D_N is defined as

$$D_N = \frac{1}{\sum_{i=1}^{v_N} \left| \theta_i - \frac{(v_N-2)\pi}{v_N} \right| + 1} \quad (2.2)$$

The variable v_N signifies the total vertices of the polygon labeled as the N -th. To quantify the geometric regularity across the entire mosaic structure, we employ the formula

$$D = \frac{\sum_{i=1}^M D_i}{M} \quad (2.3)$$

where M denotes the overall number of polygons (also referred to as cells) within the mosaic. According to this formulation, both measures D_N and D naturally fall within the range of 0 to 1.

Integrating the combinatorial and geometric descriptions, we establish a unified (n, v, D) framework for the complete classification of planar mosaics. This framework outlines a concise three-dimensional space that encompasses all possible configurations of convex planar mosaics.

2.2.3 Isoperimetric Ratio λ and the (n, v, λ) Space

The classical isoperimetric inequality [26] asserts that for any simple, closed curve lying on a plane, if the curve’s length is denoted by L and it encloses an area A , then the inequality $L^2 \geq 4\pi A$ must always hold true. Stemming from this, the concept of the ‘normalized isoperimetric ratio’ is introduced, symbolized by $\lambda = \frac{4\pi A}{L^2}$. This ratio is crucial for identifying various types of natural crack patterns.

This normalized isoperimetric ratio, a dimensionless measure, plays a significant role in classifying and describing the shapes that make up the networks of cracks. For example, a circle has a λ value of 1, while a regular polygon with n sides has a λ value described by $\lambda = \frac{\pi}{n \tan(\frac{\pi}{n})}$, an expression that grows with n and approaches 1. Therefore, as the shapes within the crack network transition from more round to elongated, the λ value decreases from 1 towards 0.

In exploring the angular defect for the N^{th} polygon, one computes its specific λ_N , and thereafter, the overall λ for the network is calculated as the average of these individual values, following the formula:

$$\lambda = \frac{\sum_{i=1}^M \lambda_i}{M} \quad (2.4)$$

where M is the total number of polygons (cells) in the mosaic. The space defined by three dimensions (n, v, λ) facilitates a detailed quantitative narrative of the crack mosaics that could occur, augmenting the previously described space of (n, v, D) .

2.2.4 The Parameter Space of Quadruples (n, v, D, λ)

Moving forward, every crack mosaic, whether real or simulated, will be represented by quadruples (n, v, D, λ) within a specific subset of \mathbb{R}^4 . As explored in Sec. 2.2.1, the relationship between n and v is governed by Eq. (2.1). Thus, with n and p given, v can be determined, although there may be errors due to non-convexity and boundary effects.

Since this work primarily focuses on the low-dimensional categorization and graphical depiction of crack networks, examining them through their topological and geometric characteristics, the crack mosaics are projected onto two distinct 3-dimensional frameworks – one defined by the coordinates (n, v, D) and the other by (n, v, λ) .

2.3 Geometric Simulations of Cracks

Different tiling algorithms and their variations can be used to simulate crack networks. Each crack mosaic is analyzed to determine the average number of nodes (n), the average number of vertices (v), and the average angular defect (D) of the constituent polygons. These values are then plotted as a representative point in the (n, v, D) space and further analyzed and compared using characteristic topological and geometrical descriptors such as angular defect D_N , crack length, tile area, and the polygonal roundedness measure λ . Statistical data from simulated crack networks can be compared to data from real cracks regarding their position in the topology geometry space. These comparative studies can provide insights into understanding crack systems in nature. The findings from the generated and analyzed simulated crack networks are presented in this work.

2.3.1 Gilbert Tessellation and Its Variations

The Gilbert tessellation begins by selecting a group of points as initial seeds. Subsequently, lines are drawn from these points, extending in both directions until they encounter either another line or a boundary. Various alternatives are explored, as mentioned below. These lines are interpreted as cracks, leading to the formation of angular, extended, polygonal shapes that resemble the patterns observed in broken glass. The flowchart outlining the generation of a Gilbert mosaic is described below.

Algorithm 1

-
- 1: Cracks are initiated at random points (seeds) throughout the plane.
 - 2: The cracks are allowed to grow simultaneously from all the seeds.
 - 3: From every seed, the cracks grow in two opposite directions along a straight line with a slope that is chosen randomly from a uniform distribution.
 - 4: A crack stops growing when it collides with another crack.
 - 5: If two growing crack tips collide, only one chosen randomly will continue to grow.
-

The basic algorithm has been implemented in various forms. These variations involve modifications to the distribution function of the random seeds on the plane and the selection of crack slope in relation to reference axes. Four different crack slope choices were examined for each seed distribution:

- (a) Selection between 0° and 180° at random.
- (b) Slopes parallel to reference axes, i.e., 0° or 90° .
- (c) Random selection of slopes from 0° , 45° , and 90° .
- (d) Random determination of slope between $0^\circ \pm 10^\circ$ and $90^\circ \pm 10^\circ$.

Uniform Distribution of Crack Seeds

Figure 2.3 presents the results for a uniform distribution of crack seeds on a 2-dimensional 30×30 plane, structured into a 4×5 matrix. The rows of the matrix give information on each of the 4 combinations of slopes taken for the Gilbert tessellated crack mosaics having uniform seed distribution. For each variation of the crack pattern, the five columns display (1) the visual pattern of the crack formation, (2) a histogram detailing the distribution of angular defects D_N , (3) a histogram showing the distribution of the number of vertices for the polygons within the mosaic, (4) a histogram representing the variation in crack lengths, and (5) a histogram outlining the area distribution of the tiles or polygons produced.

In our analysis of the second column in the matrix figure, intriguing observations emerge regarding the nature of crack mosaics:

- a) Cracks possessing random slopes exhibit a log-normal distribution for D_N , with an average value of about 0.325. This suggests a dominant presence of irregular polygons.
- b) Cracks oriented at 0° or 90° take on perfect rectangular shapes, illustrating the captivating symmetrical arrangements they form.
- c) Incorporating one-third of the slopes at 45° introduces a significant quantity of irregular

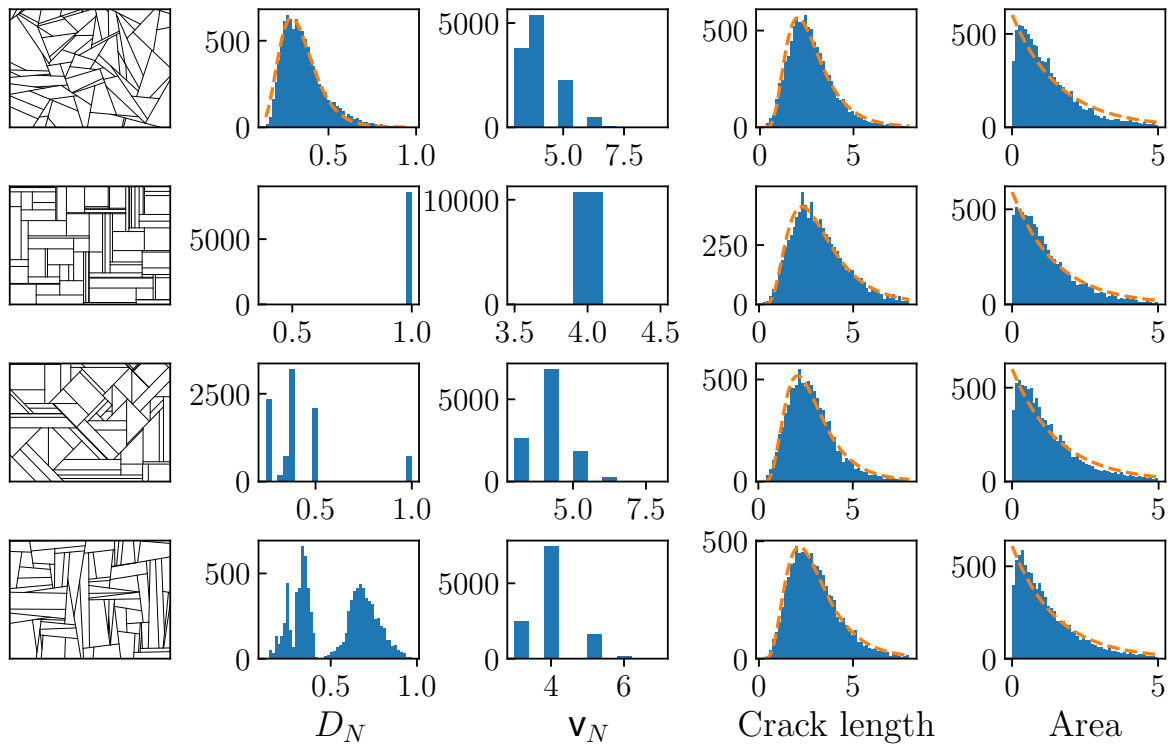


Fig. 2.3 The 4×5 matrix illustrates the Gilbert tessellation with a uniform seed distribution. The first four rows represent different selections of crack slopes: (1) random angles between 0° and 180° , (2) slopes aligned with the reference axes at 0° or 90° , (3) randomly chosen slopes from 0° , 45° , and 90° , and (4) randomly selected slopes within $0^\circ \pm 10^\circ$ or $90^\circ \pm 10^\circ$. The five columns display: (1) the crack mosaic, (2) the angular defect D_N histogram, (3) the histogram of the number of vertices in the polygons, (4) the crack length histogram, and (5) the polygon area histogram.

polygons. This change diversifies the mosaic with elements of randomness and variety.

d) Slopes within $0^\circ \pm 10^\circ$ and $90^\circ \pm 10^\circ$ lead to an interesting division in the histogram, showing pronounced peaks near 0.36 and 0.7.

The histogram for the vertices showcased in column 3 of the matrix in Fig. 2.3 reveals that quadrilaterals dominate the distribution of polygons, with notable quantities of triangles, pentagons, and a small presence of hexagons, regardless of choice (b) concerning the slopes. Furthermore, the histogram detailing the lengths of cracks in column 3 of Fig. 2.3 shows a log-normal distribution across all slope combinations investigated, featuring a nearly consistent shape parameter of $\sigma \approx 0.49$ and a median value fluctuation around 7% near 2.82. It is also important to mention that the surface area of polygons within the four crack mosaics adheres to an exponential decay model described by ae^{-bx} , where $a \approx 394.8$ and $b \approx 408$. Examination of

the elements in Fig. 2.3 indicates that the variation in the slope of cracks for Gilbert tessellation is most noticeable in the shape of the polygons rather than their sizes.

Normal Distribution of Seeds

The image shown in Fig. 2.4 illustrates the outcomes for normally distributed crack seeds across a two-dimensional 30×30 plane, organized into a 4×5 matrix. Every feature of the mosaics analyzed under this normal distribution is encapsulated within the elements of the matrix, adhering to the format previously seen in Fig. 2.3. Column 1 of the matrix in Fig.

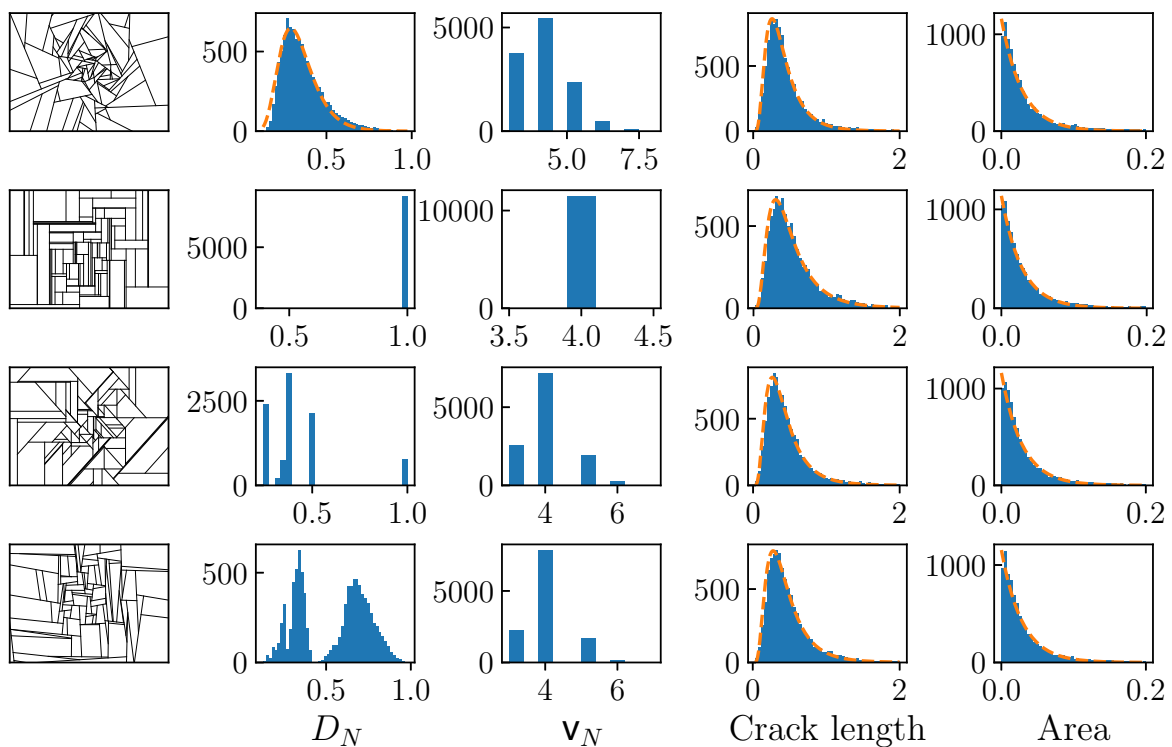


Fig. 2.4 The 4×5 matrix illustrates the Gilbert tessellation with a normal seed distribution. Rows 1 to 4 correspond to four different selections of crack slopes: (1) random angles between 0° and 180° , (2) slopes aligned with the reference axes at 0° or 90° , (3) randomly chosen slopes from 0° , 45° , and 90° , and (4) randomly selected slopes within $0^\circ \pm 10^\circ$ and $90^\circ \pm 10^\circ$. Columns 1 to 5 display: (1) the crack mosaic, (2) the angular defect D_N histogram, (3) the polygon vertex count histogram, (4) the crack length histogram, and (5) the polygon area histogram.

2.4 clearly reveals a clustering of smaller polygons around the system's central region, as anticipated. Analysis of the other matrix elements shows that altering the seed distribution of the cracks on the plane does not result in significant changes in the histogram patterns of the angular defect, polygon vertices, crack length, or polygon area. Both the crack length and

polygon area distributions exhibit log-normal and exponentially decaying behaviors, similar to the uniform seed distribution. However, the shape parameter and median values for the log-normal distribution of crack lengths suggest narrower distributions, which is also reflected by smaller values in the parameters governing the exponential decay of polygon areas.

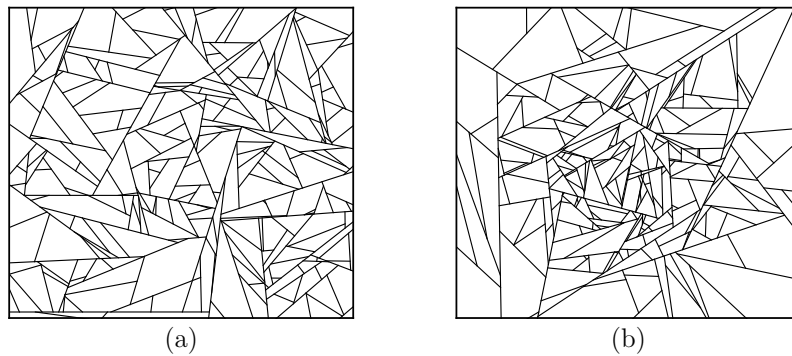


Fig. 2.5 The Gilbert tessellation with time-delayed crack initiation features: (a) a uniform distribution of initial cracks, and (b) a normal distribution of initial cracks.

A different version of the Gilbert tessellation was conducted, in which the initiation of cracks was sequentially offset by a predetermined delay among various seeds. The mosaic design resulting from both uniform and normal distributions of crack seeds is illustrated in Fig. 2.5. When comparing these images with the components of the figure matrices in Figs. 2.3 and 2.4, there appears to be no noticeable variation in the patterns. An animation of the Gilbert tessellation process is available in Ref. [27].

2.3.2 Voronoi Tessellation

Voronoi tessellation was simulated using the Python class ‘Voronoi’. The Python class ‘Voronoi’ in ‘scipy.spatial’ uses the Qhull library to find the Voronoi diagram. Qhull computes the Delaunay triangulation of the given input seeds by computing a convex hull using the Quickhull algorithm [28]. The circumcenters of the Delaunay triangles represent the Voronoi vertices.

The Voronoi mosaic effectively divides the system into polygonal regions closest to the seed that causes the crack polygon, much like the Wigner-Seitz unit cell description in crystallography. Figure 2.6 presents a matrix visualization of Voronoi tessellation, employing crack seeds that are uniformly and normally distributed, as depicted in the first and second rows, respectively. The pattern of crack seeds following a normal distribution leads to increasingly smaller crack fragments clustering towards the center of the system, as shown in the first column. Columns 2 to 4 illustrate histograms related to the angular defect, the area of the polygons, and the number of vertices for each polygon, respectively. The histogram for D_N

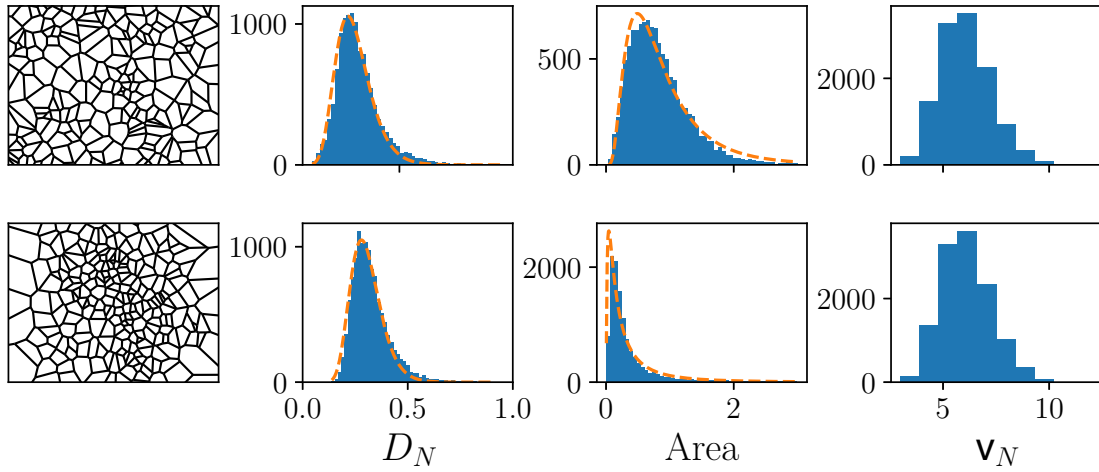


Fig. 2.6 The 2×4 matrix represents a Voronoi tessellation. Rows 1 and 2 correspond to uniform and normal seed distributions on the plane, respectively. Columns 1 to 4 display: (1) the crack mosaic, (2) the histogram of the angular defect D_N , (3) the histogram of polygon/tile areas (in arbitrary units), and (4) the histogram of the number of vertices for the polygons in the mosaic.

illustrates a log-normal distribution observed in both the normal and uniform cases of the Voronoi tessellation, with the median value slightly more inclined towards lower numbers in the normal distribution compared to the uniform one. Further analysis of the third column in the figure matrix Fig. 2.6 indicates that the normal Voronoi tessellation exhibits a log-normal distribution for the areas of the polygons, which is noticeably more condensed and with an extended tail when compared to that of the uniform Voronoi distribution. Examination of column 1 reveals that in the case of normal seed distribution, the larger polygons are roughly confined to the boundary of the system and are much fewer in number in comparison to the ‘smaller’ polygons that occupy the greater part of the plane. The contrast between the sizes of the peripheral polygons and the central polygons is sharp enough to be discernible with the more smaller and uniform peds clustered in the central region. Together, these features are responsible for the sharp decay in the area distribution. In comparison, the polygons obtained with a uniform seed distribution have a broader histogram in area distribution with a more gentle decay. Here, the Voronoi tessellation differs significantly from the Gilbert tessellation, where an exponential decaying distribution was obtained for polygonal area statistics.

In Fig. 2.6, histograms are displayed showing the number of vertices per polygon for two different Voronoi mosaics. The distribution curve of v_N follows a log-normal pattern and is quite similar for both mosaics. In the case of Gilbert tessellation, the nature of the distribution of v_N was also similar, but there are significant differences in the parameters defining the distribution. In Voronoi tessellation, there are a maximum number of hexagons with a significant number of

pentagons and heptagons, unlike in Gilbert tessellation, where the peak of the distribution was at 4 with a significant number of triangles and a smaller number of pentagons.

2.3.3 Iterative Cell Division

The flow chart for the Iterative Cell Division algorithm for crack mosaic simulation is outlined below.

Algorithm 2

- 1: Choose any two sides of a polygon randomly.
 - 2: Randomly select a point on each of the two sides chosen in the previous step.
 - 3: Connect the two points chosen in the previous step with a straight line.
 - 4: Repeat the process from the first step as many times as desired.
-

Figures 2.7 (a), (b), and (c) illustrate the progression of crack mosaic formation after the 1st, 4th, and 8th rounds of iteration, in accordance with the previously mentioned algorithm. New cracks are represented by dashed lines. Additionally, various histograms detailing angular defect, polygon area, vertices per polygon, and crack length, based on the pattern formed at the 10th iteration, are presented in Figs. 2.8 (a), (b), (c), and (d), respectively.

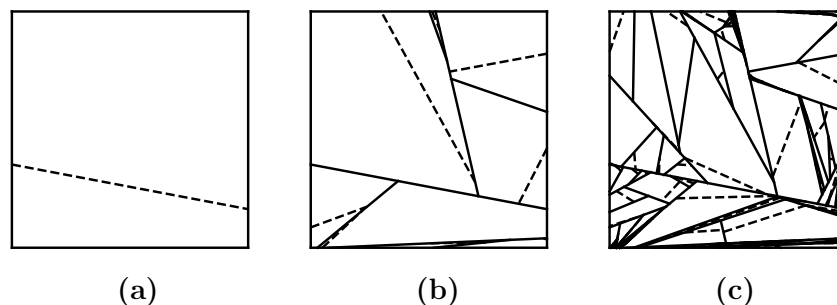


Fig. 2.7 Crack mosaic generated through iterative cell division. Images (a), (b), and (c) correspond to the results after the 1st, 4th, and 8th iterations, respectively. The newest cracks are highlighted with broken lines.

The histogram of angular defects shows a sharp double peak, indicating that the polygons are highly irregular. The histogram of polygon areas peaks at a small value, suggesting that very narrow crack polygons are generated using this algorithm, which is also evident from Fig. 2.8(c). The histogram of the number of vertices per polygon indicates that most polygons are triangles, with a nearly equal number of quadrilaterals. The number of pentagons and hexagons decreases rapidly in the distribution. The histogram of crack lengths shows a sharply decaying curve, although it is not exactly exponential in nature.

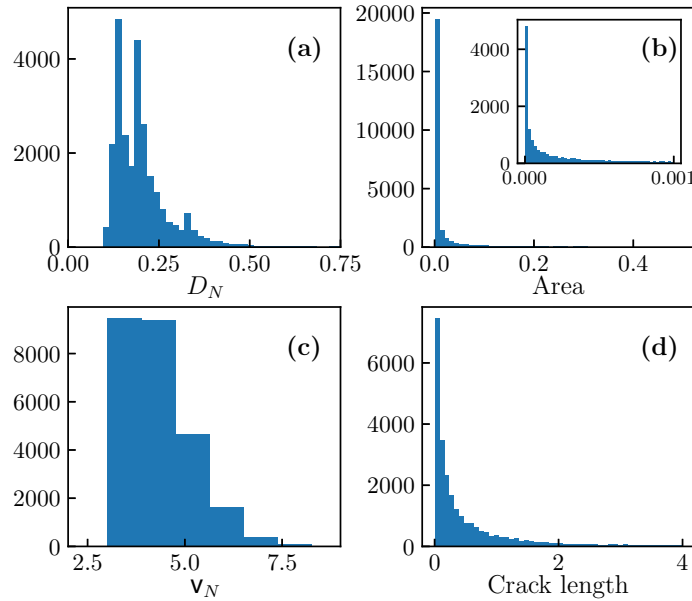


Fig. 2.8 Measures of Crack Mosaic using Iterative Cell Division after 10^{th} iteration (a) Histogram of the angular defect D_N (b) Histogram of polygon/ tile area (c) Histogram of the number of vertices per polygon in the mosaic (d) Histogram of crack length.

2.4 Real Crack Mosaics

Investigation and classification of crack mosaics from various physical systems are conducted based on their topological and geometrical features. This serves two main purposes: to determine if cracks of similar materials, cracking modes, or forcing mechanisms form distinct clusters in a specific space and to compare actual crack formations with the simulated crack mosaics. Meticulous checks and balances are essential for determining (n, v, D, λ) data from physical system mosaics. To do this, a crack skeleton is extracted from images using algorithms and suitable processing techniques. The algorithm involves identifying nodes, polygons, and crack vertices and dealing with convex and non-convex polygons as needed. The process involves image thresholding, crack skeleton extraction, node identification, and polygon tagging. The identification of vertices in crack mosaics is a non-trivial issue, and it requires determining the convexity of polygons using the gift-wrapping algorithm [29].

2.5 Mapping the Topology of Simulated and Real Cracks on the (n, v) Plane

The average values of n and v for the entire mosaic are calculated by assessing the nodes and vertices of each polygon. Figure 2.9 illustrates the coordinates of all the simulated and experimental crack mosaics examined. Iso- p lines at values of 0.5 and 0.3 are drawn to help visualize the fraction of regular nodes in these crack patterns. Since natural crack mosaics tend to be irregular, the data points predominantly cluster between $p = 0.3$ and $p = 0.5$. Despite the inclusion of various materials in the study, such as natural mud, clays like bentonite, synthetic clays like laponite, corn starch, resin, glass, and metal oxide films, the data points remain concentrated within a small region of the parameter space. This suggests that n and v alone may not be sufficient to reveal clusters of similar materials through crack pattern analysis, given the wide variation in physical and chemical properties. Therefore, more refined measures might be needed to distinguish between distinct crack clusters.

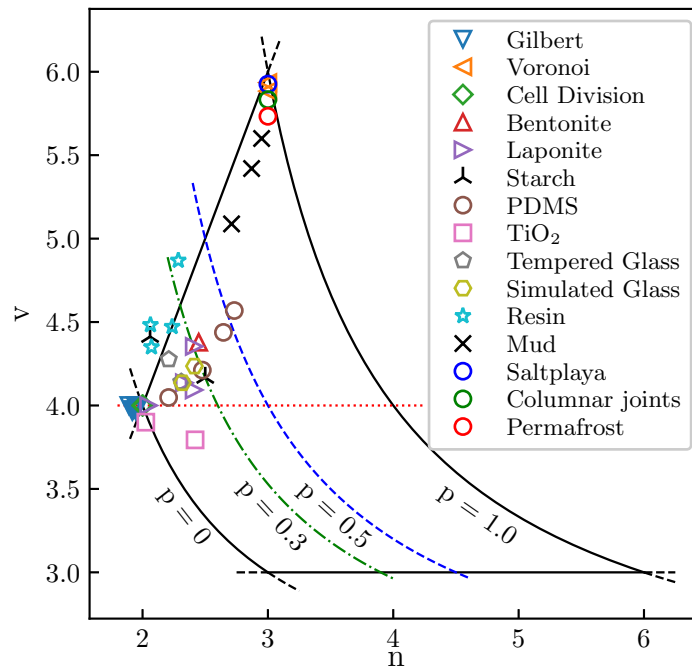


Fig. 2.9 The (n, v) data for real and simulated crack mosaics, with iso- p lines at $p = 0.3$ and $p = 0.5$ included as visual guides.

2.6 Features of the Crack Mosaics on the (n, v, D, λ) Space

The various simulations of crack mosaics exhibit distinct differences in their geometric characteristics. To compare these features with those of experimentally observed cracks, the average geometric properties are plotted in the (n, v, D) space, as shown in Fig. 2.10(a).

All data points fall within the analytically defined allowed space. Most of the simulated crack mosaics cluster around $n = 2$ and $v = 3.5$, with the exception of the Voronoi mosaic, where $n = 3$ and $v = 5.9$. Both the Voronoi and Iterative Cell divisions have D values close to 0.2, indicating a high degree of irregularity in the polygons. Variants of the Gilbert tessellation exhibit D values clustering around 0.5.

A histogram of λ for the Gilbert and Voronoi tessellations is shown in Fig. 2.11, with a noticeably different distribution across the simulation variants. This provides insights into the shape distribution of polygons within the mosaic. In the case of Gilbert tessellation, the polygon shapes largely depend on the angle between a growing crack and a reference line, as illustrated in Figs. 2.11(a-d), showing a wide dispersion of shapes.

For the Iterative Cell division algorithm, the isoperimetric ratio λ , assessed at various stages, reveals that the polygons become more elongated at higher stages, with λ decreasing linearly with the order number [see Fig. 2.13(a)]. A histogram of λ for the 10th order, shown in Fig. 2.13(b), demonstrates that most polygons exhibit highly elongated shapes.

Given that most simulation points cluster around the $n \sim 3$ and $v \sim 4$ region – except for the Voronoi tessellation at $n \sim 3$ and $v \sim 6$ – a two-dimensional variation of the four-parameter phase space is constructed using (n, v, D) and (n, v, λ) data [see Figs. 2.10(b) and (d)]. These figures zoom in on the data points, spacing them along the vertical axis, which prominently highlights the variation in D and λ values.

Table 2.1 lists the topological combinatorics and geometrical information of the simulated and real crack systems.

2.7 Comparison Between Physical and Simulated Mosaics

Exploring the similarities between simulated and real-world crack patterns opens up an insightful analysis. The visual representation in Fig. 2.10 juxtaposes (n, v, D) and (n, v, λ) data for both experimental and simulated crack mosaics, offering a unified perspective. A notable observation is that, with the exception of Voronoi simulations, the (n, v) values for simulated cracks hover around $(2, 4)$, aligning closely with the experimental data for all types of crack mosaics barring mud. On the other hand, mud crack mosaics share their (n, v) values of approximately $(3, 6)$ with Voronoi simulations. Delving deeper, Figs. 2.10(b) and (d) focus on

Table 2.1 Measures of simulated and real crack mosaics

		Model	n	ν	D	λ
Gilbert	Uniform seed distribution	Randomly oriented cracks	1.962	3.984	0.363	0.482
		Parallel cracks	1.941	4.0	1.0	0.403
		Cracks at 0°, 45° and 90°	1.958	3.99	0.420	0.476
		Cracks orientations in between (-10°– +10°) and (80°–100°)	1.954	3.987	0.542	0.422
	Normal seed distribution	Randomly oriented cracks	1.946	3.968	0.361	0.477
		Parallel cracks	1.891	4.0	1.0	0.405
		Cracks at 0°, 45° and 90°	1.929	3.976	0.419	0.476
		Cracks orientations in between (-10°– +10°) and (80°–100°)	1.918	3.965	0.524	0.402
Voronoi	Uniform seed distribution	3.0	5.884	0.319	0.683	
	Normal seed distribution	3.0	5.935	0.325	0.714	
Iterative Cell Division	Iteration order					
		6	2.0	4.0	0.246	0.235
		7	2.0	4.0	0.230	0.207
		8	2.0	4.0	0.218	0.167
		9	2.0	4.0	0.211	0.146
		10	2.0	4.0	0.202	0.128
		11	2.0	4.0	0.200	0.124
Real cracks		12	2.0	4.0	0.192	0.103
		Bentonite	2.442	4.479	0.463	0.739
		Laponite (pH 10)	2.333	4.136	0.483	0.579
		Laponite (pH 13)	2.048	4.0	0.415	0.618
		Laponite (pH 14.4)	2.410	4.093	0.484	0.625
		Laponite (pH 6.7)	2.411	4.353	0.467	0.647
		Corn starch	2.5	4.16	0.466	0.674
		Potato starch	2.606	4.411	0.425	0.554
		PDMS - 1	2.731	4.569	0.428	0.618
		PDMS - 2	2.644	4.438	0.445	0.587
		PDMS - 3	2.477	4.212	0.453	0.612
		TiO ₂ (primary)	2.025	3.9	0.415	0.513
		TiO ₂ (secondary)	2.419	3.794	0.461	0.497
		Tempered glass - 1	2.208	4.276	0.416	0.547
		Tempered glass - 2	2.309	4.141	0.428	0.548
		Resin - 1	2.284	4.868	0.410	0.789
		Resin - 2	2.063	4.482	0.370	0.657
	Resin - 3	2.236	4.472	0.393	0.675	
	Mud	2.870	5.42	0.387	0.774	
	Columnar joints	3.0	5.833	-	-	
	Salt Playa	3.0	5.926	-	-	
	Permafrost	3.0	5.733	-	-	

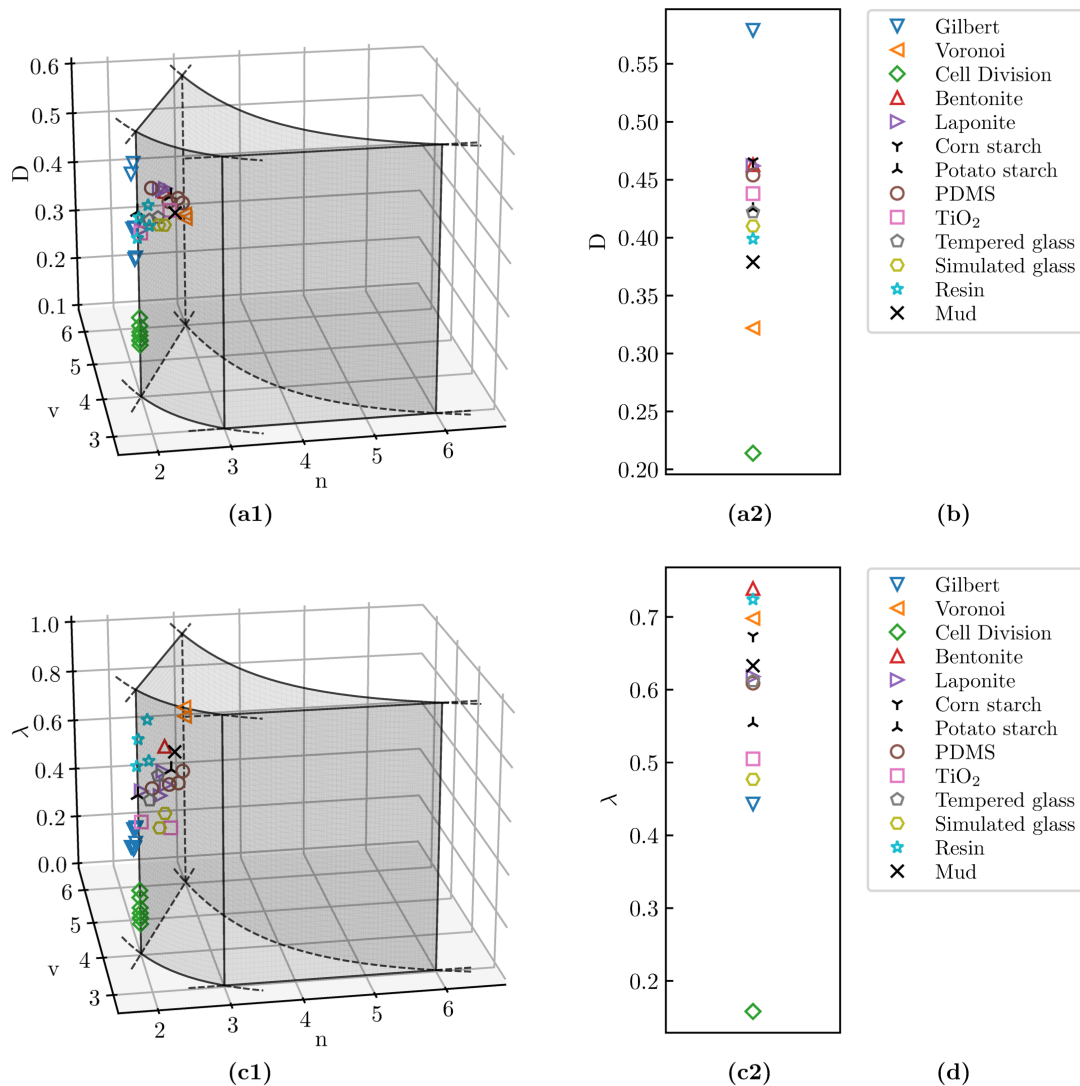


Fig. 2.10 (a1) (n, v, D) data of real and simulated crack mosaics. (a2) Zoomed-in view of (n, v, D) data. (c1) (n, v, λ) data of real and simulated crack mosaics. (c2) Zoomed-in view of (n, v, λ) data. (b) Legends for (a1) and (a2) and (d) legends for (c1) and (c2)

the geometric metrics D and λ for both experimental and simulated cracks. By averaging data for similar materials, each material type is condensed into a singular data point in these figures. This approach yields two significant outcomes: firstly, it resolves the seeming overlap in (n, v) measures by distinctly locating different material types in the 4-parameter space; secondly, it hints at the possibility of matching experimental cracks with certain Gilbert tessellations. Among the geometric measures analyzed, the isoperimetric ratio λ emerges as a particularly effective tool in differentiating crack mosaics.

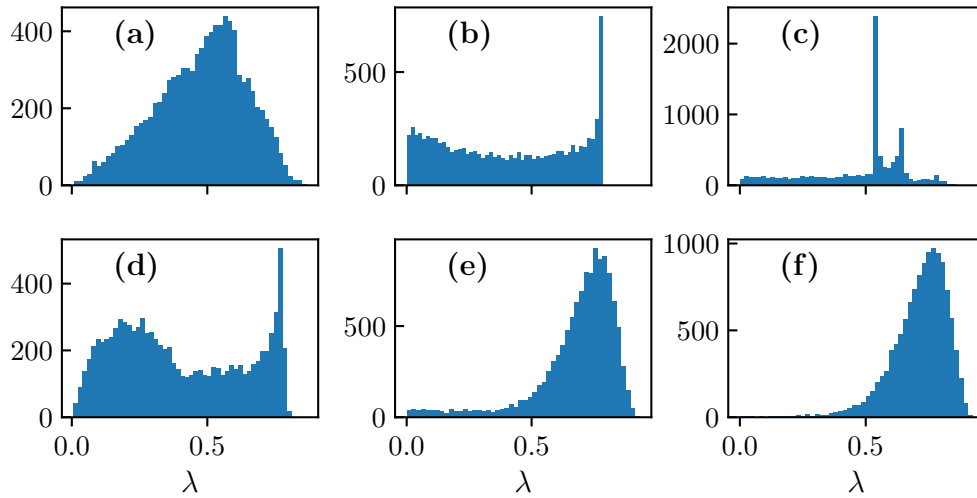


Fig. 2.11 Histogram of isoperimetric ratio λ for simulated crack mosaics: (a) Gilbert tessellations with random slopes, (b) slopes at 0° and 90° , (c) slopes at 0° , 45° , and 90° , (d) slopes at $0^\circ \pm 10^\circ$ and $90^\circ \pm 10^\circ$. For Voronoi tessellations, (e) uniform seed distribution, and (f) normal seed distribution. The average values of the λ parameter are presented in Tab. 2.1.

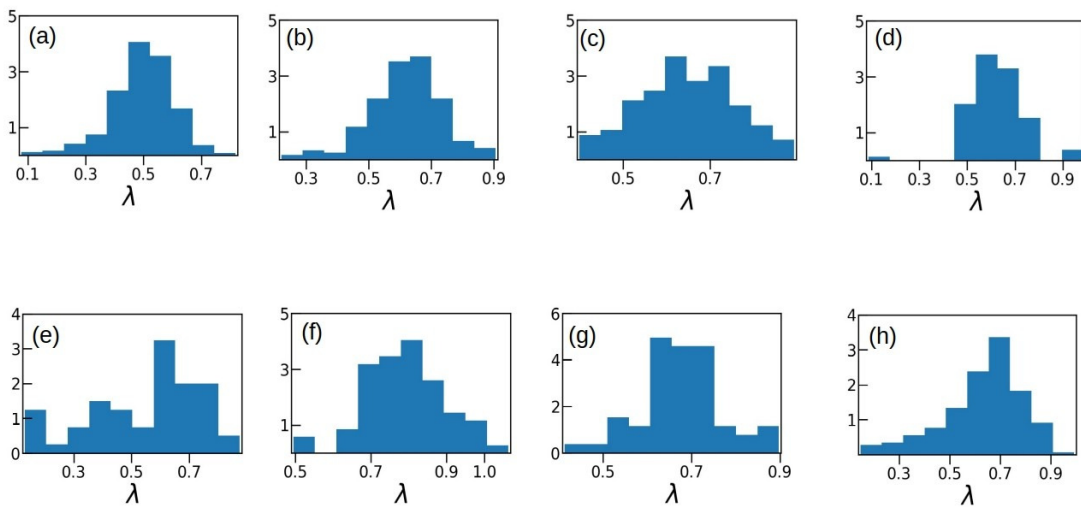


Fig. 2.12 Histogram of isoperimetric ratio λ for real crack mosaics of: (a) TiO_2 , (b) PDMS, (c) Laponite (pH 6.73), (d) Laponite (pH 13.45), (e) Tempered Glass, (f) Resin, (g) Corn starch, and (h) Mud cracks.

The aim of contrasting topological and geometrical analytics between natural crack formations and their simulated equivalents is to shed light on the underlying processes of natural cracking. The isoperimetric ratio λ for a selection of natural crack mosaics is showcased in

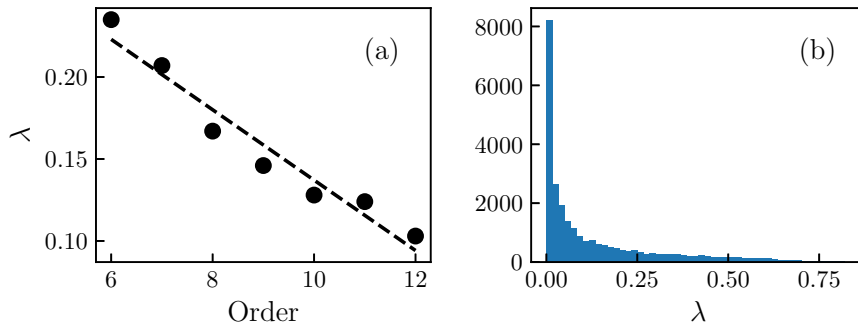


Fig. 2.13 (a) Variation of isoperimetric ratio λ across different iteration stages in the cell division method. (b) Histogram of λ at the 10th iteration step.

Fig. 2.12, which when compared to the simulated crack λ values in Fig. 2.11, indicates that materials such as TiO₂, PDMS, and Laponite at $pH = 6.73$ exhibit a similar λ distribution to that found in Fig. 2.11(a), suggesting a Gilbert tessellation pattern with variable slopes. Conversely, Laponite at $pH = 13.45$ presents a λ distribution more akin to a strict Gilbert pattern with crack angles fixed at 45 and 90 degrees, as depicted in Fig. 2.11(c), while accounting for natural variances. Similarly, the λ distributions for tempered glass [see Fig. 2.12(e)] closely mirror the dual-mode Gilbert tessellation observed in Fig. 2.11(d) with slopes concentrated around 0 ± 10 , and 90 ± 10 degrees. Additionally, the λ distributions for crack mosaics made of resin, corn starch, and mud [see Figs. 2.12(f), (g), and (h)] are comparable to those seen in Voronoi mosaics [see Figs. 2.11(e) and (f)], suggesting a shared developmental algorithm with their simulated counterparts. Interestingly, uniformly desiccating systems, which form cracks analogous to the Gilbert algorithm's logic, further underscore this point.

Experimental research further corroborates that corn starch matures into columnar joints exhibiting transverse Voronoi tessellations; similarly, natural mud cracks undergo a cycle of wetting and drying, leading to Voronoi patterns, indicating that Voronoi tessellation principles are at play in these natural phenomena.

2.8 Discussion

In this study, the formation of crack mosaics across a variety of materials – including natural mud, clay types such as laponite and bentonite, starches derived from corn and potato, polymers like PDMS, films of metal oxide, and both glass and resins – has been investigated. The aim was to categorize these crack patterns by identifying significant shared features, linking them with the materials they appeared on, and pinpointing the physical, chemical, or geological mechanisms behind their creation. The focus was on determining whether materials that share

certain characteristics, like molecular bonding types and physical or rheological attributes, also exhibit similar patterns of cracking. To achieve this, methods from planar convex tiling and combinatorial topology were used to describe and sort the diverse types of crack mosaics. Ideally, a comprehensive dataset covering a wide range of materials and multiple datasets would facilitate the development of a robust four-parameter phase space. This statistical approach could then assist in determining the material of origin based on crack patterns.

The geometrical and topological aspects of the crack mosaics were quantitatively analyzed and organized into a four-parameter phase space. This quartet (n, v, D, λ) acts as a concise signature for any given crack mosaic. Here, the topological variables v and n account for the cells within the mosaic and their connections to adjacent cells, whereas the geometric variables D and λ detail the cells' shapes. These parameters are graphically represented through two three-dimensional spaces: (n, v, D) and (n, v, λ) , effectively differentiating between crack patterns from various materials and models. It is vital to recognize the influence of environmental conditions on crack development, which introduces variability to patterns of similar materials. Previous research by Domokos et al. [30] suggested that fractures and cracks in geological systems largely fall into either 'Platonic' or 'Voronoi' categories, albeit without a solid theoretical explanation. Our research demonstrates that, by focusing on the combinatorial (n, v) topology alone, crack mosaics from beyond geological contexts can also be approximately sorted into these categories. We discovered that crack mosaics pertaining to different classes of materials tend to cluster within the four-parameter phase space. This indicates a correlation between materials' physical and chemical properties and their resulting crack geometries. Similar analyses on simulated crack mosaics show that the (n, v) data for Gilbert cracks consistently approaches $\sim (2, 4)$ across different versions of the algorithm.

2.9 Conclusions

The study analyzes crack statistics and examines crack mosaics that have reached an equilibrium state. It demonstrates that accurate measures of the geometry and topology of crack mosaics can effectively differentiate between crack systems based on crack mechanisms and intrinsic material properties. However, distinguishing between crack mosaics cannot rely solely on their topological combinatorial values (n, v) . For precise identification, it is essential to consider the geometrical features of the polygonal mosaics.

A comprehensive quantitative analysis of the average geometrical and topological characteristics of crack mosaics is encapsulated in a four-parameter set (n, v, D, λ) . This quartet of parameters serves as a compact signature that defines the essence of a crack mosaic. The study identifies two distinct three-dimensional realms, defined by the spaces (n, v, D) and (n, v, λ) ,

which effectively illustrate the differentiation of crack patterns based on underlying materials and theoretical models. Materials with similar physical and chemical properties often exhibit comparable crack geometries. Significant differences in the mean values of D and λ have been observed across various materials.

Custom codes have been developed to accurately calculate the topological and geometrical properties of non-convex polygons interwoven with convex polygons within a mosaic, ensuring the preservation of the original geometrical and topological features. Naturally occurring cracks tend to exhibit characteristics similar to Gilbert models, with a notable tendency to form T-junctions. Simulations suggest that the crack mechanisms, rather than specific material characteristics, determine whether the resulting crack mosaics resemble Gilbert or Voronoi patterns.

The study identifies two main topological regions, referred to as the ‘Platonic attractor’ and the ‘Voronoi attractor.’ When geometric factors of the crack mosaics are considered, data points in these regions become dispersed. Some crack mosaics initially aligned with the ‘Platonic attractor’ transition to the ‘Voronoi attractor’ in the equilibrium state. Investigating the trajectory of this evolutionary process in the context of the topology-geometry architecture presents an intriguing avenue for further study.

The upcoming three chapters will explore specific dynamical systems, such as columnar joints, repeated wetting and drying of mud, and salt playas, to further elucidate these concepts.

Chapter 3

Columnar Joints

3.1 Introduction

In the previous chapter (Chapter 2), we examined various real crack mosaics of different materials alongside several variations of simulated crack mosaics. It was noted that, from a topological perspective, crack mosaics generally fall into two categories: Gilbert or Voronoi cracks. When exploring the mathematically allowed space of (n, v, D, λ) , we observed that real crack meshes predominantly cluster around the Gilbert crack representative point. In contrast, only a few crack mosaic points are situated near the Voronoi crack descriptor, leaving much of the allowed domain space devoid of real crack mosaic instances. While columnar joints *initiate* as Gilbert cracks and *mature* into Voronoi cracks, the detailed trajectory of their evolution through the (n, v, D, λ) space remains to be fully mapped.

Columnar joints represent a unique crack system where the role of the interface is crucial. Crack formation inherently involves the creation of new interfaces, as seen in common examples like desiccation cracks in drying films or slurries, which typically manifest as two-dimensional mosaics [31]. In these cases, the new surfaces form primarily in the third dimension (thickness), which is minimal compared to the lateral dimensions of the pattern. A particularly striking and distinct example of crack formation occurs in the phenomenon of columnar joints [32]. Unlike everyday cracks, columnar joints form column-like structures as molten volcanic lava cools and fractures under specific thermal and elastic conditions. These cracks propagate downward, creating long vertical columns with polygonal cross-sections, resulting in a fascinating geological formation.

Most natural crack networks, regardless of the material type, consist of tightly packed polygons that converge at T-junctions. This pattern is expected because new cracks tend to intersect existing cracks perpendicularly, efficiently dissipating in-plane stress. However, the remarkable columnar joints found in formations like Giant's Causeway in Ireland and Devil's



Fig. 3.1 Columnar joint in Tsumekisaki Izu, Japan. Photo credit: hide. S [39]

Postpile in California feature Y-junction intersections within pentagonal and hexagonal cross-sectional patterns [32]. These three-dimensional structures originate as random crack patterns on the surface of cooling lava, which extend downward and gradually segregate the rock into vertical columns. As the columns deepen, they stabilize into Y-junction formations. Similar patterns have been observed on a smaller scale in drying starch slurry columns [33].

Gauthier et al. [34] investigated the transition from T-junctions to Y-junctions in crack systems, showing through laboratory experiments that varying cooling rates can produce star-shaped cracks at 90° or 120° angles. Over time and across different length scales, hexagonal columnar patterns develop, ranging from tens of centimeters in laboratory conditions to several meters in natural formations such as Giant's Causeway [32] and the Genbudo caves in Japan [see Fig. 3.3(b)]. These patterns may undergo repeated cycles of healing and re-cracking over various time scales, as noted by Goehring [35]. The transformation from T-junction to Y-junction fracture systems [34, 35] implies a reduction in system energy [36]. Budkewitsch et al. [37] examined pattern maturation by initiating with Voronoi polygons and random crack seeds, generating successive Voronoi polygons using the centroids of the previous ones as seeds. Jagla [38] proposed that crack progression in columnar joints is driven by a balance between two factors: the crack front gains energy by advancing ahead of neighboring cracks, reducing stress, but its driving force weakens as it enters regions of lower thermal shrinkage stress.

Hofmann et al. [40] simulated crack patterns caused by thermal shock using a 3-D gradient damage model, leading to regular hexagon formations in the final stages. Interestingly, most junctions in the early stages of the simulation were near $\sim 120^\circ$. Additionally, Hofmann et

al. [41] used three-dimensional finite element methods to model the incremental progression of crack fronts, accounting for local crack extension and deflection angles relative to previous crack planes.

This work investigates the elongated interfaces of columnar joints, particularly how their cross-sections transition from a disordered Gilbert tessellation to an ordered hexagonal Voronoi pattern. As these columns extend to several meters in length, various intriguing changes occur at the growing interface. The outline continuously evolves, the center may shift, and the columns may twist. This study systematically explores these phenomena through simulations across a wide range of systems and compares the results with natural examples.

The objectives of this work are threefold: (1) to simulate the three-dimensional formation of columnar joints in cooling lava, (2) to map their evolution within the (n, v, D, λ) domain, and (3) to understand the energy minimization mechanisms and propose a relationship between energy and the geometric characteristics of the crack mosaic.

The following sections provide an overview of the current understanding of the mechanics behind columnar joint formation. This is followed by a description of the simulation model used for studying columnar joints. We then present and analyze the simulation results, focusing on the trajectory within the (n, v, D, λ) space. Subsequent sections evaluate the system's energy changes and propose a relationship between these energy changes and the geometric features of the crack mosaic. Finally, the conclusions are summarized.

3.1.1 Formation of Columnar Joints

As lava cools and solidifies, its upper surface contracts, breaking into polygons. The sides of these polygons form cracks that meet at T-junctions. These cracks create gaps that allow gases and fluids to circulate through convection, which further cools the lava within the polygonal boundaries, promoting additional solidification. As molten lava comes into contact with the cooler atmosphere, it contracts and forms crack patterns on the surface. Initially, this contraction leads to a disordered mosaic of cracks with T-junctions, which is attributed to inherent defects or heterogeneities in the system that act as crack nuclei [24]. Systematic studies of basalt fracturing [42, 43] support the thermal cracking hypothesis of columnar joints. These joints serve as conduits for convective heat flow from the hot interior to the cooler atmosphere, with the convective medium typically being gases and vapor. Thicker columns are expected to retain higher temperatures at their centers compared to slimmer columns, as the cooling rate of a cylinder is inversely proportional to its diameter. Heat loss from the column interiors primarily occurs through conduction to the crack front, meaning that columnar joints cool via a combination of convection and conduction processes. Figure 3.2(a) illustrates a schematic of these cooling processes.

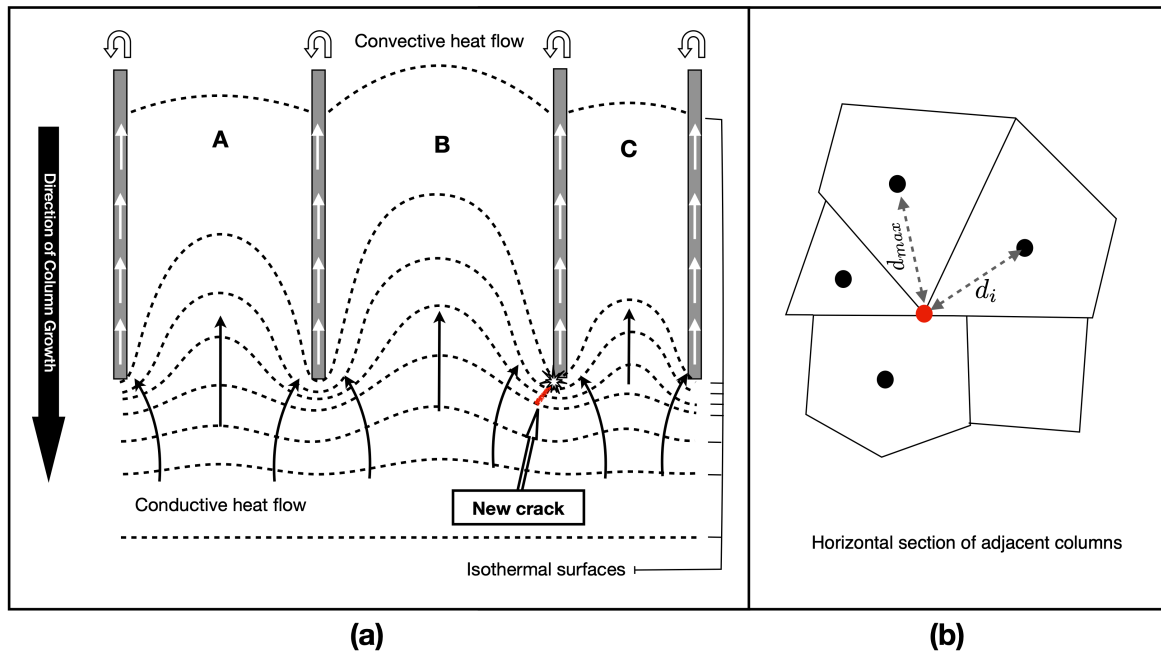


Fig. 3.2 (a) Convection flow cooling, represented by white arrows, occurs within the crack joints, while conduction cooling, shown by black arrows, takes place across the column's interior. The isotherms are indicated by dashed lines. *Figure adapted from [37]*. The red line illustrates the deviation of the growing crack toward the direction of the wider column. (b) A schematic diagram for estimating $d_{i(max)}$ in Eq. (3.1) is presented. The diagram represents a horizontal cross-section of adjacent columns meeting at a single point. Black circles depict the centroids of neighboring polygons surrounding the node, which is marked by a red circle.

Assuming heat is evenly removed from all crack fronts, the isothermal surfaces appear as paraboloids centered on the columns [see Fig. 3.2(a)] and become concentrated at the advancing crack tip, resulting in a higher density of isothermal curves in that area. This concentration leads to increased heat flow near the crack tips.

The consistent alignment of the long-axis directions of the polygons indicates that tensile stresses in the transverse plane of the crack front are statistically isotropic. This isotropic stress field is sustained on a larger scale by a fluid system circulating vertically through the three-dimensional network. However, on the scale of individual columns, the local stress field at the crack segment between columns is influenced by both mechanical and thermal stresses. For cooling lava, the dominant stress contribution at the crack tip is influenced by the thermal gradient. This gradient arises from the high temperature at the center of the cooling column and the relatively cooler crack front, with conduction being the primary cooling mechanism. Since crack faces are stress-free planes, new cracks tend to intersect older cracks in the direction of the greatest stress release, which aligns with the direction of the highest thermal gradient.

Consequently, crack advancement tends to cut into the hottest (and thus thickest) columns common to the crack front, as shown in Fig. 3.2(a).

As crack joints propagate, the isothermal surfaces are again modified by convective cooling along the network of crack fronts. Thus, columnar joint formation is a cyclic process, with each crack advancement influenced by both convection and conduction heat flow. Field measurements [44] show that the cooling front advances in a quasi-steady manner, evident in the distinct changes in the orientation and width of column faces along their length.

The next sections will explain the methodology used to simulate 3-dimensional columnar joints and the logistics that establish the relationship between the iso-perimetric ratio and energy as the joint system undergoes energy minimization.

3.2 Simulation of Columnar Joints

In the 3-dimensional columnar joint simulations, the disordered crack pattern on the top surface of a cooling lava system is replicated by creating a polygonal mesh of cracks based on a specified density and distribution of crack seeds. The 2-dimensional tessellation of the surface is carried out using (a) the Gilbert algorithm and its variants and (b) the Voronoi algorithm. Variations in the disordered crack mesh pattern are introduced by altering the distribution, density, and orientation of the crack seeds. The evolution of this polygonal crack mesh simulates successive transverse layers of a columnar joint system as it progresses vertically downward from the surface layer.

Although the stress field at the tip of an advancing crack front includes contributions from various stresses beyond thermal stress, thermal stress predominates in the case of cooling molten lava. The model assumes that the advancement of the crack front is solely guided by the intensity of the thermal field. It is presumed that all crack fronts on a transverse plane are at the same temperature, with the highest temperature within a polygon occurring at the centroid. In a transverse horizontal section of the system (see Fig. 3.2), the centroids of the polygons, being further from the cooler boundaries, represent the highest temperature within each polygon and are termed ‘thermal stress points.’ This temperature distribution is illustrated in a vertical section of the system in Fig. 3.2(b).

A crack node shared by multiple polygons is influenced by each of their thermal fields. According to previous discussions, the thermal field intensity at any point on the polygonal boundary (crack front) is greatest in the thickest polygon it intersects. The model assumes that the vertical advancement of a crack edge at any time step is determined solely by the movement of its two end nodes. Stochasticity in node movement is factored in, with node displacement being influenced by the thermal field gradient. One of the centroids of the neighboring polygons

is chosen randomly, with the probability proportional to its distance from the node, thus favoring movement towards the farthest centroid. The node is then moved towards this centroid by a fraction κ of the distance from the centroid to the node, d_n , adjusted by a factor $\frac{(d_{i(max)} - \bar{d})}{d_{i(max)}}$. Here, $d_{i(max)}$ represents the maximum distance between the node and a centroid among its neighboring polygons [see Fig. 3.2(b)], \bar{d} is the average distance, calculated as $\bar{d} = \frac{\sum_{i=1}^M |d_i|}{M}$, and M is the number of neighboring polygons sharing the node. This factor accounts for the correlation of thermal stresses at a node due to its neighboring polygons and columns. Thus, in a time-step, a node is moved by Δx following

$$\Delta x = \kappa \frac{(d_{i(max)} - \bar{d})}{d_{i(max)}} d_n \quad (3.1)$$

and in the direction of d_n .

All nodes in the crack mesh are updated according to a parallel updating protocol. At each time step, the values of n , v , D , and λ are recorded. The process begins with estimating Δx for each node in the crack mesh according to the specified protocol and concludes with shifting the nodes accordingly. The crack mesh is considered to be mature when the difference between successive node positions in the transverse plane at consecutive time steps is less than or equal to a threshold value δ . In the simulation, δ was set to 10^{-5} .

The periodic transverse striations seen in real columnar joints suggest that their vertical growth occurs in intermittent phases. In the simulation, the duration of each time step represents the time needed for the cooling crack joints to advance from one layer of cracks at quasi-equilibrium to the next. The updated crack mosaic configuration at each time step reflects the geometry of a transverse layer of the columnar joint. Figure 3.3(c) illustrates that columns can twist as they grow downward, a phenomenon observed in nature. Figure 3.3(d) reconstructs the progression of a single column in the joint system by sequentially placing the time development of a specific polygon from the mesh. An animation illustrating the evolution of the crack front can be found in Ref. [45].

Our simulation algorithm does not account for the creation or termination of new columns, as nodes are neither added nor removed. While such events are rare in real columnar joint systems, they may occasionally be observed.

3.3 Energy Minimization and Evolving Columnar Joints

It is well-established that a regular polygon with more than six sides cannot tile a plane without gaps. Among all regular, close-packed polygonal patterns, the hexagonal arrangement is notable

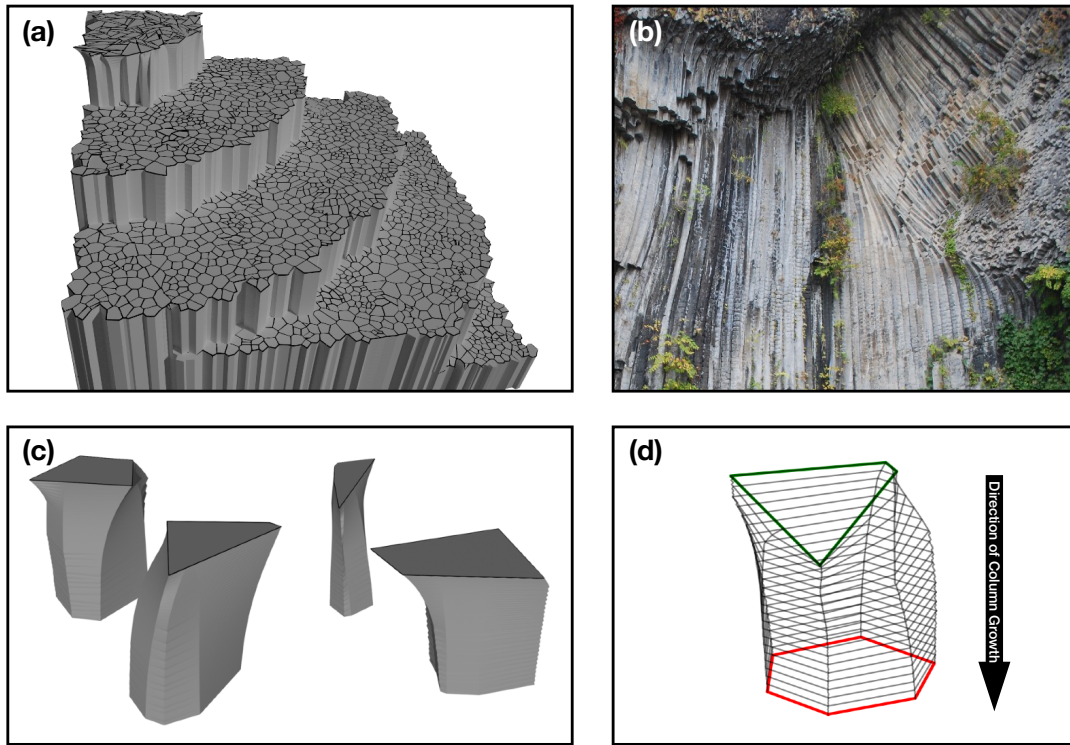


Fig. 3.3 (a) Simulated 3-dimensional columnar joints, with step-wise sections showing their time development. (b) Natural columnar joints located in Genbudo Geo-Park, Japan. (c) Time progression of several independent columns within the crack mesh. (d) The evolution of a single columnar joint, tracked from its initial polygonal shape (highlighted in green) to its final matured form (highlighted in red).

for having the smallest crack perimeter for a given area [46], as evident from the formula for λ in Eq. (2.4) when applied to a hexagon. This characteristic explains why columnar joints, which start with a disordered crack pattern, tend to evolve into a nearly hexagonal arrangement as they mature [47].

Jagla et al. [38] introduced an empirical crack energy functional, ξ , given by

$$\xi = \gamma \sum_i A_i^{\nu} + \sigma L. \quad (3.2)$$

where A_i represents the area of the i^{th} crack ped, L denotes the total crack length, γ and ν are free parameters with appropriate dimensions, and σ is the fracture energy per unit length. Jagla et al. used $\nu = 2$ in their analysis and demonstrated that the minimum value of Eq. (3.2) is achieved by a perfect hexagon.

Observations of columnar joints in nature reveal that the initial polygonal crack mesh on the top surface of basaltic columns does not initially exhibit the well-ordered hexagonal tiling seen in the transverse plane of mature columns. Over time, the polygonal geometry evolves into a hexagonal pattern. Since natural systems tend to seek a minimum energy configuration, there is a reasonable expectation of a correlation between the shape evolution of columnar joints and energy minimization. This study aims to establish a relationship between the shape of the polygonal mesh, as measured by the isoperimetric ratio λ , and the energy E of the column at each stage. In the model, this involves calculating λ and E at every simulation time step.

Crack evolution in columnar joints involves two distinct fracturing processes occurring on different planes. The first process occurs on the top surface, where cracks initiate at nucleation sites once the maximum stress is exceeded. These fractures then propagate horizontally, influenced by local surface inhomogeneities. According to fracture mechanics principles, a crack of length l relieves the accumulated stress in a region of approximately the same length scale $\approx l$ around it [24]. Consequently, the area A of a crack ped is roughly proportional to l^2 . This area A is influenced by factors such as the elastic modulus of the system and contributes to the periodic patterns often observed on cracked surfaces. We refer to the energy expended in fracturing the horizontal plane as E_1 .

The second fracturing process occurs in the vertical plane. When a fracture extends slightly beyond neighboring fractures, stress concentrates at the fracture tip, facilitating its further advancement. In cooling lava columns, the temperature gradient increases ahead of the fractures. As a fracture progresses, it quickly encounters regions with a lower temperature gradient, which hinders further advancement. This leads to a sequential vertical advancement of fractures, termed as the sequence step with distance δz for a very small advancement. The energy associated with this vertical fracturing process is referred to as E_2 . Since all points along the total crack length contribute to the vertical advancement, E_2 is directly proportional to the total crack length L on the plane. For a sufficiently small advancement, each δz can be assumed to be equal. Therefore, for each crack front advancement, a volume of approximately $A \times \delta z$ becomes stress-free.

At any given time step, the total energy E can be expressed as: $E = E_1 + E_2$, i.e.,

$$E = \sum_i \gamma A_i + \sigma L \quad (3.3)$$

Here, L represents the total crack length, γ is a function of elastic constants with units of stress per unit length, and σ is the crack energy per unit length, which is a material constant. The index i spans all the crack peds in the mesh. As columnar joints often begin with 90° crack joints and mature to 120° crack joints, this progression suggests that the system's transition towards

energy minimization is related to changes in λ , which defines the shape of the crack ped. Given that the total crack length L is related to the perimeter of the crack peds by $L = \sum_i l_i/2$, Eq. (3.3) can be expressed in terms of λ using Eq. (2.4), resulting in:

$$E = \sum_i [\gamma A_i + \sigma' \sqrt{A_i}/\lambda_i] \quad (3.4)$$

Here, the index i runs over the total number of crack peds on any transverse plane. Since the crack lines are very thin compared to the areas of the peds, the total crack ped area can be approximated as constant. Under this assumption, Eq. (3.4) allows us to propose an empirical relation for the energy in terms of the average λ of the mosaic as follows:

$$E = \alpha \lambda^{-\beta} + c \quad (3.5)$$

Here, α and β are parameters, and c is a system constant. The rate of change of the system's energy as the columnar joints evolve can be expressed as:

$$\frac{dE}{dt} = -\alpha \beta \lambda^{-\beta-1} \frac{d\lambda}{dt} \quad (3.6)$$

Thus, Eqs. (3.5) and (3.6) together describe the relationship between the geometry of the transverse polygonal mesh and the energy expended in forming it.

To evaluate how well our proposed relation of energy as a function of λ [Eq. (3.5)] compares with other energy models for columnar joints, we can perform the following steps:

1. **Estimate Parameters:** At each time step of our simulation, compute the crack ped area, crack length, and λ of the crack mosaic.
2. **Apply Jagla's Energy Functional:** Use these estimates to calculate the energy functional proposed by Jagla et al. using Eq. (3.2).
3. **Compute Rate of Change:** Determine the time rate of change of Jagla's energy functional ξ .
4. **Compare with Our Model:** Compare this rate of change with the corresponding change in total energy obtained from our model, as given by Eq. (3.6).

By comparing these values, we can assess how well our proposed energy relation aligns with or improves upon Jagla's energy functional for modeling the evolution of columnar joints.

3.3.1 Geometrical Energy of Crack Planes

For each polygonal region, we can define a function ε_i as follows: $\varepsilon_i = \int_{x \in \Omega_i} w(x) \|x_i - x\|^2 dx$. Here, $\|\cdot\|$ represents the Euclidean norm in \mathbb{R}^2 , $w(x)$ is a density function, and $\{x_i\}_{i=1}^n$ are points on the polygonal plane. The integration is carried out over the entire area of the polygon Ω_i . The geometrical energy function of the tessellation can then be obtained by summing this function for all polygons in the tessellation.

$$\varepsilon = \sum_i \varepsilon_i = \sum_i \int_{x \in \Omega_i} w(x) \|x_i - x\|^2 dx \quad (3.7)$$

The relationship between the geometrical energy defined in Eq. (3.7) and the crack energy (E) becomes clear when ($w(q)$) is interpreted as the energy density. For this energy function to be minimized, the tessellation must be a Centroidal Voronoi Tessellation with $\{x_i\}_{i=1}^n$ as the seed points [48].

To evaluate the system's progress toward energy minimization, the geometrical energy of the polygonal mesh at each simulation time step can be computed and graphed against time. By creating the Voronoi polygonal mesh at each step, the corresponding geometrical energy can be determined. This allows for comparison between the time development of Eq. (3.6) and the rate at which the geometrical energy changes as the system progresses toward its final state.

3.4 Results and Discussion

This work simulates various columnar joint systems and compares the resulting structures with those found in nature. The initial polygonal crack patterns on a square plane were generated using variations of the Gilbert tessellation, incorporating different crack orientations and seed distributions. The columnar joints were then allowed to evolve until they reached maturation.

Figure 3.3(a) shows a typical image of 3-dimensional columnar joints generated by the described algorithm, which closely resembles natural columnar joints depicted in Fig. 3.3(b).

Figures 3.3(c) and (d) illustrate the time progression of individual columns within the mesh from their formation to maturity, highlighting how the columns twist as they evolve toward a hexagonal shape.

Tracking the (n, v, D, λ) Trajectory of Columnar Joints

The first rows of Figs. 3.4 and 3.5 display the transverse sections of columnar joints for uniform and normal crack seed distributions, respectively. Different crack patterns were generated by varying the crack orientation for each seed distribution, as indicated by the Roman numerals

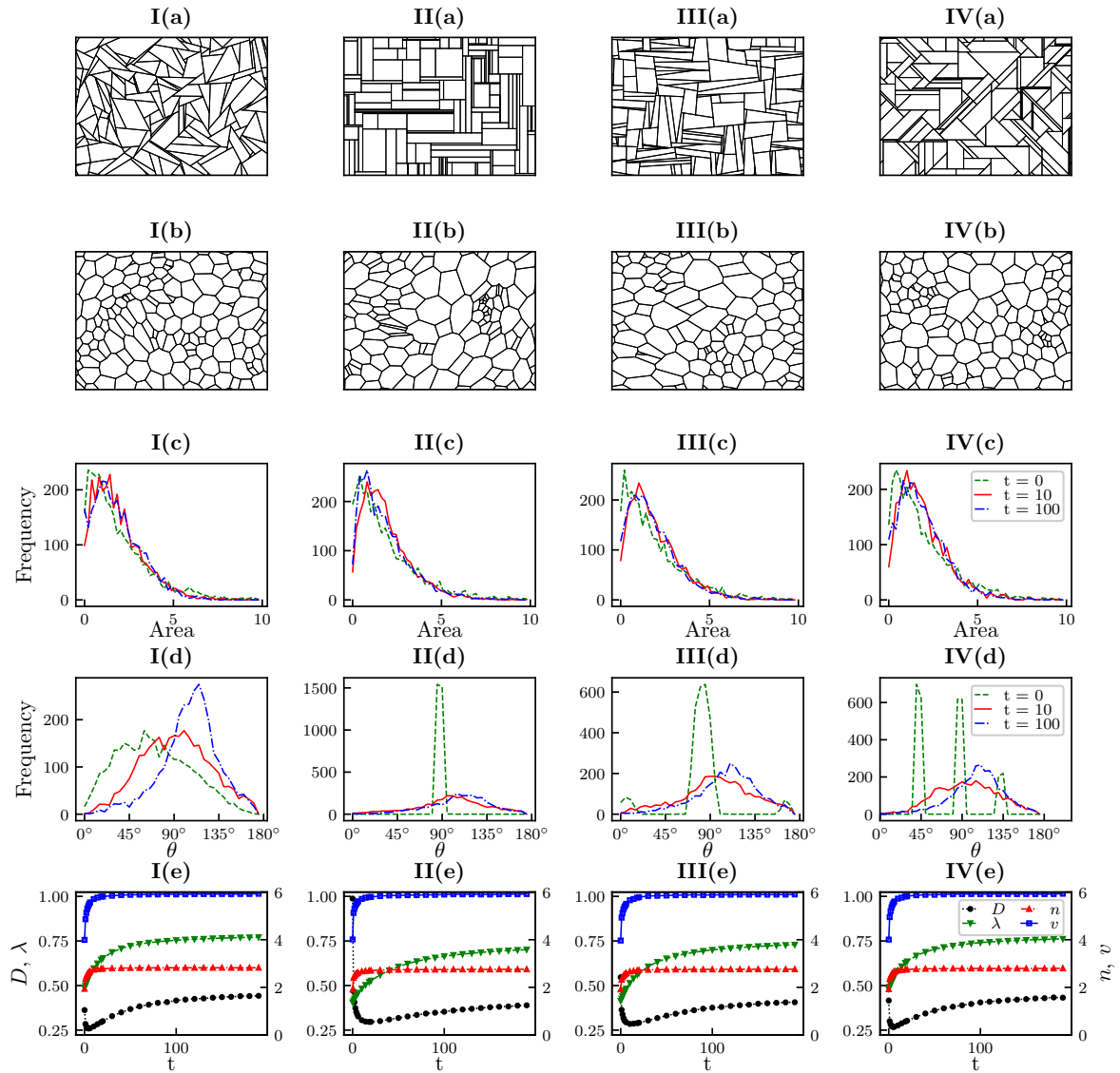


Fig. 3.4 Characteristics of crack mosaic dynamics following Gilbert tessellation with uniform seed distribution. Variation in crack orientation with respect to the horizontal axis: (I) Random, (II) Parallel, (III) $\pm 10^\circ$, (IV) 45° and 90° . (a) Crack mosaic at the start ($t = 0$). (b) Crack mosaic at maturation. (c) Crack ped area distribution at $t = 0$, $t = 10$, and $t = 100$. (d) Distribution of average polygonal angle of crack ped at $t = 0$, $t = 10$, and $t = 100$. (e) Time development of average n , v , D , and λ . For figures in rows (c) and (d), green, red, and blue denote distributions at $t = 0$, $t = 10$, and $t = 100$, respectively.

(I-IV). The mature crack mosaic patterns for each simulation variation are shown in the second row of Figs. 3.4 and 3.5.

In the third row (c) of Fig. 3.4, the crack ped area distribution shows minimal change, with only a slight sharpening of the peak as the cracks mature. This suggests a relatively stable

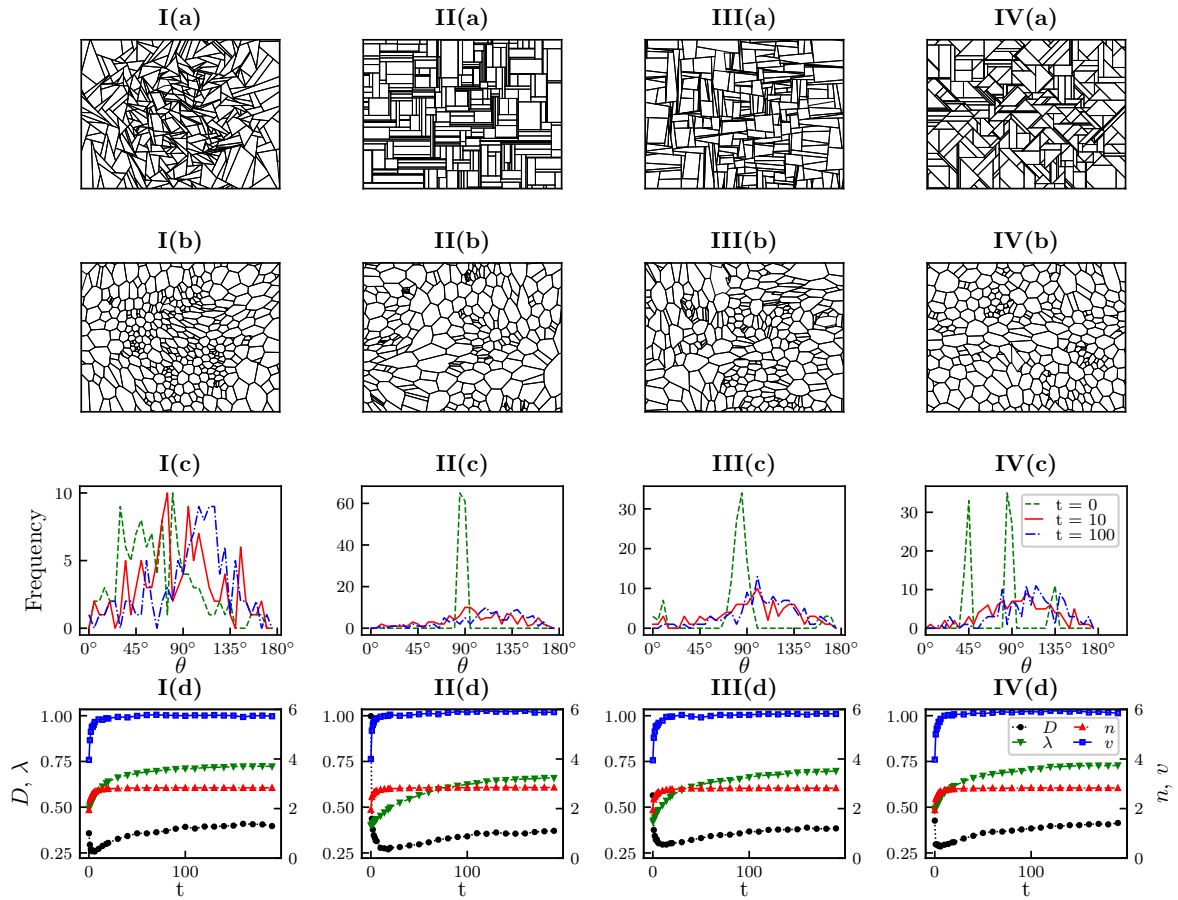


Fig. 3.5 Characteristics of crack mosaic dynamics following Gilbert tessellation with normal seed distribution. Variation in crack orientation with respect to the horizontal axis: (I) Random, (II) Parallel, (III) $\pm 10^\circ$, (IV) 45° and 90° . (a) Crack mosaic at the start ($t = 0$). (b) Crack mosaic at maturation. (c) Distribution of average polygonal angle of crack ped at $t = 0$, $t = 10$, and $t = 100$. (d) Time development of average n , v , D , and λ . For figures in row (c), green, red, and blue denote distributions at $t = 0$, $t = 10$, and $t = 100$, respectively.

crack area distribution over time. However, regardless of the initial crack orientation or seed distribution, a distinct peak at 120° emerges at maturation ($t = 100$), as seen in Fig. 3.4(d), indicating that the Y-junctions characteristic of mature columnar crack joints are successfully reproduced in the simulation.

Figure 3.4(e) presents the time development of topology and geometry measures for each simulation case. The values of (n, v) rapidly increase from $(2, 4)$ to $(3, 6)$ within the first few time steps and then remain nearly constant. The geometric measure D decreases sharply at first, then increases to a constant value following a power-law trend. The isoperimetric ratio λ steadily rises to approximately 0.75, indicating the approach to a near-hexagonal shape. This pattern holds true across all cases studied, regardless of the initial shape of the polygons.

Fig. 3.5 illustrates similar behavior for columnar joints simulated with Gilbert tessellation but using a normal seed distribution.

When comparing Figs. 3.4 and 3.5, it is clear that although the initial crack mosaics differ due to the different seed distributions, the dynamics of crack maturation are quite similar. Differences in crack evolution are reflected in the time evolution of the geometric measures D and λ . Despite the variation in starting configurations, the similarity in the saturation values of all measures suggests the existence of a unique configuration for (n, ν, D, λ) in columnar joints. The effect of the different initial crack mosaic configurations is primarily observed in the trajectory of the corresponding (n, ν, D, λ) point in \mathbb{R}^4 , as depicted in Fig. 3.6. Figures 3.6(a-h) demonstrate the transition from $(n, \nu) = (2, 4)$ to $(n, \nu) = (3, 6)$, confirming that the crack tiling on the transverse plane of columnar joints evolves from a Gilbert-like pattern to a Voronoi-like pattern upon maturation. In contrast, Fig. 3.6(i) does not exhibit a prominent trajectory since it illustrates the evolution of a crack system that begins with a Voronoi polygonal mesh. This specific case will be discussed further in the following section.

The characteristics of columnar joints simulated using Voronoi polygonal tessellation with a uniform seed distribution are presented in Fig. 3.7. Since crack evolution using a normal seed distribution did not display significant differences, those results are not discussed here. In the (n, ν, D, λ) domain shown in Fig. 3.6(i), both the initial and final points lie on $(n, \nu) = (3, 6)$, as anticipated. This is because the crack mosaic at the formation stage of the joint system was generated using the Voronoi algorithm.

Energy Analysis

An examination of Fig. 3.4(c) reveals that the crack area of the evolving mosaic remains relatively stable over time. This observation supports the assumption of constant area in the construction of Eq. (3.5). To test our hypothesis that the system progresses towards energy minimization, as reflected in the changing polygon shapes, the total crack length L and the average isoperimetric ratio λ are plotted against time.

Figure 3.8 illustrates that both L and λ follow a power-law relationship with time (t), described by the equations:

$$L \sim a_L t^{-b_L}. \quad (3.8)$$

and

$$\lambda \sim a_\lambda t^{b_\lambda}. \quad (3.9)$$

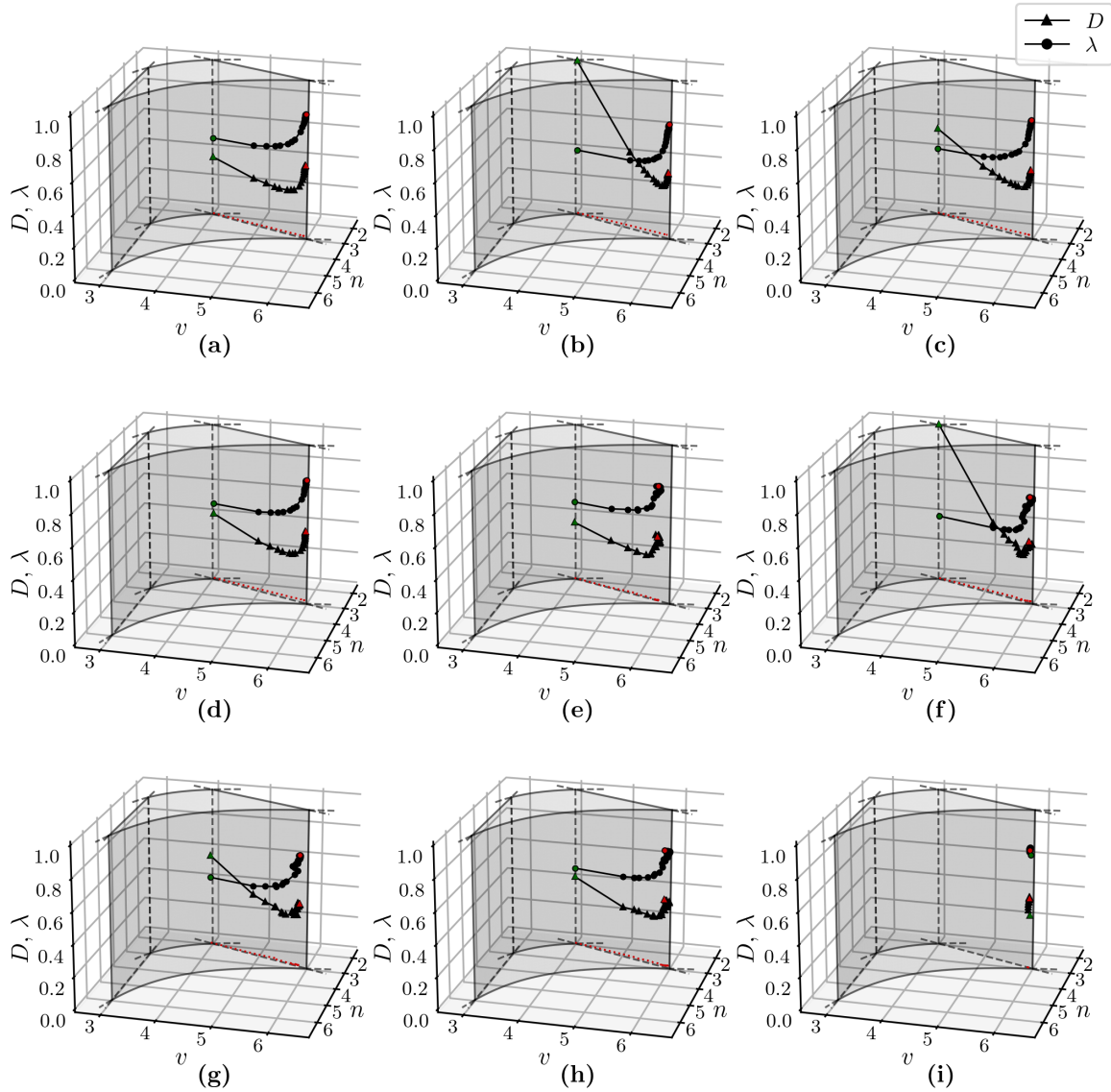


Fig. 3.6 Trajectory of the crack in the (n, v, D, λ) domain: Gilbert cracks with uniform seed distribution and crack orientation - (a) random (b) parallel (c) $\pm 10^\circ$ (d) 45° and 90° ; Gilbert cracks with normal seed distribution and crack orientation - (e) random (f) parallel (g) $\pm 10^\circ$ (h) 45° and 90° ; (i) Voronoi cracks.

By substituting the expressions for L and t from Eqs. (3.8) and (3.9) into Eq. (3.3), the equation can be rewritten in terms of λ , leading to Eq. (3.5). The parameters α and β in Eq. (3.5) can also be derived from the simulation data and are found to be

$$\beta = \frac{b_L}{b_\lambda} \quad (3.10)$$

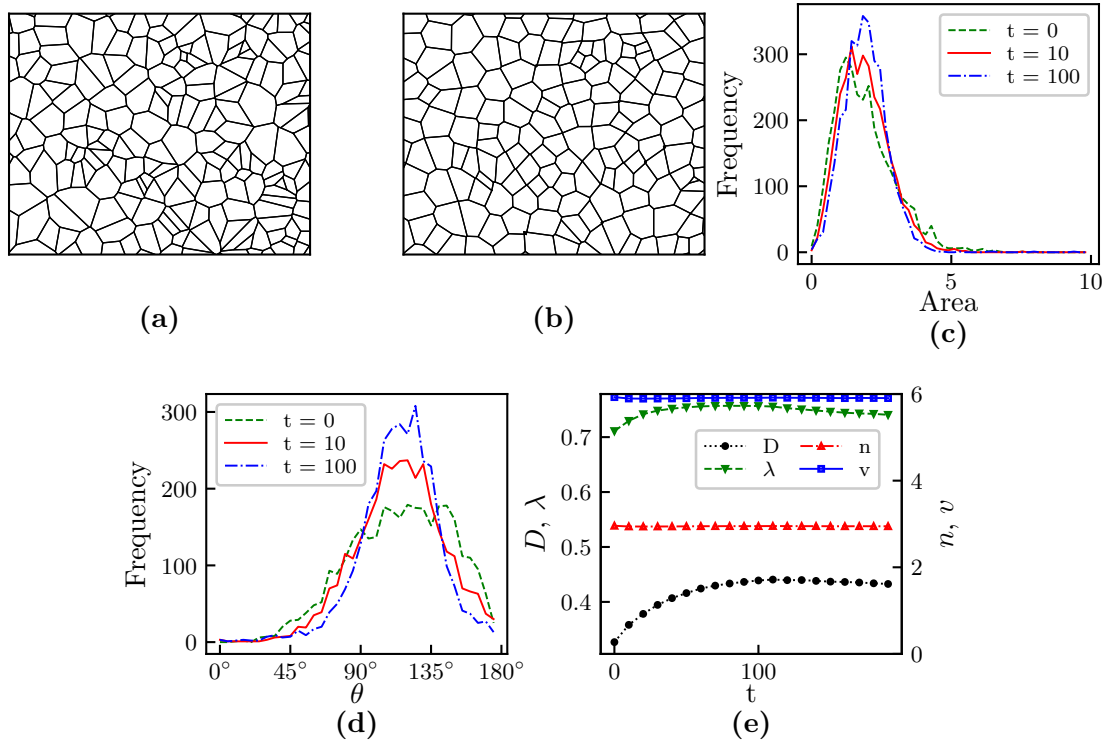


Fig. 3.7 Characteristics of crack mosaic dynamics following Voronoi tessellation with uniform seed distribution. (a) Mosaic at $t = 0$. (b) Mosaic at $t = 100$. (c) Time variation of the histogram of crack ped area. (d) Time variation of the histogram of the average internal angle of crack ped. (e) Time development of n , v , D , and λ .

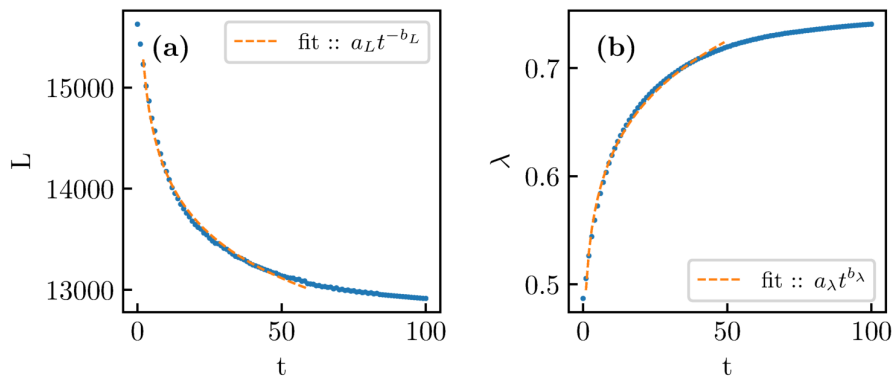


Fig. 3.8 Power law fitting of (a) crack length, L and (b) λ

and

$$\alpha = \sigma a_L a_\lambda^\beta \tag{3.11}$$

This confirms that the proposed empirical relationship between the energy of the columnar joint system and the shape parameter λ , which was derived from heuristic arguments, aligns with the results obtained from the simulation.

To validate our model, we calculated the total energy at every time step for all simulations of columnar joints using Eq. (3.5), as shown in Fig. 3.9(a). The values of α and β were derived from Eqs. (3.10) and (3.11) for the different mosaics studied, which are listed in Tab. 3.1. The exponent β has an average value of approximately 0.3, with its variation potentially due to changes in crack orientation. The parameter α shows consistency in magnitude across all seed distributions. To further compare our results with the empirical expression proposed by Jagla et al., Eq. (3.2), we plotted the energy evolution for crack mosaics with uniform seed distribution and random orientation in Fig. 3.9(b), as a representative example. The fits were nearly exact across all mosaic configurations studied. The goodness of fit across all simulation

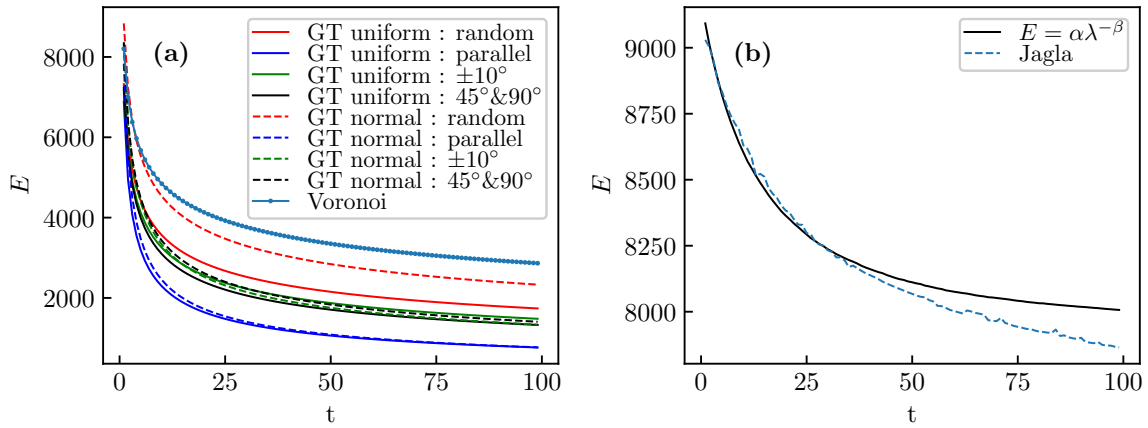


Fig. 3.9 (a) Trajectory of energy E based on Eq. (3.5) for various initial mosaics. (b) Comparison of energy minimization trajectories using Eq. (3.2) and Eq. (3.5) for the initial mosaic generated with Gilbert tessellation, featuring a uniform seed distribution and random crack orientation.

variations indicates that when the crack area remains approximately constant, monitoring the time evolution of columnar joints can be effectively achieved by tracking changes in the shape parameter λ alone.

According to Eq. (3.6), a typical plot of the rate of change of the isoperimetric ratio, $d\lambda/dt$, versus time, t , mirrors the change in the energy functional described by Eq. (3.2), as shown in Fig. 3.10(a). This indicates that energy minimization is primarily accomplished through adjustments in crack length and polygonal shape within the transverse plane of the crack mosaic as the columnar joint progresses toward maturation.

Table 3.1 Values of α and β obtained from Eqs. (3.10) and (3.11) for the energy estimations.

Model	distribution & orientation	α	β
Gilbert	uniform-random	7323	0.31
Gilbert	uniform- $\pm 10^\circ$	7162	0.34
Gilbert	uniform-45&90 $^\circ$	7233	0.37
Gilbert	uniform-parallel	6887	0.48
Gilbert	normal-random	8836	0.29
Gilbert	normal- $\pm 10^\circ$	8323	0.39
Gilbert	normal-45&90 $^\circ$	8369	0.39
Gilbert	normal-parallel	7834	0.50
Voronoi	uniform-random	8204	0.23

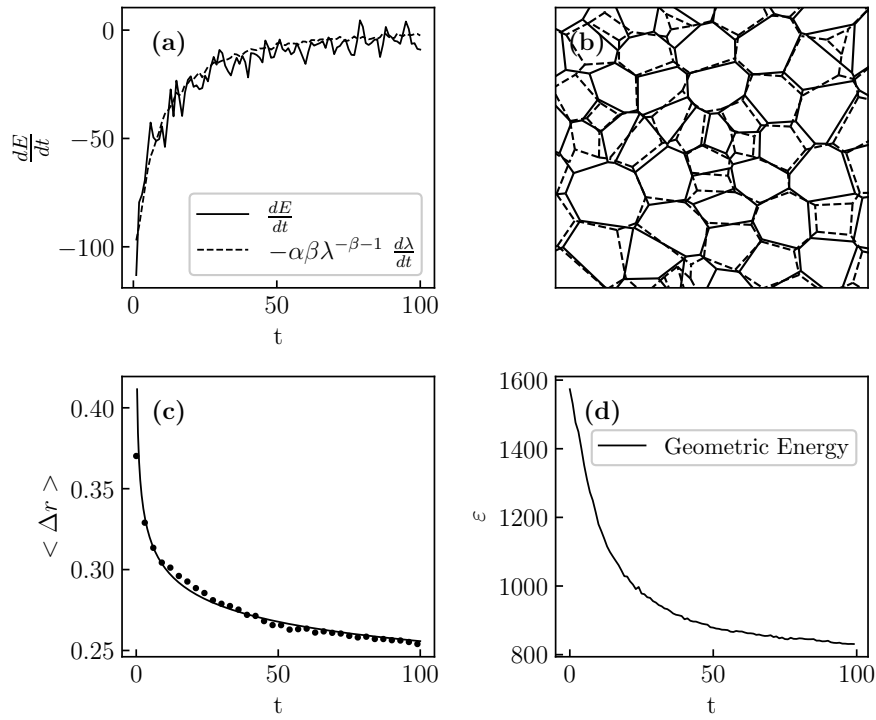


Fig. 3.10 (a) Plot of dE/dt against $d\lambda/dt$. (b) Comparison between the columnar joint pattern (dashed line) and the Voronoi mosaic (solid line) created from the centroids of matured columns. (c) Change in $\langle \Delta r \rangle$ over time t . (d) Geometric energy ε trajectory as described by Eq. (3.7).

Equation (3.7) predicts a minimum energy configuration for systems with Voronoi polygons, while the initial crack mosaic in our simulation does not necessarily conform to this structure. To verify whether the maturation of the simulated columnar joint system aligns with the minimization of geometric energy, the centroids of the polygons in the transverse mosaic at each time step were used as seeds to construct corresponding Voronoi polygons, as shown in

Fig. 3.10(b). The difference in distance, Δr , between the centroid of the Voronoi polygon and its seed was calculated, and the average difference, $\langle \Delta r(t) \rangle$, was estimated for all polygons in the mosaic at each time step. The variation in the geometric energy of the evolving crack mosaic was found to correlate with the variation of $\langle \Delta r(t) \rangle$ over time, as expected, Fig. 3.10(c).

The geometric energy of the transverse crack plane in the columnar joints was estimated at each time step using Eq. (3.7). The results for the change in geometric energy for the case of columnar joints starting from a uniform seed distribution with randomly oriented cracks are plotted as a function of time in Fig. 3.10(d). For the calculations, the density parameter $w(q)$ was set to unity. The curve shows a decrease in energy over time, tending toward a minimum as the mosaic transitions into a Voronoi-like structure.

3.5 Conclusions

The time evolution of columnar joints reveals several intriguing dynamics, particularly in the crack mosaics within the transverse plane. Initially, these mosaics are characterized by T-junctions, which evolve into Y-junctions as the lava cools and the joint system matures. For the first time, this study maps the evolution of both the topology and geometry of crack mosaics as a trajectory in the (n, v, D, λ) domain. By simulating 3-dimensional columnar joints formed through cooling lava using a stochastic model, we introduce variations in initial crack mosaics to reflect material heterogeneity. Variations in crack seed distribution and orientations simulate the preferred cleavage planes of minerals in basaltic rocks, demonstrating that the trajectory in the (n, v, D, λ) space depends on both factors. This method of analyzing time-dependent topology-geometry evolution offers a novel approach to distinguishing between different columnar joint systems and holds potential for application to other complex dynamical systems.

The evolution of hexagonal tiling in the transverse sections of mature columnar joints is captured by an empirical relationship linking the geometry of the crack mosaic to the system's energy changes. Building on fracture mechanics and the underlying physics of columnar joint formation, we propose an empirical relation between system energy and the shape parameter λ . The total system energy follows a power-law dependence on λ , with an exponent β that averages around 0.3 but ranges from 0.2 to 0.5 across simulations (as detailed in Tab. 3.1). Both the coefficient α and the exponent β are derived from the stochastic model. At crack maturation, λ stabilizes around 0.75, regardless of the initial mosaic configuration. Validation of this model is achieved by aligning the proposed energy evolution with existing energy estimates from the literature. Unlike previous methods that relied on challenging estimations of individual polygon statistics, our model ties the system's energy to the average shape of the

crack mosaic, providing a clearer connection between visible geometric changes and energy dynamics over time. While traditional energy minimization methods often use Monte Carlo techniques, our simulation naturally reorganizes the crack mosaic's geometry according to fundamental physical principles, leading to an energy-minimized state.

In applying topological concepts to these findings, we draw parallels between the geometric energy of plane polygonal meshes and the physical energy of the columnar joint system. Minimizing the geometric energy for centroidal Voronoi diagrams – a well-known result in topology – serves as a useful analogy. We estimate the geometric energy of the polygonal mosaics over time and show that as the system matures, the mosaic becomes more Voronoi-like, moving towards a minimum geometric energy state. The consistency between this geometric evolution and the physical energy estimates derived from the model further reinforces its validity. This work not only advances our understanding of the physical processes governing columnar joint formation but also provides a robust framework for studying energy dynamics in complex polygonal systems.

Chapter 4

Voronoiness of Crack Patterns

4.1 Introduction

Mathematically, a Voronoi diagram divides a plane into regions around a set of points called generators. These regions, known as Voronoi regions, are defined as having every point within a region closest to its corresponding generator or seed. This property makes Voronoi diagrams particularly interesting, as they have diverse applications in physical systems. In real-world scenarios, the seeds represent critical points that influence the tessellation process. For example, during the 1854 cholera outbreak in Soho, physician John Snow mapped the outbreak and demonstrated that the most affected area formed a Voronoi region with the contaminated Broad Street water pump as the seed [49].

Crack patterns, or mosaics, prevalent throughout nature, ranging from microscopic biological structures to vast volcanic columnar formations, for example the intricate veins on a dragonfly's wings to the irregular brown spots on a giraffe's fur [50–55], columnar joints, permafrost to salt play show very resemblance to Voronoi diagram. They often involve some form of optimization. For instance, the honeycomb's structure, a Centroidal Voronoi diagram, is designed to maximize the efficiency of wax usage [46]. Yadav et al. [56] proposed a method to identify key Voronoi sites to enhance the structural performance of beams by ensuring uniform stress distribution. Dynamical systems, such as the formation of surface cracks due to permafrost thawing and the development of columnar joints, undergo evolution over decades, ultimately adopting a pattern akin to a Voronoi tessellation [57, 37, 58–60]. The formation of mud crack patterns during summer, characterized by a rough Voronoi tessellation, likely originates from local stress points caused by drying; similarly, the formation of giant columnar joints during the cooling process of basaltic lava sees the highest temperatures at the Voronoi regions' inception points, visible in their cross-section. It has been observed that the formation of columnar joints aims to release the maximum amount of thermal stress to reduce the system's

overall energy [38, 61]. The presence of Voronoi tessellation across various fields including biology [62–65], physics [66–68], architecture, design [69, 70], and fabrication [71–73], highlights the need for further investigation into the fundamental forces driving this geometric formation.

This chapter delves into measuring the Voronoiness of various static and dynamic crack patterns. As a case study, I modeled the evolution of mud crack patterns resulting from repeated wetting and drying cycles. Mud slurries, comprised of large colloidal particles with relaxation times significantly longer (by an estimate of $\approx 10^{10}$ times) than those of other molecules, including clay and lava, showcase the slow dynamical maturation that scientists are able to track due to these prolonged relaxation times. This has led to the utilization of a spring network model by the researchers to simulate the temporal evolution of crack patterns in desiccating clay systems subjected to wetting-drying cycles.

The transformation of the initial geometry of the desiccation crack mosaic with the progression of these cycles until a mature state is achieved has been the subject of prior research. In the previous chapter, we introduced a specific topology-geometry combination (n, v, D, λ) to characterize a crack mosaic [31]; with (n, v) defining the topology and (D, λ) defining the geometry of the crack pattern. Further exploration into these topological and geometrical measures is provided in the subsequent section. This classification of crack mosaics by their (n, v, D, λ) parameters allows for their identification as distinct points within a 4-dimensional topology-geometry space, a subset of \mathbb{R}^4 . Crack mosaics with similar (n, v, D, λ) configurations are grouped together in this space. However, the majority of real-world crack patterns tend to cluster near the Gilbert crack model point, with fewer instances clustering around the Voronoi crack descriptor, leaving considerable portions of the (n, v, D, λ) domain space unoccupied. As reported, the transition in mud crack patterns from featuring an abundance of T-junctions (aligning with Gilbert mosaics) to evolving towards Voronoi-like patterns with Y-junctions over wetting-drying cycles has been meticulously mapped. This transition across the (n, v, D, λ) domain effectively captures and characterizes the development of such complex dynamical systems over time.

To quantify the ‘Voronoi-ness’ of a physical tessellation, we have introduced a measure denoted as p , which offers a heuristic assessment of how closely the tessellation resembles a Voronoi pattern. Additionally, the authors have effectively employed the Hausdorff Metric d_H to assess the deviation of any crack mosaic from a Centroidal Voronoi.

The quantification of the ‘Voronoi-ness’ in terms of p and the Hausdorff Metric over time cycles involves the examination of the crack mosaic’s shape evolution. The patterns observed in our simulations closely resemble real system observations made by physicists and geologists.

It has been observed that the desiccation mud crack mosaics tend to evolve towards a Voronoi tessellation as this minimizes the system's total energy.

The shape and size of the polygons in a Voronoi tessellation are influenced by the distribution of seeds in each region. Identifying the seed of a Voronoi region can be used to establish the range of correlation of a specific physical property, such as the elastic properties of surface cracks. In the context of Centroidal Voronoi tessellations, the seed and the centroid of the corresponding Voronoi region are the same. However, in real crack mosaics, it is not always possible to definitively determine the seeds, and the centroid of the polygon is often used as an approximation for the seed. Therefore, it is interesting to determine the degree of 'Voronoi-ness' in any polygonal network and measure how closely it resembles a Centroidal Voronoi tessellation. We demonstrate that by using both the p measure and the Hausdorff Metric to the corresponding Centroidal Voronoi mosaic, it is possible to determine (a) the degree to which a crack mosaic resembles a Voronoi tessellation and (b) how close a Voronoi region is to be a Centroidal Voronoi tessellation.

In the following sections, I first introduced Measures for the quantification of the 'Voronoi-ness' of a crack mosaic. Then, a simple explanation of the mechanics of desiccation cracks. The simulation model of the wetting and drying dynamics of a clay system is described next in terms of a spring network model based on the mechanics of desiccation cracks. Having established the fundamental theories guiding this work, the results of the simulation are examined in terms of the time evolution of both - the crack mosaic geometry and the system energy. The 'Voronoi-ness' of the crack mosaic is first checked in terms of existing laws and measures of entropy. We follow this up with measures of 'Voronoi-ness' represented in terms of wetting-drying cycles and quantified in terms of defined measures. The preferred 'Voronoi-ness' of desiccating crack mosaics is explained next in tandem with the energy minimization of the system. An examination of a few natural but static crack mosaics is also conducted to check if nature does indeed have any preference for Voronoi patterns in mosaics.

4.2 Theoretical Background

4.2.1 Quantification of Voronoi-ness

Given a finite set of points x_1, x_2, \dots, x_n on a subset Ω of the plane, we define the region Ω_i as $\{x \in \Omega : \|x - x_i\| \leq \|x - x_j\| \text{ for all } j \neq i\}$. A Voronoi diagram with seeds x_1, x_2, \dots, x_n is the mosaic of Ω formed by the regions $\Omega_1, \Omega_2, \dots, \Omega_n$. This creates a polygonal mosaic of Ω with notable geometric properties. A related construction is the Delaunay Triangulation, which is a triangulation of a finite set of points F that satisfies the Empty Circumcircle Property—no point

in F lies inside the circumcircle of any triangle in the triangulation. The Voronoi diagram is the dual construction of the Delaunay triangulation for the same set of points. For further details on the mathematical properties of Voronoi diagrams and Delaunay triangulations discussed here and throughout this work, see [74].

Given a plane mosaic, determining whether it is a Voronoi diagram for a specific set of points is generally a challenging problem, as the seed points are not predetermined. For real-world mosaics, a computationally efficient approach is to treat the centroids of the mosaic regions as seeds of a Voronoi diagram, which can then be compared to the original mosaic. For example, in crack mosaics, the exact location of stress seeds may not be easily determined. As an approximation, the centroids of the polygons can be assumed to act as the seeds. By connecting the centroids of polygons that share a common vertex, the mosaic can be triangulated (see Fig. 4.8). A key characteristic of Delaunay triangulation is that none of the circumcircles of the Delaunay triangles contain any of the seeds within them. This property can be utilized to calculate the fraction of non-empty triangles that deviate from the Delaunay triangulation's criteria. A parameter p can be defined as a heuristic measure of the 'Voronoi-ness' of real crack systems.

$$p = \frac{\text{Number of non-empty circumcircles}}{\text{Total number of the triangles}}$$

A more definitive way to measure the 'Voronoi-ness' is the mathematical tool Hausdorff Metric¹. It measures the distance between two subsets within a metric space. This allows for a comparison between an actual crack and its associated Voronoi diagram, which is created by utilizing the centroids of the crack peds as seeds.[61].

4.2.2 Construction of Voronoi Diagram From a Seed Scatter

Figure 4.1 illustrates the step-by-step process for generating a Voronoi diagram from a set of scattered points (seeds), as seen in Fig. 4.1(a). The first step involves connecting the points to their neighbors to create a Delaunay triangulation, shown in Fig. 4.1(b). Then, circumcircles are drawn around each triangle, as depicted in Fig. 4.1(c). Finally, the circumcenters (marked in red in the online version) of triangles that share a common side are connected, completing the Voronoi diagram in Fig. 4.1(d). If the points coincide with the centroids of the Voronoi polygons, the diagram is known as a *Centroidal Voronoi* diagram.

¹For compact subsets $A, B \subset \mathbb{R}^2$, the Hausdorff Metric $d_H(A, B)$ is defined as $d_H(A, B) = \max\{\max_{a \in A} d(a, B), \max_{b \in B} d(b, A)\}$, where $d(x, C) = \inf\{\|x - c\| : c \in C\}$.

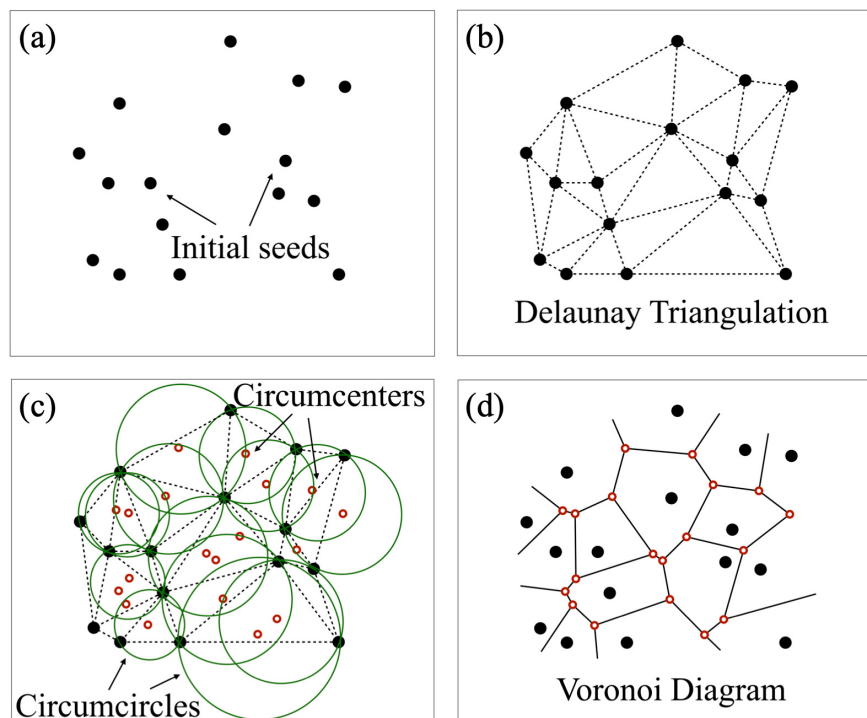


Fig. 4.1 A Voronoi diagram is the dual of a Delaunay triangulation: (a) The seeds used to create the Voronoi diagram, (b) The Delaunay triangulation formed by connecting the seeds, (c) Circumcircles around each triangle, ensuring no seed lies within the interior of any circumcircle. The red points represent the circumcenters of the triangles. (d) Connecting the circumcenters of triangles that share a common side results in the formation of the Voronoi diagram.

4.2.3 Crack Evolution

Most crack patterns found in nature are static, meaning their shapes remain unchanged over time. Such static crack mosaics can vary from the nearly regular hexagonal patterns of honeycombs to the irregular polygonal mud cracks seen in dry agricultural fields and riverbeds. However, if the time scale of crack pattern changes aligns with the experimental or observation time, it becomes possible to observe and track the dynamic evolution of these crack patterns until they reach maturity. There are few instances of natural crack mosaics that undergo dynamic shape changes, eventually maturing into Voronoi-like patterns. Examples include terrain cracks caused by permafrost, columnar joints, and patterns found in salt deserts or dry salt lakes [75]. A similar pattern of crack evolution is observed in the drying of wet corn starch [33, 76, 5]. Laboratory experiments have documented mud cracks undergoing desiccation and repeated wetting-drying cycles, during which the angles between the cracks shift from 90° to 120° [22, 35]. This raises the question of whether the time evolution of such crack patterns leads to Voronoi-like tessellations. We simulate a repeated wetting-drying experiment on mud cracks

using a spring network model [77] to gain deeper insight into the fundamental mechanisms driving these evolving crack systems. We assess the ‘Voronoi-ness’ of the evolving crack pattern using the metrics discussed in the following section.

During the desiccation of mud or other colloidal systems, capillary pressure between the particles increases as evaporation occurs, causing the particles to draw closer together [78]. Micro-cracks form from inhomogeneities that act as crack nucleation sites [24]. When a new crack appears near an existing one, it tends to grow towards the existing crack at a right angle. This occurs because the stress is higher parallel to the existing crack, making it energetically favorable for the growing crack to bend along the direction of the steepest stress release gradient, leading it to meet the existing crack perpendicularly [79]. Consequently, a highly connected crack network forms, dividing the mud surface into rectilinear regions (peds). As the cracks open, they also contribute to surface evaporation, creating a moisture gradient within each ped that increases from the exposed crack face towards the center. The drying front within each ped advances from the crack boundary towards the center. As drying continues, the cracks widen while the ped areas shrink. When the cracked surface is subsequently re-wetted to saturation, the cracks and inter-particle pores refill with water, partially relaxing the elastic strain generated during desiccation. In cases where the mud or clay system undergoes repeated wetting and drying cycles, the vertices where different cracks intersect gradually shift, causing the angles at the joints to change from 90° to 120° . The ‘T’-shaped junctions transform into ‘Y’-shaped junctions, and the crack pattern evolves towards a hexagonal arrangement.

4.3 Simulation of the Wetting-drying Process

As desiccation cracks emerge randomly and propagate along straight lines, we use the Gilbert tessellation [80, 31], a random network, to model the initial crack pattern. Tiny crack tips are initiated from a homogeneous Poisson point distribution of seeds and allowed to grow in randomly selected directions on a 100×100 square plane. The cracks expand in both directions. When a growing edge encounters an existing crack segment, it stops growing and forms a node at the collision point. After the crack network is fully developed, the nodes and distinct crack regions (peds) are identified.

The resulting crack mosaic, along with the dynamics of repeated wetting and drying, is simulated using a connected spring network—a model commonly employed to replicate crack mechanics [81, 13, 82–84]. A brief explanation of the spring model and its relation to elasticity in solids is provided in the App. A. As discussed earlier, the crack faces along the boundary of each ped contribute to surface evaporation. As the drying front of each ped progresses inward over time, this process is replicated by connecting each vertex of the polygon (ped) in the

mosaic to its centroid with a spring of spring constant k , which compresses with each drying time step. The natural length d_0 of the spring is set to the distance between the vertex and the centroid, as shown in Fig. 4.2(a).

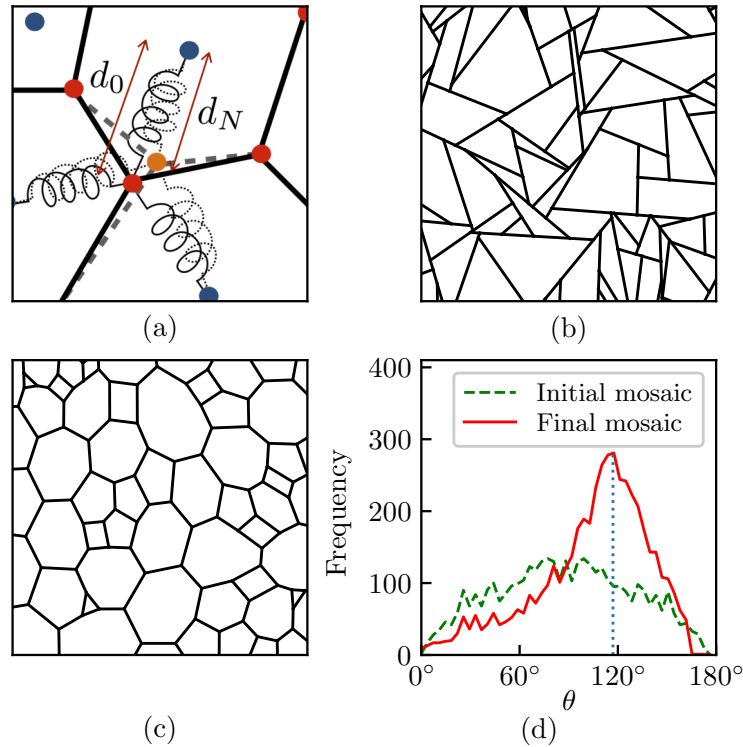


Fig. 4.2 (a) Spring model used to simulate desiccation cracking. The vertices of the crack peds are represented by red circles, and the centroids of the peds are marked by blue circles. The natural spring length d_0 between the centroid (blue) and vertex (red) is indicated by an arrow. A red vertex experiences elastic forces from the surrounding polygons through the springs. After N desiccation steps, the vertex moves to a new position (orange circle) and remains connected to the polygon centroids by springs (shown as dotted lines) with new lengths d_N (also indicated by an arrow). (b) Initial crack network of a desiccation crack. (c) Final matured crack network pattern after repeated wetting-drying cycles. (d) Initial and final frequency distributions of the polygonal angles of crack peds. The final distribution shows a peak around 120° , marked by a blue dotted line.

The evaporation process is influenced not only by ambient conditions but also by the material properties of the colloidal system. The simulation utilizes two time notations: (i) N (or N') and (ii) t . N represents the number of consecutive times a spring is allowed to contract due to drying before it can be wetted again. For instance, $N = 1$ means the system is wetted after one application of the drying rule, whereas $N > 1$ indicates N consecutive drying steps before

the sample is wetted. The prime notation (N') is used to indicate the number of successive wetting steps.

In the simulation, the natural lengths of the springs decrease due to desiccation according to the following relation –

$$d_n = d_{n-1} \left(1 - \frac{a}{b^n} \right) \quad (4.1)$$

where a and b are parameters that control the desiccation process. At the n^{th} desiccation time step, the length of a spring decreases by a factor of $\left(1 - \frac{a}{b^n} \right)$ relative to its previous length. This desiccation rule is based on earlier work by Tarafdar and Dutta [85, 77], where experiments on aqueous clay showed that evaporation typically continued until the mass was reduced by approximately 63% of its original weight. As desiccation progresses and the springs contract, a net force, which is the resultant of the forces from all the springs connected to that node, acts on it, as illustrated in Fig. 4.2(a). The displacement of any node can thus be expressed in terms of the spring length shrinkage as follows –

$$\Delta \vec{x} = \kappa \sum_i \Delta \vec{d}_i \quad (4.2)$$

where the summation runs over all the springs connected to the node. The term $\Delta \vec{d}_i$ represents the shrinkage of the i^{th} spring during a single cycle and is given by $(d_0 - d_N) \hat{n}$, where d_N is the length of the spring after N desiccation time steps, just before the next wetting phase begins. The unit vector \hat{n} points towards the centroid after N drying steps. In our simulations, κ is set to 1, assuming the material is perfectly elastic and defect-free and that particle-particle interactions are restricted to nearest neighbors. The crack evolution during the drying cycle is modeled by displacing the nodes based on the resultant forces, which in turn alters the paths of the crack segments.

During the wetting process, the springs expand, and their natural lengths change over time as follows –

$$d_{n'} = d_{n'-1} \left(1 + \frac{a}{b^{n'}} \right) \quad (4.3)$$

The nodes move similarly during the wetting process as they do during drying. However, since all wetting-drying experiments are conducted by saturating the sample during wetting, we set the number of wetting steps to $N' = 1$ to represent saturation. At the start of the wetting-drying cycle, i.e., at $t = 0$, $n = 1$, and $d_{n-1} = d_0$ in Eq. (4.1). After N drying steps, all springs connected to a single node shrink according to Eq. (4.1), and the node is displaced as per Eq. (4.2). All nodes are updated to their new positions simultaneously. The d_0 value of each spring is reassigned based on the new position relative to its centroid. Wetting, followed by spring

expansion, is then initiated according to Eq. (4.3). A single wetting-drying time cycle t consists of N successive drying steps followed by one wetting step ($N' = 1$). For clarity, the flow chart of one complete wetting-drying cycle is depicted in Fig. 4.3.

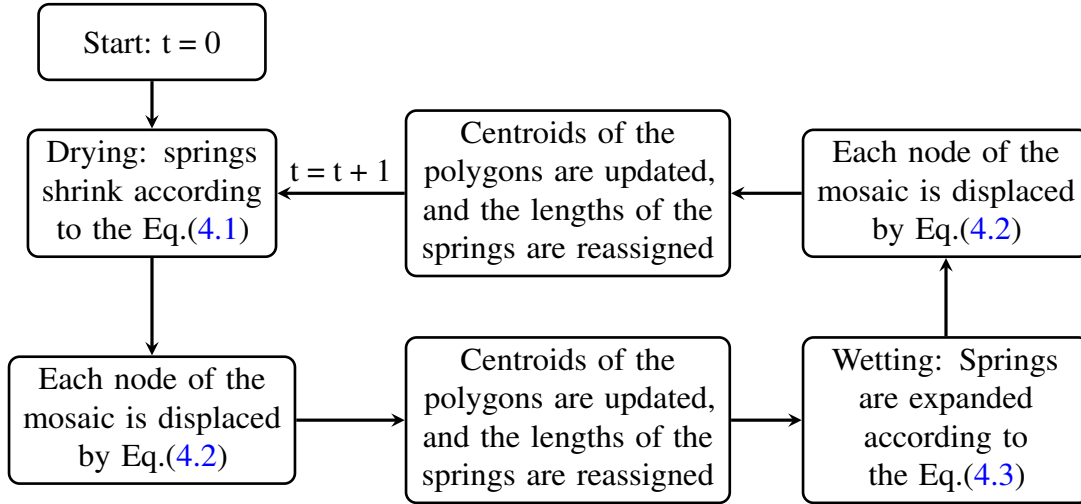


Fig. 4.3 Flow-chart of one complete wetting-drying cycle.

We note that the recursive relation in Eq. (4.1), with $b > 1$ and $a > 0$, forms an infinite product that converges to a positive real number. This convergence physically corresponds to a sufficient number of drying cycles. At the end of each time cycle t , the centroids of the mosaic polygons are calculated, which serve as seeds for constructing a Voronoi mosaic. The Hausdorff metric between the Voronoi mosaic and the crack mosaic is computed at every cycle t .

The wetting and drying cycle is repeated until the difference in displacement of any vertex between consecutive time steps is $\leq 10^{-3}$. At this point, the crack pattern is considered to have matured and ceases to evolve further. Animations showing the movement of crack nodes during wetting-drying cycles, along with the circumcircles of the dynamic triangulation, can be found in Ref. [86].

4.4 Results and Discussion

In the following subsections, we first present the results and discussion on the dynamic evolution of mud cracks under repeated wetting-drying cycles based on our simulation. The topological and geometrical transformations of the crack mosaic are traced through a trajectory in the (n, v, D, λ) domain. We explain the preference for a Voronoi-like pattern at maturation by analyzing the system's energy evolution towards a minimum. The evolution of the p parameter

and the Hausdorff metric over time cycle t are also examined and discussed. Finally, we provide an analysis of some natural crack mosaics, i.e., matured crack patterns, to illustrate that energy minimization is a significant driving force behind the preference for Voronoi geometry in crack mosaics.

4.4.1 Dynamic Progression of Crack Mosaics

$n - v$ domain

Figure 4.2(b) illustrates the initial desiccation crack network, while Fig. 4.2(c) shows its matured state after repeated wetting-drying cycles. These figures were generated using parameter values of $a = 0.05$, $b = 1.2$, and $N = 25$. The simulation was conducted to examine the effects of varying ambient conditions by adjusting a , altering the system's physical properties by changing b , and modifying the periodicity of the wetting-drying cycles by varying N . A higher value of N indicates longer intervals between successive wetting events. Figure 4.4

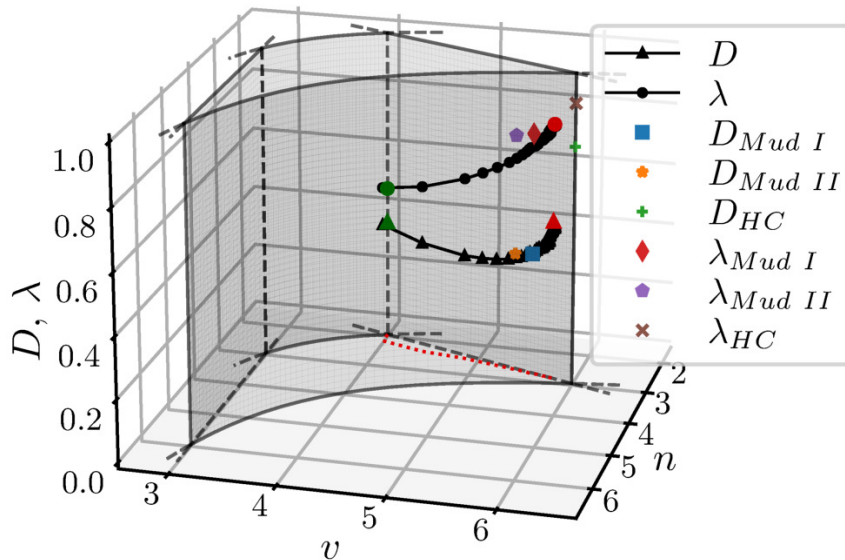


Fig. 4.4 The trajectory of crack evolution under repeated wetting and drying cycles is shown in the (n, v, D, λ) domain. The green and red points represent the starting and ending positions of the crack mosaic's combinatorial trajectory, respectively. The positions of static crack mosaics for (i) Mud crack I, (ii) Mud crack II, and (iii) Honeycomb within the 4-tuple vector domain are also marked, as described in the legend.

shows the time evolution of the topology and geometry measures for the simulation. The (n, v) values rapidly increase from $(2, 4)$ to $(3, 6)$ within the first few time-steps and then remain nearly constant over time. The geometric measure D initially decreases sharply, then increases, stabilizing according to a power-law function. The trajectory represents the transformation of the crack mosaic under repeated wetting-drying cycles from a Gilbert tessellation with $(n, v) = (2, 4)$ towards a Voronoi tessellation with $(n, v) = (3, 6)$ as it matures.

Voronoiness

We have examined the impact of the parameters a , b , and N , which represent the ambient effect, the rate of spring shrinkage (essentially capturing material properties), and the rate of cycles, respectively, on the development of the crack mosaic. The ultimate rate at which any mosaic under repeated wetting-drying cycles will evolve into a Voronoi diagram is an optimization of all three parameters. Figure 4.5 illustrates the influence of these parameters on p and Hausdorff Metric measures of the mosaic. The fact that both the p measure and the Hausdorff Metric (distance between the crack mosaic and the corresponding Centroidal Voronoi mosaic) decrease with t indicates that the crack mosaic moves towards a Centroidal Voronoi pattern with an increasing number of cycles. In the matured mosaic, all nodes are trivalent, and a large proportion of nodes form a 120° triad, as shown in Fig. 4.2(d). Our algorithm geometrically ensures that in such cases, the Voronoi empty circle condition is satisfied, which aligns with our simulations.

Figure 4.5 column I(a–c) shows that p is lower for higher a and lower b values, although the effect of N is not very pronounced. A longer drying period before wetting (higher N) and a lower elastic modulus (lower b), as indicated by Fig. 4.5(b–c), facilitate a faster transition towards a Voronoi pattern.

For a regular hexagon, the value of λ is 0.907. Our simulation results indicate that the value of λ increases from around 0.45 and stabilizes at 0.83, reflecting a transition to a nearly hexagonal shape, as shown in Fig. 4.5 column III(a–c). This is corroborated by Fig. 4.2(c), which displays the matured crack mosaic, where every polygon appears ‘rounder’ than its initial geometry in the matured mosaic. In summary, our simulations suggest that the algorithm tends to converge to a Centroidal Voronoi mosaic, regardless of the initial crack mosaic. Additionally, materials with a lower elastic modulus, when subjected to longer drying periods between consecutive wetting, promote a quicker maturation into a Centroidal Voronoi-like mosaic. The time evolution of both the p measure and the Hausdorff Metric clearly shows that repeated wetting and drying cycles drive desiccation crack mosaics toward a more Centroidal Voronoi-like structure.

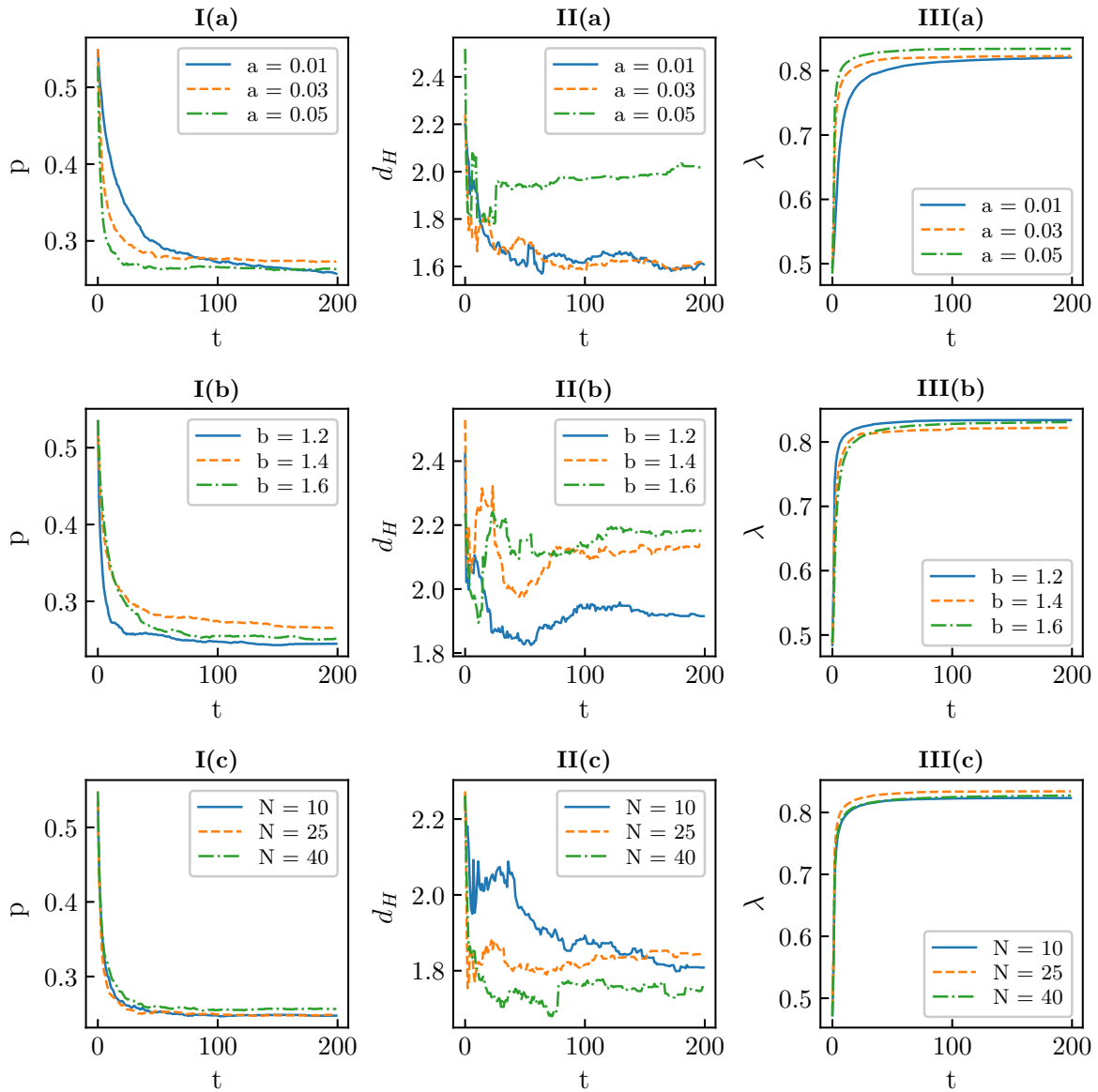


Fig. 4.5 Column I(a–c): The ratio of circles encompassing any seed, p , decreases with successive wetting-drying cycles. Column II(a–c): Variation in the Hausdorff Metric between the mud-crack pattern and the corresponding Voronoi diagram generated using the centroids. The metric decreases with wetting-drying cycles and stabilizes at a constant value of around 1.8. Column III(a–c): The Iso-perimetric ratio λ increases as the mud undergoes wetting-drying cycles, indicating that the peds become rounder with each cycle. In the first row (I(a)–III(a)), only the parameter ‘ a ’ is varied while the other parameters remain constant. In the second and third rows, the parameter ‘ b ’ and the number of desiccation time steps N per cycle are varied, respectively, with other parameters held constant.

Energy

The total energy E of a mud layer with deep vertical cracks can be described as the sum of three components: (i) E_0 , which encompasses all energy contributions except for elastic and fracture energy; (ii) the elastic energy associated with the polygonal crack segments or ‘peds’; and (iii) the fracture energy required to create new crack surface area. In our model, E_0 is assumed to be constant for systems under similar ambient conditions. Therefore, changes in the total mechanical energy during the crack evolution process are attributed solely to the elastic and fracture energy components.

The elastic energy at any given time step is proportional to the change in volume of the polygonal peds. This is calculated as $\gamma \sum_i A_i \delta z$, where A_i represents the cross-sectional area of the i^{th} crack ped, and δz is the vertical depth by which the crack ped opens during the time step. We assume that the mud matrix is homogeneous and isotropic in the plane perpendicular to the direction of evaporation, meaning all polygonal peds open by an equal infinitesimal vertical depth δz in a single time step. The parameter γ reflects the elastic properties of the playa system.

During each wetting-drying cycle, a new crack surface area $L\delta z$ is created, where L denotes the total length of the crack channels in the transverse plane. The fracture energy required to create this new surface is $\sigma L\delta z$, with σ being the fracture energy per unit area. Consequently,

$$E = \gamma \sum_i A_i + \sigma L \quad (4.4)$$

where E denotes the total energy of the system per unit height.

From the simulation, it is observed that while the total area of the polygons remains nearly constant, the total crack length L varies with time. This means that although the overall area stays unchanged, the shape of the polygons evolves through wetting-drying cycles.

Substituting L in terms of λ and using the fact that the total area remains constant in Eq. (4.4), the total mechanical energy per time step in terms of λ is given by (similar to the Sec. 3.3).

$$E = \alpha \lambda^{-\beta} \quad (4.5)$$

where α and β are constants. The net system energy change relative to the crack geometry parameter λ is depicted in Fig. 4.6(a). The system energy follows a power-law relationship with λ , with an exponent of $\beta = 1.13$. It is evident that the energy decreases over time and stabilizes at a constant value as the crack pattern matures and approaches a Voronoi structure.

Figure 4.6(b) shows the stress distribution in each ped of the mosaic after undergoing several wetting-drying cycles, continuing until the crack mosaic reaches maturation. The stress

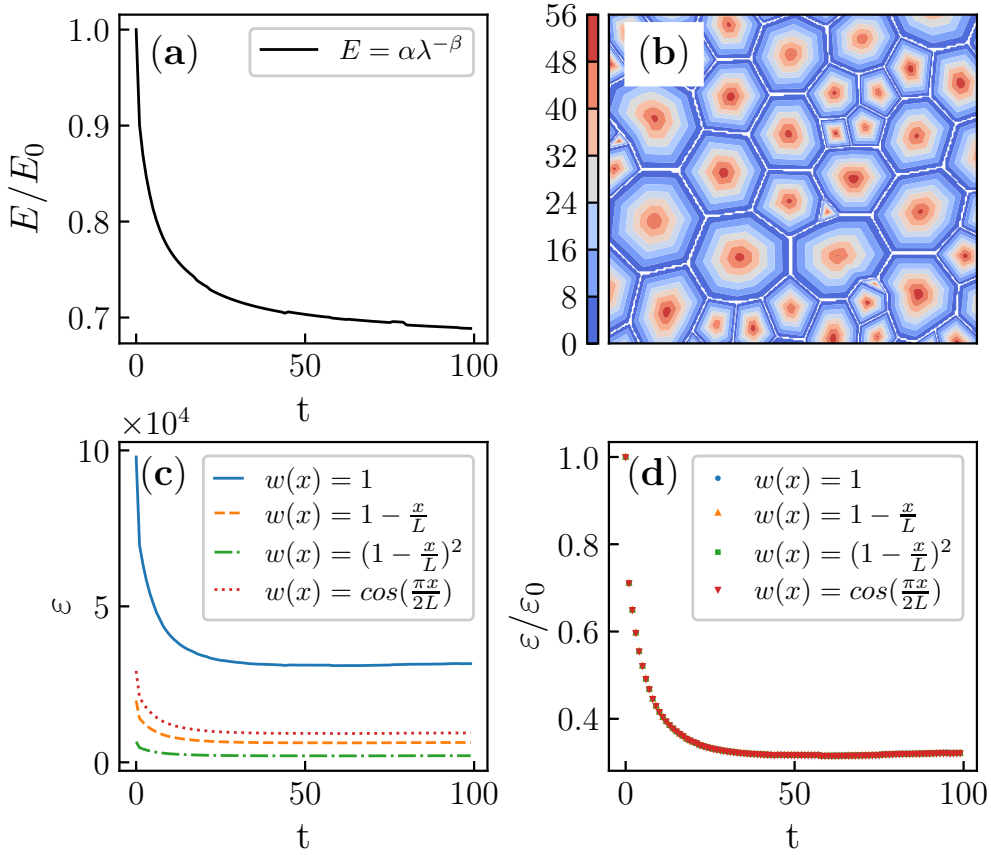


Fig. 4.6 (a) Reduction of elastic energy over successive wetting-drying cycles. (b) Distribution of linear stress within each polygon of the final mosaics. (c) Geometrical energy corresponding to various stress distributions within a polygon. (d) Normalized geometrical energies for different stress distributions converge onto a single curve.

distribution follows an approximately linear pattern centered around the ped centroid, aligning with the crack boundary geometry.

Geometrical Energy

The geometrical energy is defined as (see Sec. 3.3.1)

$$\varepsilon = \sum_i \varepsilon_i = \sum_i \int_{x \in \Omega_i} w(x) \|x_i - x\|^2 dx \quad (4.6)$$

If ε_i is interpreted as the strain energy of the i^{th} polygon, then the stress density function $w(x)$ is obtained from a linear stress distribution inside the polygon such that the stress is maximum at the w -weighted centroid of the polygon (which is almost identical to the geometric centroid

with a deviation $< 0.01\%$) and zero at the boundaries. A polygon in the mosaic shrinks as a result of the strain developed due to the moisture gradient in a ped as drying commences from the edge towards the center. This implies that stress due to shrinkage is zero at the crack front and highest at the centroid. Hence, a linear stress distribution in a crack ped is a simple approximation that mimics the stress distribution in the ped. It is assumed that stress due to evaporation from the exposed top layer is a constant for the whole mosaic. The geometrical energy function of the tessellation is then defined as the summation of this function for all polygons in the tessellation.

If the polygons in the mosaic contain inhomogeneities such as micro-cracks or defects, $w(x)$ can become a non-linear function of x . We considered two non-linear functions for $w(x)$: (i) $w(x) = (1 - \frac{x}{L})^2$ and (ii) $w(x) = \cos(\frac{\pi x}{2L})$. In both cases, the system energy decreases as time t increases, as shown in Fig. 4.6(c). It was observed that the geometrical energy in each stress distribution scenario tends to a minimum value, following a similar pattern. Although the energy decreases in a similar manner with a constant $w(x)$, it stabilizes at a higher equilibrium minimum value. However, when the geometrical energy ε of the mosaic at any time-step t is normalized by its total energy ε_0 at maturation, all the graphs in Fig. 4.6(c) converge into a single curve, as illustrated in Fig. 4.6(d). This indicates that the convergence of the normalized geometrical energy of the mosaic to an identical equilibrium minimum is universal, regardless of the nature of inhomogeneity in the sample. This strongly suggests that the Voronoi diagram represents the equilibrium geometry favored by dynamically evolving systems.

Shannon Entropy, Lewis' and Aboav's Laws

Various methods have been introduced over the past few decades to measure the randomness of 2-D tessellations. The degree of regularity in the Voronoi tessellation is characterized by either the Voronoi entropy or the Shannon entropy, defined as

$$S = - \sum_v P_v \ln P_v \quad (4.7)$$

Here, the symbol P_v denotes the proportion of polygons that have v sides or edges, as referenced in [87, 88, 51]. The calculation outlined in Eq. (4.7) sums up values starting from $v = 3$ to the maximum edge count among the polygons found in the mosaic; thus, if the tessellation's largest polygon is a hexagon, then the summation's upper boundary, v , would be 6. A perfectly ordered structure, which comprises solely one type of polygon making $P_v = 1$, results in the Voronoi entropy being null. With a 2-D random array of seed points stemming from a uniform distribution, S has a value of 1.71 [89]. In a self-organizing system, the expectation is that the

value of S would reduce. Despite this, given that the S value does not depend on the number of seeds, Voronoi entropy signifies an inherent characteristic [90].

Lewis' Law pertains to the randomness found in a polygonal arrangement and suggests that there is a direct correlation between the average area of a standard polygon with v sides, denoted as A_v , and the value of v given by

$$A_v = \alpha(v - 2) \quad (4.8)$$

where α represents a constant of proportionality [91]. This relationship has been shown to hold true for natural patterns across various size scales [92, 93]. The Aboav law [94–96] establishes a connection between the average number of sides m_v of a Voronoi cell that adjoins a v -sided cell and the number v , according to

$$m_v = a + \frac{b}{v} \quad (4.9)$$

where a and b represent constants. Therefore, small polygons are inclined to be encircled by larger ones, and vice versa.

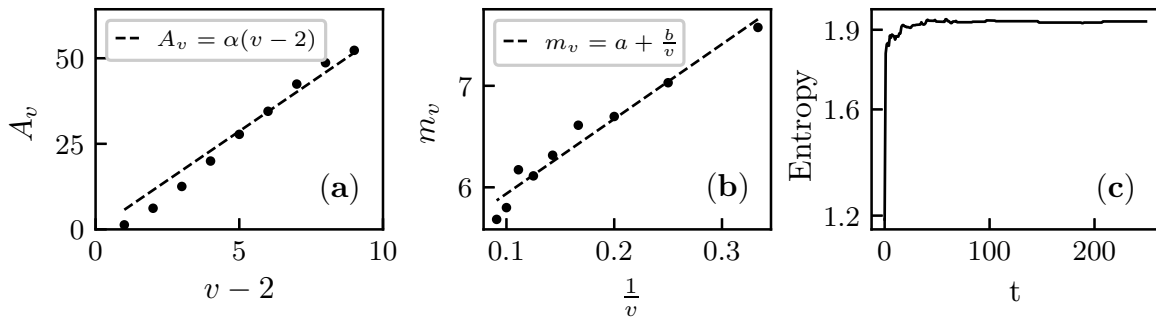


Fig. 4.7 (a) Change in Shannon (Voronoi) entropy over time t for a maturing crack mosaic. (b) Confirmation of Lewis' Law: the relationship between the average area A_v of a polygon with v sides and $(v - 2)$. (c) Confirmation of Aboav's Law: the variation in the average number of sides m_v of polygons adjacent to a v -sided polygon.

The Shannon entropy of the maturing crack mosaic was calculated at each time step t using Eq. (4.7). The equilibrium value reached 1.95 in our wetting-drying simulations, compared to the reported 1.71 for Voronoi tessellation, as shown in Fig. 4.7(a). The Lewis law, as expressed in Eq. (4.8), was confirmed for the mature crack mosaic, as depicted in Fig. 4.7(b). The average area A_v of a polygon with v sides exhibits an approximately linear relationship with $(v - 2)$, with a slope of $\alpha = 3.057$. The scaling of the average number of sides m_v of polygons adjacent to a v -sided polygon in the mature crack mosaic follows a linear trend, as predicted by Aboav's

law in Eq. (4.9). In our simulation, the constants a and b were found to be 5.295 and 6.967, respectively.

4.4.2 Static Crack Mosaics

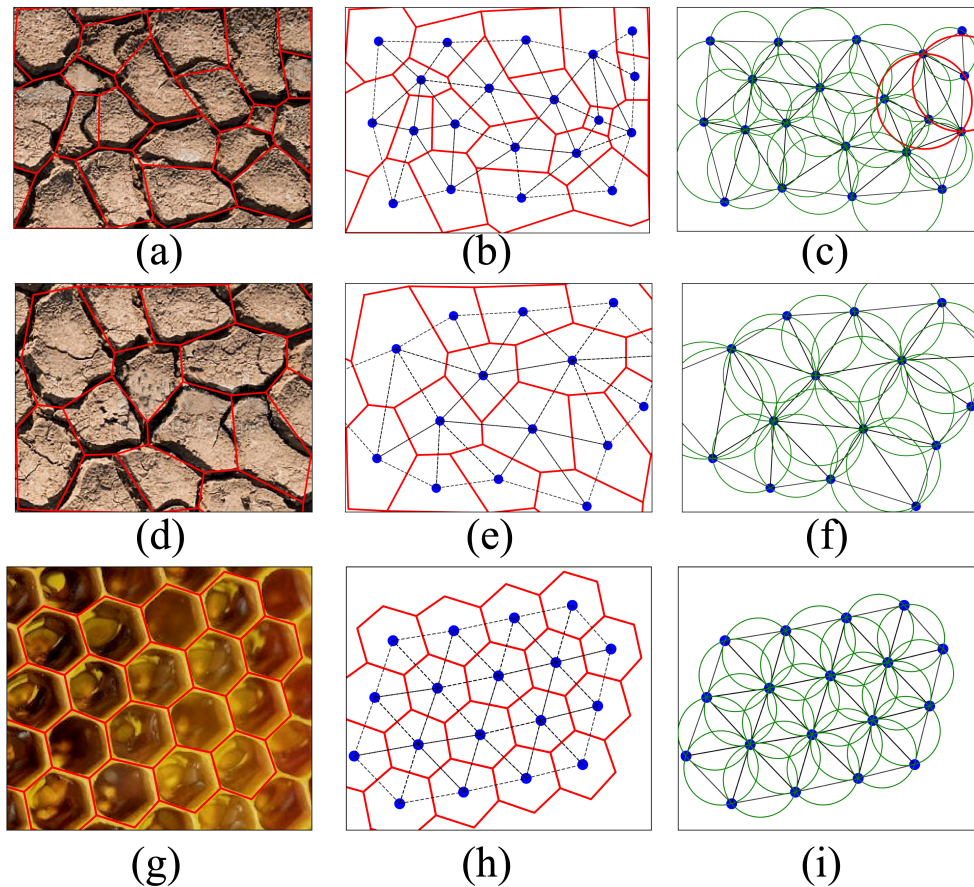


Fig. 4.8 Verification of Voronoi-like patterns. Real mud-cracks: (a) Case I, with the crack network outlined in red. (b) Triangulation created by connecting centroids of adjacent polygons sharing a common edge. (c) Circumcircles drawn for each triangle, with red circles containing one or more centroids. (d) Case II of mud cracks. (e) Delaunay triangulation for the polygons. (f) Circumcircles for all triangles, showing no centroids inside the circles in this case. (g)–(i) illustrate the same schematic process for a honeycomb structure.

To determine whether nature favors Voronoi patterns in crack mosaics, we examine several static examples. Figures 4.8(a) and (d) display images of actual mud crack mosaics, while Fig. 4.8(g) depicts the pattern on a honeycomb surface. The red lines outline the polygonal crack networks. The crack plane is triangulated by connecting the centroids of adjacent polygons that share a common vertex, as shown in Figs. 4.8(b), (e), and (h). Circumcircles for each triangle

Table 4.1 Measures of Voronoi-ness and (n, v, D, λ) values for the static crack mosaics.

Model	p	d_H (pixels)	n	v	D	λ
Mud crack I	0.077	21	2.87	5.42	0.387	0.774
Mud crack II	0.00	14	2.95	5.60	0.399	0.791
Honeycomb	0.00	0	3.00	6.00	0.765	0.904

are drawn in Figs. 4.8(c), (f), and (i), with green circles indicating those that meet the Delaunay triangulation criteria. Triangles that do not conform to Delaunay triangulation are marked with red circles. Comparing Figs. 4.8(c) and (f) reveal that while both originate from mud crack mosaics, the former includes non-Delaunay triangles (indicated by red circles), whereas the latter forms a complete Delaunay triangulation (all green circles). Similarly, the honeycomb structure in Fig. 4.8(g) also results in a Delaunay triangulation.

The p values for all three crack mosaics are presented in Tab. 4.1. The non-zero p value in Fig. 4.8(a) indicates that the mud crack does not form a Centroidal Voronoi diagram. Conversely, the $p = 0$ values for Figs. 4.8(d) and (g) suggest that while the crack pattern aligns with a Delaunay triangulation, the corresponding dual Voronoi diagram may not match the original crack pattern. Therefore, p serves as a simple, heuristic measure that is easy to calculate and provides a quick but incomplete assessment of Centroidal Voronoi characteristics.

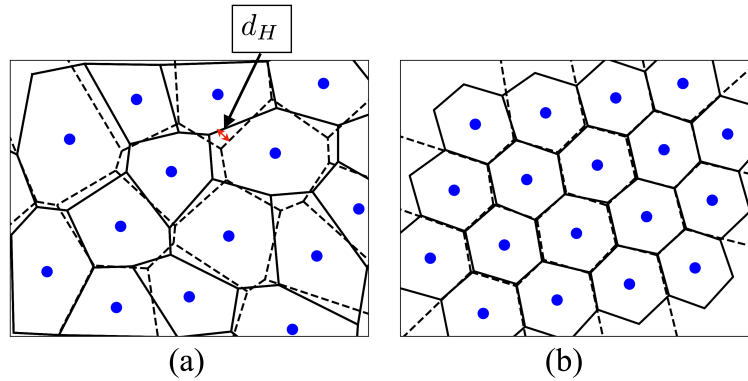


Fig. 4.9 Measuring the Hausdorff Metric, d_H . (a) A real mud crack (solid black lines) is compared with the Voronoi diagram (dashed black lines) generated from the centroids of the polygons. The red arrow indicates the point of maximum deviation, which determines the Hausdorff Metric. (b) The Voronoi diagram aligns perfectly with the honeycomb structure, resulting in a Hausdorff Metric of zero.

To demonstrate the calculation of the Hausdorff Metric, Fig. 4.9(a) shows the real mud crack from Case II (solid black lines) and the corresponding Voronoi diagram (dashed black

lines) created using the polygon centroids as seeds. The red arrow indicates the point of maximum deviation between the real crack pattern and its Voronoi counterpart. This distance represents the Hausdorff Metric between the original crack network and the Voronoi diagram, which becomes zero if the two sets are identical. In the honeycomb case shown in Fig. 4.9(b), the real crack mosaic and its Voronoi diagram overlap perfectly, resulting in a Hausdorff Metric of zero. As shown in Tab. 4.1, the Hausdorff Metric is zero only for the honeycomb structure. This is expected, as the honeycomb in Fig. 4.8(d) is a regular hexagon, where each seed coincides with its centroid. For mud cracks, the Hausdorff Metric is non-zero, although it decreases as the mosaic becomes more Centroidal Voronoi-like.

In conclusion, the p measure can confirm that a crack network is not Centroidal Voronoi if $p \neq 0$. The Hausdorff Metric between a polygonal crack network and its corresponding Voronoi diagram (using the centroids of the original network as seeds) is zero only if the crack network is a Centroidal Voronoi diagram. Lastly, while not all natural crack mosaics are Centroidal Voronoi, systems tend to evolve towards a Voronoi diagram to minimize energy.

Table 4.1 presents the (n, v, D, λ) tuple values for each static crack mosaic, and their positions within the topology-geometry domain are illustrated in Fig. 4.4. While the honeycomb mosaic closely resembles a Centroidal Voronoi, both mud crack systems exhibit Voronoi-like characteristics.

4.5 Conclusions

This study examines the dynamic evolution of crack patterns in colloidal systems, specifically the cyclic wetting and drying of mud cracks, which alters mosaic geometries over time. Colloidal systems in their slurry state are soft, with long response times that allow observation of evolving mosaics. Using a spring model, we simulated the cyclic changes observed in experimental mud systems, finding that crack mosaics transition from ‘T’ to ‘Y’ junctions over time. These changes in topology and geometry were tracked as a trajectory in the (n, v, D, λ) domain.

We provide a phenomenological explanation for the energy shifts during periodic wetting and drying, showing that system energy follows a power-law dependence on λ with an exponent of 1.13. The study confirms that the system naturally tends towards Voronoi-like tessellations, minimizing total energy, as supported by both experimental evidence and mathematical analysis of geometric energy.

The natural tendency of Voronoi diagrams, where each region is closest to its seed, plays a crucial role in the evolution of crack mosaics. To quantify this progression towards Voronoi tessellations, we introduce a measure of ‘Voronoi-ness’ using the p measure and the Hausdorff

Metric, analyzing how crack mosaics evolve during drying-wetting cycles. Our results suggest that mud cracks gradually mature into Centroidal Voronoi tessellations with repeated cycles, with faster progression in systems with lower elastic modulus and longer drying intervals between cycles.

To extend this analysis, we investigated static crack mosaics from real-world examples, assessing their preference for Voronoi patterns. We quantified their degree of ‘Voronoi-ness’ using the p measure and Hausdorff Metric, comparing original crack networks with their corresponding Voronoi diagrams. The polygon centroids were treated as Voronoi seeds, and the Hausdorff Metric measured the alignment between the polygon centroids and system dynamics.

This study provides new insights into the formation and evolution of complex patterns in cyclic systems. It is among the first theoretical and simulation-based investigations of this process. The quantification of ‘Voronoi-ness’ offers a valuable tool for modeling tessellations in both natural and artificial systems. Our findings deepen the understanding of energy minimization in such systems, reinforcing the well-established theory of Centroidal Voronoi tessellations and their connection to physical tessellations, which often exhibit similar geometric properties.

Chapter 5

Simulation of Salt Playas

5.1 Introduction

Salt playas, or salt deserts, are often adorned with intricate patterns of salt ridges that tessellate the entire saline surface into polygons, predominantly pentagons and hexagons. These saline pans are flat, shallow depressions covered in salt layers, typically dry except during periods of flooding or heavy rainfall, which temporarily convert the pans into lakes [97]. Over time, these pans undergo cyclical wetting and drying [98]. Annually, the salt ridges grow up to a few centimeters on the surface, spanning areas from 1 km² to several thousand km², and overlay thin-bedded, salt-saturated clays enriched with various minerals, which can be silty, sandy, or more granular, as noted in geological studies [99–101]. Additionally, most playas have a significant or unique groundwater supply. These salt playas contribute to ecological diversity, benefiting water-bird habitats, providing economic value, and impacting human health [102].

Various theories have been proposed to explain the distinctive Voronoi-like patterns, often using fracture or buckling models [103]. These models suggest that surface fractures tend to form 120° angles as they propagate from weak points. However, not all natural fractures exhibit Y-shaped junctions characteristic of crack mosaics [104]. The shape of cracks can vary, influenced by material properties and environmental conditions [24]. Rigid salt crusts can deteriorate due to extreme weather events like heavy rainfall or flooding [104], with their growth being driven by the interplay between subsurface flow and evaporation rates. Other research includes 2D modeling of complex fluid dynamics beneath playa surfaces [105–110]. Recently, Lasser et al. [75] introduced a 3D model that explores subsurface saline water flow but is less explicit regarding salt crystal formation and deposition. The novelty of this work lies in offering a comprehensive explanation for the natural evolution of the rough pentagonal or hexagonal Voronoi-like tessellation, spanning several square kilometers of salt basins, through a self-organizing process driven by salt ridge formation.



Fig. 5.1 Polygonal pattern formed by salt ridges at Salar de Uyuni, Bolivia. Photo credit: Anouchka Unel [111]

In this chapter, I will explain the intriguing *formation* of polygonal salt patterns by integrating principles from fracture mechanics, fluid dynamics, mass transport, and crystallization. Observations of modern salt playas show predominantly hexagonal polygons, with some pentagonal, rectangular, and triangular cells emerging near the termination zones of salt basins or in areas with significant inhomogeneities [103]. I introduce a model that simulates the development of the ridge mosaic within a 3-dimensional system of porous material, composed of mineral-rich clay, lying above the groundwater table. The model dynamics begin from a time when the salt basin or playa existed without polygonal ridges, then progresses rapidly through time, accounting for the periodic processes that lead to the current macro pattern of salt ridges.

In the subsequent sections, I will provide a detailed description of the model, beginning with crack formation under wetting and drying cycles, followed by the hydrodynamic equations governing fluid flow within the crack conduits that connect groundwater to the surface, the crystallization process, and finally, the stable formation of salt ridges. This will be followed by a discussion of the simulation results and final conclusions.

5.2 Materials and Methods

Salt playas are often low-lying regions that were once lakes or seas, undergoing cycles of wetting and drying. During dry periods, water evaporates from the upper surface layers. As

desiccation occurs, these surface layers contract due to capillary pressure within the pore spaces, eventually leading to the formation of fractures that release the accumulated stress. Since all crack faces are planes of zero traction, a crack ceases to propagate once it intersects another crack, resulting in a tessellation of the surface into polygonal crack patterns, akin to Gilbert tessellation[80]. As drying progresses, desiccation stress moves downward through successive layers, causing the surface cracks to widen and the deeper layers to fracture. The cracks that extend from the surface to the subsurface water table serve as the main channels for water flow. The underlying porous clay system functions as secondary conduits, though these connected channels tend to be highly tortuous and irregular in geometry. A schematic representation is provided in Fig. 5.2(a).

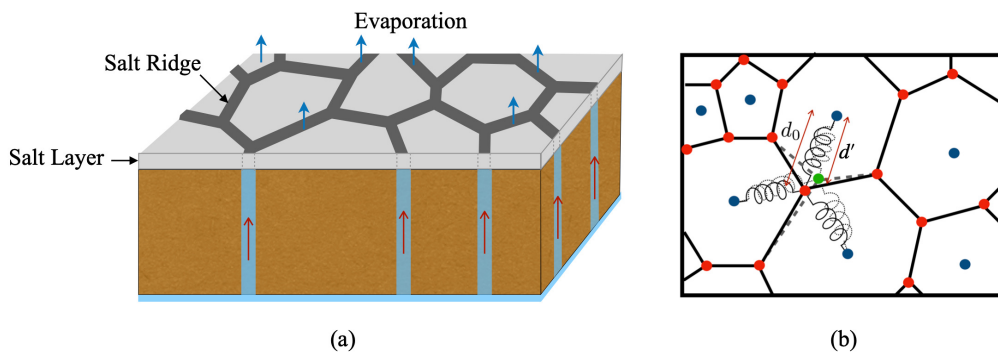


Fig. 5.2 (a) Schematic illustration of a salt playa. The grey layer depicts a salt layer atop the clay surface. Polygonal salt ridges form along the edges of the polygonal cracks as saline water is transported from the subsurface water table through vertical crack channels. Red arrows indicate the direction of advection, while blue arrows represent the direction of evaporation flux. (b) Spring model for crack dynamics. Red dots signify the vertices of peds, and blue circles mark their centroids. The natural length d_0 of the springs connecting a centroid to a vertex is indicated by an arrow. A vertex (red) is connected via springs to the centroids of adjacent polygons to account for elastic forces. The updated position (green) of the vertex after one complete wetting-drying cycle is shown. Dotted springs have updated lengths d' , as indicated by arrows.

During desiccation, water evaporates from the surface layer, and saline water from the subsurface water table (or trapped within the clay's interstitial pores) is drawn upward due to advection driven by the evaporation flux. As water evaporates, it leaves behind the dissolved salt, increasing the salt concentration in the upper layer of the channels. This can create a concentration gradient within the conduits, where the salt concentration at the water table is assumed to be at a fixed lower value corresponding to equilibrium salinity. This initiates a diffusion process from the top layer to the bottom of the channel. A schematic illustrating these processes is shown in Fig. 5.2(a). Variations in salt concentration can influence the local density at each corresponding layer. The mass transport of salt is governed by the combined effects of

advection and diffusion, characterized by the Peclet number $Pe = UL/D$, where U represents the advection velocity, L is a characteristic length scale, and D is the diffusion coefficient of the solution. The characteristic length is considered to be the average crack width of the system. When the competition between advection and diffusion causes the upper layers of the crack channels to become supersaturated, salt crystallization is promoted along the crack edges.

Let the equilibrium salinity at the water table be c_0 , and the critical salt concentration at supersaturation be c_{cr} ; then the difference in salt concentration $\Delta c = c_{cr} - c_0$ dictates the rate of salt crystallization along the surface crack edges under a given ambient condition. Salt crystals continue to accumulate along the crack edges, forming ridges that self-organize into stable structures determined by the angle of repose of the salt deposits. The pattern of the ridges mirrors the crack network pattern on the clay surface. Over an extended period, as the clay surface undergoes multiple wetting-drying cycles, the crack network pattern evolves to achieve a minimum energy configuration. The angles at the junctions where two or more cracks meet shift from 90° to 120° [22]. Consequently, the crack pattern, and therefore the salt ridge pattern, becomes Voronoi-like [112]. The shifting salt ridges are considered a transient state that stabilizes to a steady state once the crack mosaic matures. Thus, during the transient state, evaporation and subsequent crystallization result in the deposition of a surface salt layer; the salt ridges become visibly prominent only after the underlying crack mosaic reaches a mature steady state.

A Voronoi diagram is a collection of regions that tessellates a plane around a set of points (seeds) such that every point within a region is closest to its corresponding seed. Given a finite set of points $x_i (i = 1 \dots n)$ on a subset Ω of the plane, the Voronoi regions are defined as $\Omega_i = \{x \in \Omega : \|x - x_i\| \leq \|x - x_j\| \text{ for all } j \neq i\}$. If the centroids of the polygons coincide with the seeds, the Voronoi diagram is referred to as a Centroidal Voronoi diagram. Many Voronoi-like patterns occur in nature and are often associated with optimizing material or energy [37, 38, 61, 112]. The images of salt ridges tessellating salt playas visually resemble Voronoi mosaics, as seen in Fig. 5.4(d). The Voronoi-ness of a real mosaic can be quantified by comparing it with the Voronoi diagram generated using the centroids of the polygons as seeds [112]. The Hausdorff metric¹ is employed to measure the deviation of the simulated salt ridge patterns from the corresponding Voronoi diagram generated from the centroids.

¹For compact subsets $A, B \subset \mathbb{R}^2$, the Hausdorff Metric $d_H(A, B)$ is defined as $d_H(A, B) = \max\{\max_{a \in A} d(a, B), \max_{b \in B} d(b, A)\}$, where $d(x, C) = \inf\{\|x - c\| : c \in C\}$.

5.2.1 The Simulation Model

Initial Cracks

As water evaporates from clay or soil surfaces during desiccation, stress builds up in the matrix (clay/soil) due to capillary pressure within the pores [24]. Desiccation leads to the fracturing of the surface clay layers, which relieves the accumulated traction. Consequently, all crack faces become regions of zero traction. In our simulation, the initial crack network on the clay surface is modeled using Gilbert tessellation [80, 31]. The cracks initiate from a set of randomly distributed points on a plane, following a homogeneous Poisson point distribution, and propagate along a straight line until they intersect with an existing crack. Periodic boundary conditions are not assumed. The random points represent surface inhomogeneities that act as crack seeds. As desiccation progresses, the lower clay layers experience stress due to the evaporation of water from the interstitial pores, causing the cracks to extend vertically downward with each drying step [112]. These vertically extended cracks eventually serve as conduits that connect to the subsurface water table.

Wetting-drying

A spring network, commonly utilized to simulate fracture mechanics [81, 13, 82–84], has been employed to model desiccation resulting from cyclic wetting-drying. After the Gilbert tessellation is generated, all polygons and nodes are identified. Hookean springs are used to connect each node to the centroids of all polygons that share that particular node. All springs are assumed to have a spring constant k , with a natural length d_0 , which is equal to the distance between the node and the centroid of the polygon to which the spring is attached. During desiccation, the length of each spring contracts, while during wetting, the length expands following the rule –

$$d_n = d_{n-1} \left(1 \mp \frac{a}{b^n} \right) \quad (5.1)$$

Here, a and b are constants, with the negative sign representing drying and the positive sign representing wetting. It is assumed that while the drying process causes the clay layers to shrink, wetting allows the layers to relax slightly as water fills the interstitial pore spaces, leading to some swelling of the clay. At the end of the n^{th} desiccation step, the spring length contracts to $\left(1 - \frac{a}{b^n} \right)$ of its previous length. Similarly, during wetting, the length increases by a factor of $\left(1 + \frac{a}{b^n} \right)$. One complete wetting-drying cycle consists of N consecutive drying steps followed by a wetting step, as shown in Fig. 5.2(b). The wetting-drying rule described by Eq. (5.1) is based on experiments on clay evaporation rates under ambient conditions, where

complete drying corresponds to approximately 63% weight loss [85]. The parameters a and b represent ambient conditions and clay characteristics, respectively. During the drying and wetting processes, the position of a node connected to the centroids of its neighboring polygons by springs is adjusted according to –

$$\Delta \mathbf{x} = \sum_i \Delta \mathbf{d}_i \quad (5.2)$$

The index i denotes the i^{th} spring connected to the node, and $\Delta \mathbf{d}_i$ represents the change in its length. Here, $\Delta \mathbf{d}_i = (d_0 - d') \hat{\mathbf{d}}_i$, where d' is the spring length after N consecutive drying steps or one wetting step, and $\hat{\mathbf{d}}_i$ is the unit vector pointing from the node towards the centroid of its i^{th} neighboring polygon. The crack segments adjust according to the movements of the nodes, and the shape of the crack network evolves through the wetting-drying cycles.

Fluid Dynamics and Crystallization

During desiccation, water evaporates from the top surface of the salt layer, creating a suction pressure that draws water from the subsurface water table to replace the evaporated water. A no-flux boundary condition is assumed for the crack and channel walls. The desiccation effect is represented by a pressure P , which regulates the water flow through the channels. In subsurface water, particularly in salt playa regions, the salinity is high. As water evaporates from the channels, dissolved salt is deposited on the top layers of the channels, increasing their salinity. This leads to the formation of a salt concentration gradient from the upper to the lower layers of the channel, initiating a diffusion flow in that direction. The salinity profile of the channels is controlled by the Peclet number Pe , which is the ratio of advective to diffusive flows.

The fracture channel is divided into cubic grids with a grid size of $dx = dy = dz = 0.1$ cm. The hydrodynamic equations are solved on this grid using the finite difference method. The crack channel in the model has a width of 0.6 cm and a vertical depth of 5 cm. Time is measured in terms of the simulation time step Δt , where $\Delta t \sim 10^{-3}$ s. The evaporation flux induces a suction pressure P in the pore channels. This evaporation flux is represented by the average vertical component U of the water velocity on the top exposed surface of any channel due to the pressure P . No slip boundary conditions are applied at the rock-pore interfaces through the use of imaginary grids [113, 114]. For an incompressible, slow-moving saline solution, the inertial term in the Navier-Stokes (NS) equation can be neglected. The hydrodynamic equations, which are solved iteratively and coupled with each other, include the continuity

equation for an incompressible fluid, the Stokes equation, and the advection-diffusion equation.

$$\nabla \cdot \mathbf{v} = 0 \quad (5.3)$$

$$\frac{\partial \mathbf{v}}{\partial t} + \frac{1}{\rho_0} \nabla p - \nu \nabla^2 \mathbf{v} = \frac{\rho \mathbf{g}}{\rho_0} \quad (5.4)$$

$$\frac{\partial c}{\partial t} = D \nabla^2 c - \mathbf{v} \cdot \nabla c \quad (5.5)$$

Equation (5.4) is discretized in an implicit scheme such that

$$\frac{\mathbf{v}^{n+1} - \mathbf{v}^n}{\Delta t} = -\frac{\nabla p^{n+1}}{\rho_0} + \eta \nabla^2 \mathbf{v}^{n+1} + \frac{\rho \mathbf{g}}{\rho_0} \quad (5.6)$$

from which we obtain \mathbf{v}^{n+1} ,

$$\mathbf{v}^{n+1} - \eta \Delta t \nabla^2 \mathbf{v}^{n+1} = \mathbf{v}^n - \frac{\Delta t}{\rho_0} \nabla p^{n+1} + \frac{\rho \mathbf{g}}{\rho_0} \Delta t \quad (5.7)$$

Using the principle of mass conservation for incompressible fluids and the aforementioned equations, the pressure at time step $(n + 1)$ is

$$\nabla^2 p^{n+1} = \frac{\rho_0}{\Delta t} \nabla \cdot \mathbf{v}^n + \frac{\nabla \cdot (\rho \mathbf{g})}{\rho_0} \Delta t \quad (5.8)$$

The pressure gradient ∇p is established with boundary conditions of $p = P$ at the bottom of the channel and $p = 0$ at the top grid cells of the crack channel. Here, \mathbf{v} and p are the velocity and pressure, respectively, calculated at the center of a given grid cell and are assumed to be constant within that cell. The index n denotes the n^{th} time step. For $n = 0$, all other grid cells are assumed to have zero values for \mathbf{v} and p . Water enters the channel perpendicularly from the groundwater source, so the horizontal component of velocity in all grid cells in the bottom layer of the channel is zero.

ρ_0 denotes the density of saline water with the initial salinity concentration c_0 , ν is the kinematic viscosity, and D is the diffusion constant. The density of the solution is influenced by temperature and concentration. Given the high specific heat of water, temperature gradients within the channel are not considered. Instead, the density of water in the buoyancy term $\rho \mathbf{g}$ is assumed to increase linearly with salinity, following the Boussinesq approximation: $\rho = \rho_0 + s \Delta \rho$. Here, s is a linear function of salinity, where $s = 0$ at the initial salinity c_0 and $s = 1$ at the supersaturated salinity c_{cr} . Since the salt concentration is sampled at each time step of the flow, the impact of density on the flow rate is assumed to be conservative. Equations (5.3–5.5) are solved iteratively until the parameters converge to within $\leq 10^{-5}$

between successive iterations, defining the steady state. The discretization details follow the methods outlined in other works by the authors [115, 116], extended to three dimensions.

At the top layer of the channels, if the salinity of the water near the channel wall reaches or exceeds c_{cr} , say $c_{cr} + \delta c$, the excess salt δc crystallizes and deposits on the surface edge of the channel wall. In the simulation, $\delta c = 0.01$ gm/cc. The irregularities in the channel walls serve as nucleation sites for the crystallization process. It is assumed that the latent heat released during crystallization does not affect the water temperature due to the high latent heat of water.

The entire process of crack formation to salt crystallization can be summarized as follows: During the drying season, as surface layers lose water due to desiccation, cracks initiate from weak points, fragmenting the surface into crack ‘peds’. Desiccation traction can alter the orientation of these crack lines. Experimental studies have documented these processes [22, 24, 112]. At the end of each wetting cycle, the crack channels are filled with water at equilibrium salinity c_0 . As evaporation occurs, advection-diffusion flow starts within the channel, increasing salinity in the top layers, leading to supersaturation and eventual crystallization.

In a wet cycle, although the crack spaces fill with water, the cracks do not heal perfectly and remain as weak fronts. During the subsequent dry cycle, cracks typically reappear at these weak fronts, and crack nodes shift to new positions due to the resulting traction. This process continues until the crack mosaic matures.

Over many wetting-drying cycles, the crack mosaics evolve into a stable equilibrium geometry, known as the ‘matured’ state. Salt deposits along the crack edges shift with the changing crack patterns, covering the playas with a layer of salt. When the crack pattern becomes static upon maturation, salt crystals accumulate along the cracked boundaries and form ridges that become visible as polygonal mosaics. In the model, ridges are allowed to form stable structures through self-organization, distributing the deposited crystals to the nearest neighbor sites with lower potential energy (lower height). The self-organization of the crystals occurs while maintaining an angle of repose of 63° . Experimental measurements of table salt (NaCl) from Tata Chemicals Ltd. showed an angle of repose of 58.5° [see Fig. 5.4(c)]. The angle of repose depends on factors such as the chemical composition, grain size, shape, purity, and hygroscopic properties of the salt. To simplify the simulation, our model uses an angle of repose of approximately 63° .

The flowchart of the simulation is outlined as follows:

1. **Surface Crack Formation:** Initiation of cracks on the surface due to desiccation.
2. **Crack Evolution Over Time:** Development and changes in the crack pattern with drying and wetting cycles.

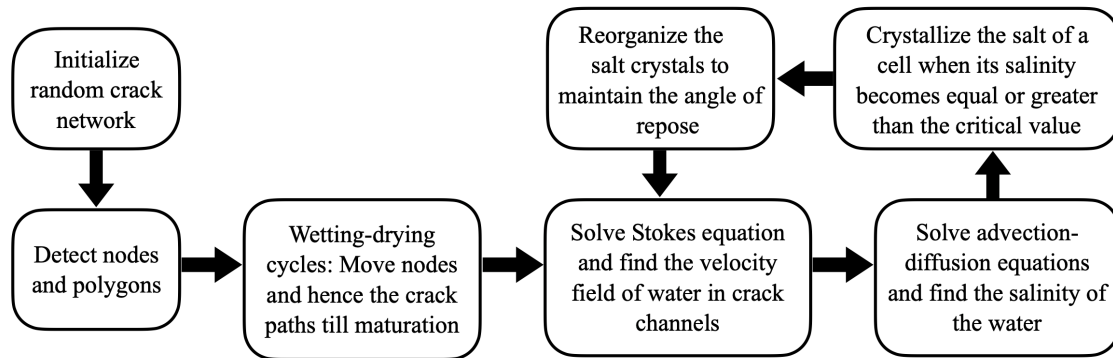


Fig. 5.3 Flowchart of simulation.

3. **Control of Evaporation Flux:** Determination of evaporation flux which generates draw pressure, facilitating the movement of saline water from the subsurface water table to the surface.
4. **Pressure and Velocity Field Determination:** Calculation of pressure and velocity fields within the crack channels.
5. **Salt Concentration Distribution:** Assessment of salt concentration in the channels resulting from the combined effects of advection and diffusion.
6. **Salt Crystallization:** Deposition and crystallization of salt on the channel walls.
7. **Self-Organization of Salt Ridges:** Formation and stabilization of salt ridges through self-organization, resulting in stable structures.

This process is illustrated in Fig. 5.3.

5.3 Results and Discussion

The progression of crack mosaics from a Gilbert tessellation to a mature Voronoi-like polygonal tessellation under periodic wetting-drying cycles is illustrated through time-lapse screenshots of a single polygon with an arbitrary shape in Fig. 5.4(a). The final 3-D simulated polygonal salt ridges tessellating a playa, as produced by our model, is shown in Fig. 5.4 alongside a real image of a playa lake in the Altiplano-Puna Plateau of the Andes, Fig. 5.4(d). The resemblance between the simulated polygonal pattern and the actual ridge mosaics is striking. The lateral striations seen along the ridge walls of the simulated 3-dimensional salt playa [see Fig. 5.4(b)] suggest that the salt deposits self-organize to maintain an angle of repose at 63° . A short video

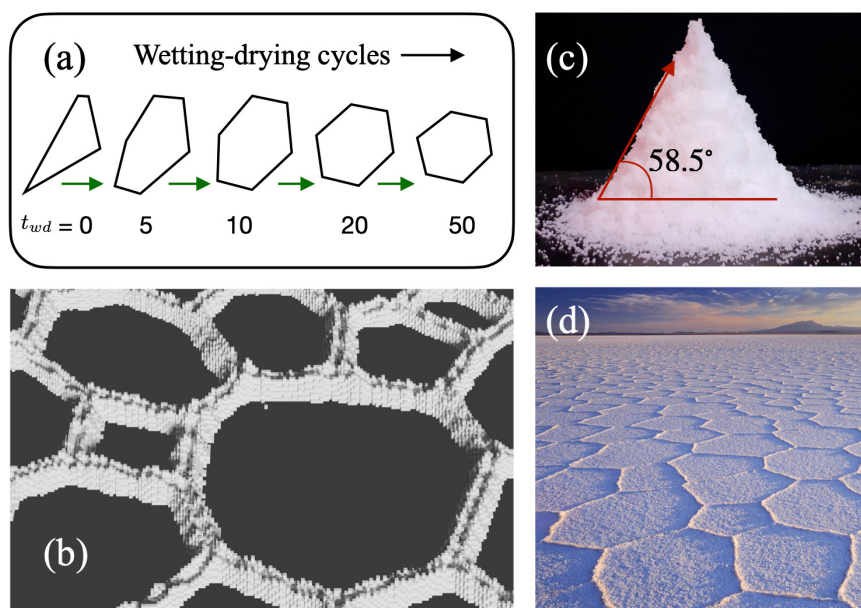


Fig. 5.4 (a) The shape evolution of an arbitrarily shaped polygon under cyclic wetting and drying, following the spring-network model, until it reaches maturation. (b) 3-D simulation of salt ridge patterns. Refer to supplemental video files for more details. (c) Experimental measurement of the angle of repose for a self-organized pile of wet NaCl salt (Tata Chemicals Ltd.), showing an angle of 58.5° . (d) A playa lake located in the Altiplano-Puna Plateau of the Andes. Adapted from Brooks[117].

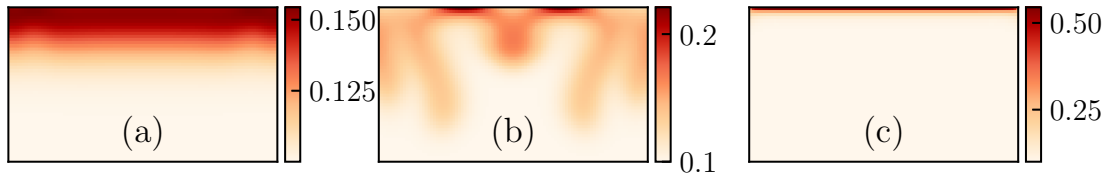


Fig. 5.5 Impact of evaporation-induced suction pressure on the salinity profile along the y - z plane of a typical crack channel after 2500 time-steps. Parameters $D = 0.5 \text{ cm}^2/\text{s}$ and $c_{in} = 0.1 \text{ gm/cc}$ are kept constant. Legends indicate the salinity range. Salinity profiles for (a) $P = 10 \text{ dyn/cm}^2$, $Ra = 18.3$; (b) $P = 15 \text{ dyn/cm}^2$, $Ra = 8.7$; (c) $P = 20 \text{ dyn/cm}^2$, $Ra = 6.1$.

demonstrating the growth and self-organization of salt along crack fronts is provided in Ref. [118].

The rate of salt crystallization along crack edges results from the combined influences of the evaporation flux, which determines suction pressure P , the diffusion coefficient D of the saline solution, the equilibrium salt concentration c_0 in the subsurface water table, and the critical salt concentration c_{cr} at which the solution becomes supersaturated and crystallization begins. For any given salt solution, D remains constant. Initial analysis showed that the concentration difference Δc , rather than c_0 or c_{cr} , is the key factor determining the onset of crystallization t_{cr} . Therefore, our results will be presented and discussed concerning variations in Δc .

Figure 5.5 displays salinity distribution snapshots along a y - z section in a typical pore channel, where the evaporative flux (and thus suction pressure) is varied while keeping the diffusion coefficient D and Δc constant. Figure 5.5(a) shows the profile for a low P -high D combination, where $Pe < 1$. The high D value effectively redistributes salinity concentration within the crack channel, despite the increased salinity at the top layer. When $Pe \sim 1$, as shown in Fig. 5.5(b), the competition between advective flow and gravity leads to the formation of Rayleigh fingers, which penetrate inward from the channel's top surface. At $Pe \gg 1$, the high suction pressure almost entirely suppresses the role of diffusion, as seen in Fig. 5.5(c). The parameter values are indicated in the figure caption, and the color legend beside each figure shows the salinity range.

Steven et al. [110] conducted 3-D resistivity measurements that revealed plumes of more saline water descending due to the interplay between density inversions and convection effects when their ratio is approximately 1. Our flow results in Fig. 5.5 align with Steven et al.'s experimental findings at $Pe \sim 1$. The heterogeneity in hydrogeologic processes can lead to Rayleigh numbers Ra that vary significantly between different salt playas, depending on subsoil and atmospheric conditions [119, 120], influencing the presence of free convection and flow instabilities. In this study, variations in evaporative pressure, density, and diffusion constants were chosen to allow Ra to range from 1 to 130.

Although it is common practice to describe advection-diffusion flow processes using the Peclet number Pe , it is noted that advection and diffusion have distinct impacts on the first crystallization time t_{cr} , which can be obscured when their combined effect is represented solely by Pe . Therefore, I present and discuss the simulation results by examining P and D separately. The evaporation flux is assumed to be vertical to the surface plane and remains unaffected by external factors such as wind velocity, temperature fluctuations, or changes in humidity.

First crystallization time dependence on evaporation flux

In examining the dependence of crystallization on suction pressure P with varying Δc , the diffusion coefficient is kept constant at $D = 0.1 \text{ cm}^2/\text{s}$. Since the simulation accelerates the time evolution of a phenomenon that naturally spans months, the time of first crystallization has been scaled by the characteristic time required for diffusion in advection-diffusion flow. The scaled time $\tau = t/T$ is dimensionless, where $T = D/U^2$ and t is time measured in units of Δt . The characteristic time is calculated using the values $D = 0.1 \text{ cm}^2/\text{s}$, $P = 15 \text{ dyn/cm}^2$, and $U = 4.021 \text{ cm/s}$. A log-log plot of τ_{cr} versus P [see Fig. 5.6(a)] shows a power-law relationship, with the exponent $m_{\Delta c}$ and y-intercept $n_{\Delta c}$ both depending on Δc .

$$\log \tau_{cr} = m_{\Delta c} \log P + n_{\Delta c} \quad (5.9)$$

The first crystallization time τ_{cr} decreases as evaporation rates and, consequently, suction pressure P increase, following a power law. The exponent $m_{\Delta c}$ decreases linearly with Δc , as shown in the inset of Fig. 5.6(a). Additionally, for a given D and P , τ_{cr} increases exponentially with Δc . The variation of the y-intercept $n_{\Delta c}$ with Δc is also depicted in the inset of Fig. 5.6(a). Therefore, we can express it as:

$$m_{\Delta c} = q_1 \Delta c + r_1 \quad (5.10)$$

$$n_{\Delta c} = q_2 \Delta c + r_2 \quad (5.11)$$

where, q_1 , r_1 , q_2 and r_2 are functions of D and hence, constants for a given D . Combining Eqs. (5.9 – 5.11),

$$\log \tau_{cr} = q \Delta c + r \quad (5.12)$$

where

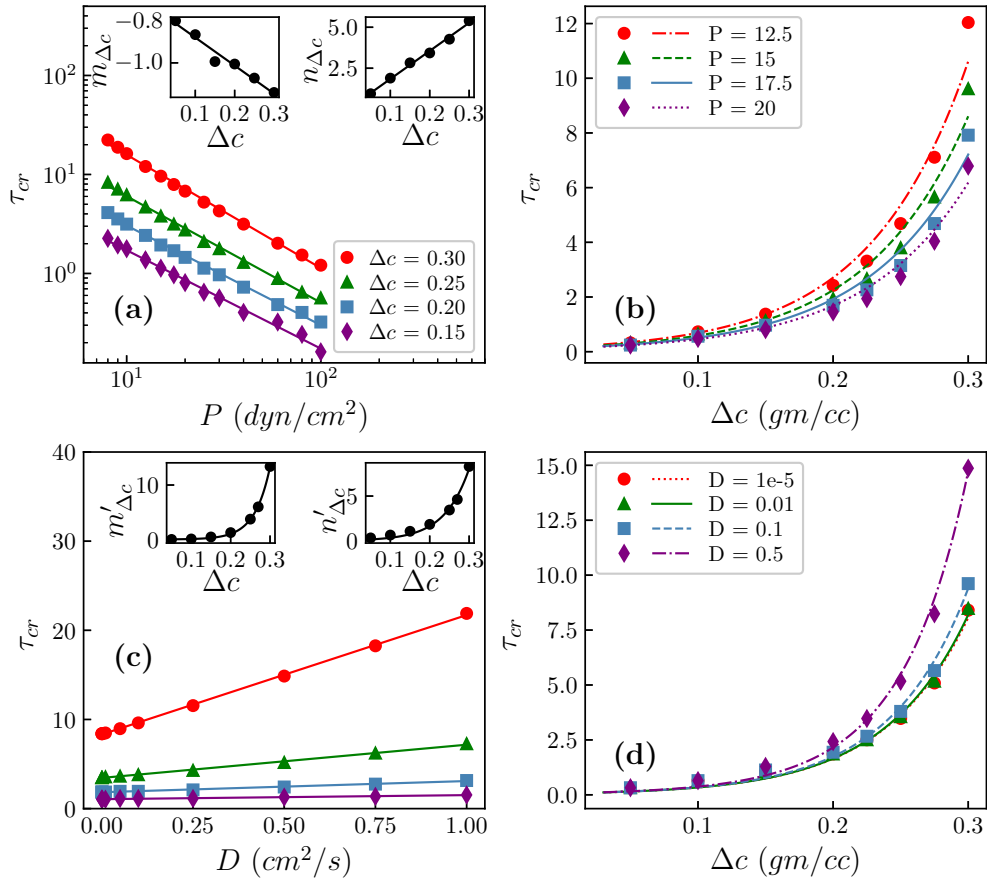


Fig. 5.6 (a) Log-log plot showing the variation of τ_{cr} with P for different Δc values. The insets illustrate how the scale exponent $m_{\Delta c}$ and the y-axis intercept $n_{\Delta c}$ change with Δc . (b) Validation of the analytical relationship between τ_{cr} and Δc for varying P . The symbols indicate simulated data points, while the curves are derived from Eq. (5.12). (c) Plot of τ_{cr} versus D for various Δc values. The insets display the variation of the slope $m'_{\Delta c}$ and the y-axis intercept $n'_{\Delta c}$ with Δc . The color legend is the same as in (a). (d) Validation of the analytical relationship between τ_{cr} and Δc for varying D . The symbols represent simulated data points, and the curves are based on Eq. (5.18).

$$q = q_1 \log p + q_2 \quad (5.13)$$

$$r = r_1 \log p + r_2 \quad (5.14)$$

Equation (5.12) describes the relationship between the time of first crystallization τ_{cr} , suction pressure P , diffusion coefficient D , and concentration difference Δc . Figure 5.6(b) shows simulation results illustrating the variation of τ_{cr} with Δc for different values of P while keeping D constant. The lines in the graph are derived from the analytical expression in Eq. (5.12). The close agreement between the simulation data and the calculated values confirms the self-consistency of the model.

First crystallization time dependence on Diffusion coefficient

Salt playas can contain salts of various chemical compositions depending on their geographical location. While halite ($NaCl$) is the principal salt in salt pans, other salts such as gypsum ($CaSO_4 \cdot 2H_2O$), mirabilite ($Na_2SO_4 \cdot 10H_2O$), thenardite (Na_2SO_4), epsomite ($MgSO_4 \cdot 7H_2O$), trona ($NaHCO_3 \cdot Na_2CO_3 \cdot 2H_2O$), KCl , and carnallite ($KCl \cdot MgCl_2 \cdot 6H_2O$) are also found [121, 122]. The diffusion coefficient for each of these salt solutions varies under identical ambient conditions. Given the generic nature of our model, an analysis was conducted to examine the dependence of salt crystallization time on the diffusion coefficient of the saline solution. We found that τ_{cr} increases linearly with increasing D , although with different slopes, as shown in Fig. 5.6(c).

$$\tau_{cr} = m'_{\Delta c} D + n'_{\Delta c} \quad (5.15)$$

As D increases, the time of first crystallization τ_{cr} increases as anticipated, since higher diffusion rates hinder the attainment of supersaturation at the top layer of the channel for all Δc values. Both $m'_{\Delta c}$ and $n'_{\Delta c}$, which are functions of Δc , increase exponentially with Δc , as shown in the inset of Fig. 5.6(c).

$$m'_{\Delta c} = a_1 e^{b_1 \Delta c} \quad (5.16)$$

$$n'_{\Delta c} = a_2 e^{b_2 \Delta c} \quad (5.17)$$

Here, a_1 , b_1 , a_2 , and b_2 are constants determined by the evaporation flux and are functions of Δc . By combining Eqs. (5.15 – 5.17), we obtain:

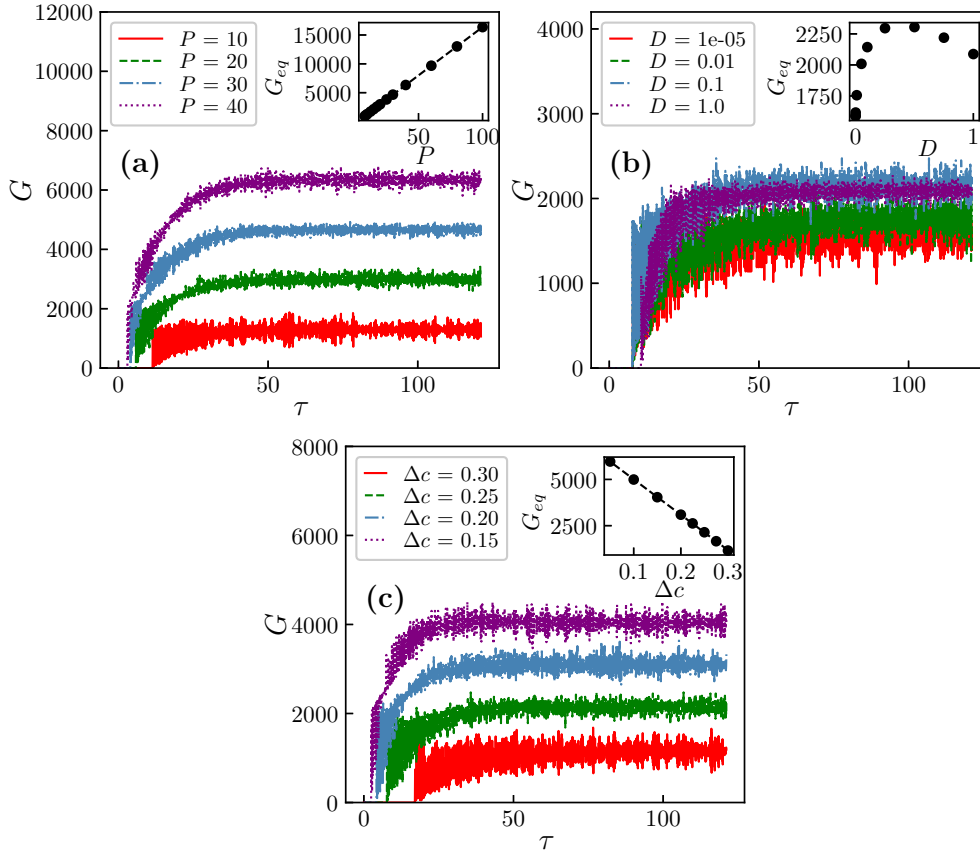


Fig. 5.7 Effect of the model parameters P , D , and Δc on the crystal growth rate G versus dimensionless time τ , following crack maturation. The crystal growth rate G approaches a dynamic equilibrium value G_{eq} in each scenario. The variation of G_{eq} with each parameter is shown in the insets of the figures. (a) Effect of varying pressure P with constants $D = 0.1 \text{ cm}^2/\text{s}$ and $\Delta c = 0.2 \text{ gm/cc}$. (b) Effect of varying diffusion coefficient D with constants $P = 15 \text{ dyn/cm}^2$ and $\Delta c = 0.2 \text{ gm/cc}$. (c) Effect of varying Δc with constants $P = 15 \text{ dyn/cm}^2$ and $D = 0.1 \text{ cm}^2/\text{s}$.

$$\tau_{cr} = a_1 e^{b_1 \Delta c} D + a_2 e^{b_2 \Delta c} \quad (5.18)$$

Equation (5.18) is validated from the simulation results displayed in Fig. 5.6(d) where the exponential curve (denoted by lines) drawn using Eq. (5.18) almost exactly fits the simulation data obtained for τ_{cr} versus Δc for constant values of P . One can conclude that the simulation model produces self-consistent results.

Crystal growth

The impact of each variable— P , D , and Δc —on crystal growth rate G was observed over time on the matured crack mosaic, with other parameters held constant while varying one

parameter at a time. In all cases, the salt growth rate initially increased and then stabilized at a constant plateau once the system reached dynamic equilibrium [see Figs. 5.7(a) – (c)].

The crystal growth rate showed a sharp increase within approximately the first 100 time steps, though the rate of increase varied depending on whether P , D , or Δc was being adjusted. To understand how this dynamic equilibrium is reached, consider that while advection raises salinity at the top layers, it also increases fluid density. This increase in density enhances the downward pull of gravity, which, along with diffusion, counteracts the upward pull of advection. With the right combinations of P , D , and Δc , dynamic equilibrium can be achieved, though at different times for each parameter.

The equilibrium growth rate G_{eq} increases linearly with P [see inset of Fig. 5.7(a)] but decreases linearly with Δc [see Fig. 5.7(c)]. In contrast, as shown in the inset of Fig. 5.7(b), G_{eq} increases with D up to a certain point, after which it decreases with further increases in D . Up to the inflection point, the upward advection force outweighs the effects of diffusion and gravity, thus increasing the growth rate. Beyond this point, however, the system becomes limited by advection, as higher diffusion combined with gravity reduces G_{eq} .

5.3.1 System Energy and Voronoi-ness

The total energy E of a mud playa with deep vertical cracks can be described as the sum of three components: (i) E_0 , which encompasses all energy contributions except for elastic and fracture energy; (ii) the elastic energy associated with the polygonal crack segments or ‘peds’; and (iii) the fracture energy required to create new crack surface area. In our model, E_0 is assumed to be constant for playas under similar ambient conditions. Therefore, changes in the total mechanical energy during the crack evolution process are attributed solely to the elastic and fracture energy components.

As discussed in Sec. 4.4.1, the total energy can be expressed as

$$E = \alpha \lambda^{-\beta} \quad (5.19)$$

where α and β are constants. Figure 5.8(a) shows that the energy decreases with wetting–drying cycles as the patterns become stable.

The Hausdorff metric between the salt ridge pattern and the corresponding Voronoi diagram is recorded at each wetting-drying cycle, as illustrated in Fig. 5.8(b). This metric decreases over time as the ridge pattern increasingly resembles a Voronoi diagram. Previous research by the authors [112] has shown that the progression towards a Voronoi-like mosaic occurs regardless of the initial distribution of crack seeds. Although different initial seed distributions lead to variations in maturation time, the overall evolution follows the same functional pattern.

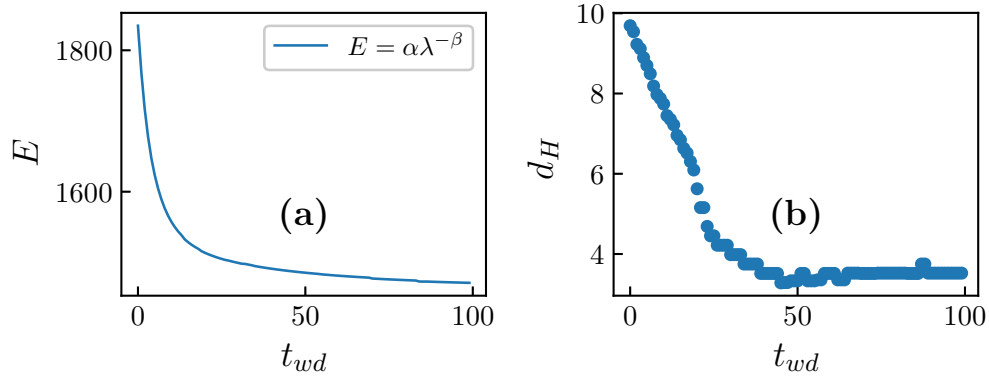


Fig. 5.8 (a) Change in system energy over time. (b) Changes in the Hausdorff metric between the salt ridge pattern and the corresponding Voronoi diagram during wetting-drying cycles.

Therefore, the evolution of salt playas involves a process of minimizing total system energy, resulting in a transition towards a centroidal Voronoi mosaic.

5.4 Conclusions

Salt playas, with their striking hexagonal salt ridge patterns, present a complex challenge for scientific modeling. This study explores their formation through a dynamic simulation using a spring network model to simulate crack formation under periodic wetting-drying cycles. The evolution of the crack mosaic from a random pattern to a nearly hexagonal Voronoi-like structure demonstrates energy minimization, with the Hausdorff metric indicating convergence to Voronoi geometry.

Fluid transport and salinity profiles in crack channels were modeled using the Stokes equation and finite difference methods. The crystallization time τ_{cr} was analyzed as a function of evaporation pressure P , salt diffusion coefficient D , and salinity difference Δc , with results validating the proposed model. The salinity profile showed distinct behaviors depending on the Peclet number Pe , indicating significant growth for $Pe \geq 1$.

Crystallization growth rate G was tracked, showing an initial sharp increase followed by a dynamic equilibrium G_{eq} . While G_{eq} increased linearly with P and decreased with Δc , it showed a peak with D , beyond which the rate decreased due to the interplay of advection, gravity, and diffusion.

Overall, the model effectively replicates the Voronoi-like mosaic seen in real salt playas, highlighting that the non-linear processes involved aim to minimize system energy.

Chapter 6

Stress-Induced Fracture in Porous Systems

6.1 Introduction

The investigation of fracture processes and their relationship to material properties has remained a significant research focus for engineers and scientists since the development of Griffith's theory [1], which established the criteria for materials cracking to form new surfaces as a mechanism to release accumulated tensile or compliant stress. Since then, both experimental and theoretical studies have demonstrated that cracks can initiate as isolated failures that may coalesce, leading to crack avalanches of varying sizes and patterns influenced by the intrinsic material properties and external loading conditions [24, 123]. The fracture behavior of porous systems such as granular solids, rocks, and colloidal systems, which are prevalent in everyday life, is highly dependent on factors such as pressure, grain size and shape distribution, and the micro-geometry of pore spaces [124–126]. These systems exhibit fracture complexity distinct from that of ordered metallic systems [127]. Experimental observations in porous systems suggest that failure begins with the nucleation of micro-cracks, which are accompanied by bursts of acoustic energy [128, 129]. These micro-cracks grow and merge, ultimately leading to the macro-failure of the material [130, 131]. Failure modes can range from axial splitting to shear band formation, reflecting a non-linear transition from brittle to ductile fracture [132, 133]. Large-scale simulations employing lattice models [134–137] and statistical analysis have advanced the understanding of the geometrical and topological characteristics of fractures and scaling behavior [138]. Before complete system failure, avalanches of micro-cracks are observed in various materials, such as wood [139], glass [140], volcanic activity [141], and earthquakes [142] [143, 144]. Quasi-static lattice models like the random fuse model [145, 146] and the spring-network model [147, 84] are often used to simulate fractures, but they face limitations in explicitly capturing deformable contacts, slips, rotations, and discontinuities.

In this study, we investigate fracture statistics and their dependence on material properties in a porous system subjected to axial compression using the Distinct Element Method (DEM) [148, 149]. Spherical grains of various sizes are allowed to fall under gravity, forming a three-dimensional structure, with their radii randomly chosen from a log-normal probability distribution. Compressive loading is then applied to the system in a quasi-static manner.

The compression can be visualized as the effect of a rigid wall in contact with the upper surface, descending with velocity V_w . It is assumed that the grains deform under compressive stress, causing contacts to change from points to planes. The grains are cemented at their contact points, with the cementation material having elastic properties distinct from the grains themselves. We track the effects of loading by calculating the stress and strain accumulation, the number of micro-cracks formed up to the crack avalanche, and the eventual development of one or more system-spanning percolating cracks. This study explores the dynamic cracking process as a function of the elastic modulus and breaking threshold of the cementing material between grains while other factors—such as grain size distribution, elastic properties of the grains, and wall velocity—are held constant. The macroscopic load is borne by the grain and cement skeleton in the form of force chains propagating from one grain to another across contacts. DEM is used to calculate the forces, which may be compressive, tensile, or shear in nature.

Analyzing the *cumulative crack statistics* reveals two distinct cracking regimes: (i) a zone of micro-crack formation, followed by (ii) a zone of micro-crack merging, culminating in system-spanning percolating cracks. Under constant quasi-static loading, the transition from one zone to the other occurs at a critical value of the elastic property of the cementing material. Notably, both this critical transition point and the onset of total percolation exhibit scaling behavior with respect to the elastic property of the cementing material, though with different exponents. Further analysis of individual micro-crack bursts shows that the largest burst follows a power-law distribution relative to the breaking threshold of the cementing material. The scaling behavior of load distribution during cracking for fixed material properties has been reported previously [150]. Additionally, Ferenc et al. [151, 152] have demonstrated that fragment mass follows a scaling behavior with a dimensionless energy measure, which depends on material properties.

In the following sections, I will detail the basic principles of DEM and the methodology for structure generation, followed by sections discussing our results, the associated discussion, and finally, the conclusion of this work.

6.2 Distinct Element Method

The Distinct Element Method (DEM) models granular materials as an assembly of distinct particles, each governed by fundamental principles of physics and mechanics. The particles are represented as spherical rigid bodies with finite mass, capable of moving independently, both translating and rotating. DEM calculations alternate between applying Newton's second law to the particles and updating contact forces via a force-displacement law. Newton's second law governs the translational and rotational motion of each particle, accounting for contact forces, applied forces, and body forces. Meanwhile, the force-displacement law updates the contact forces that arise from particles' relative motion at each point of contact.

The cementing behavior of the material is modeled by assigning parallel bonds with stiffness between particles in contact or close proximity. These bonds transfer both force and moment, and they can break when the tensile or shear stress on the bond exceeds its respective strength.

The assumptions in DEM are:

- Particles can translate and rotate independently.
- Two particles, A and B , are considered to be in contact if the distance d between their centers satisfies $d \leq R_A + R_B$.
- Particles interact solely through contact points, with each contact involving only two particles.
- Particles are allowed to overlap slightly at the contact point, but the overlap is small relative to the particle size.
- Bonds with finite stiffness and breaking thresholds exist at contacts, and these bonds break if their thresholds are exceeded.
- Newton's second law is applied to determine the translational and rotational motion of each particle, and the force-displacement law updates the contact forces based on their relative motion at the contact points.
- The dynamic behavior is modeled by updating the particle positions and bond states at each time step Δt , which is small enough to assume constant velocity and acceleration.
- Δt is chosen such that disturbances caused by a particle do not propagate beyond its nearest neighbors within a single time step.

The DEM treats particle interactions as a dynamic process, where equilibrium states are achieved when the internal forces balance. When an external force is applied to the top surface

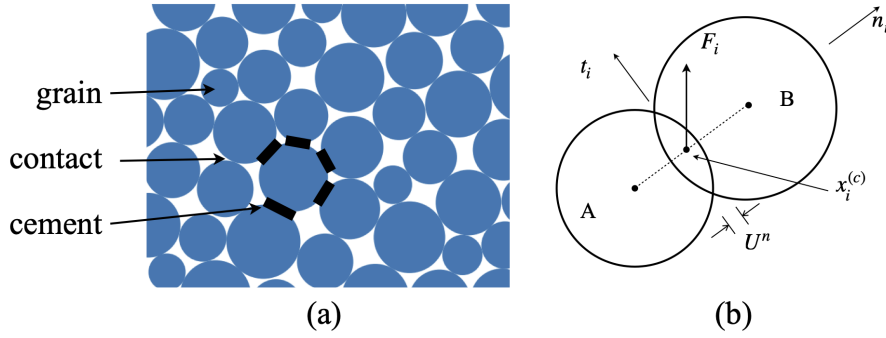


Fig. 6.1 Schematic diagram showing spherical grains constitute a porous system. The grains are cemented at their intersections. (b) Forces acting on particles in DEM.

of the structure, disturbances occur due to relative movements between particles. The speed at which these disturbances propagate depends on the distribution of particle contacts and the material properties. The force-displacement behavior at each contact is governed by the normal stiffness k_n , the shear stiffness k_s , and the coefficient of friction μ . The net normal force F^n and net shear force F^s are calculated based on the approach described by Potyondy et al. [149].

The contact force \mathbf{F}_i exerted by particle A on particle B is decomposed into normal and tangential components relative to the contact plane:

$$\mathbf{F}_i = F^n \mathbf{n}_i + F^s \mathbf{t}_i \quad (6.1)$$

where F^n and F^s represent the normal and shear components, respectively, and \mathbf{n}_i and \mathbf{t}_i are the corresponding direction vectors defining the contact plane.

The normal force is given by:

$$F^n = K^n U^n \quad (6.2)$$

where U^n is the overlap between two spheres [as shown in Fig. 6.1(a)], and K^n is the normal stiffness constant of the particles.

The change in shear force ΔF^s due to a relative shear displacement ΔU^s is expressed as:

$$\Delta F^s = -K^s \Delta U^s \quad (6.3)$$

where K^s is the shear stiffness of the particles.

At any time step of duration Δt , the relative displacement is calculated as:

$$\Delta U_i = V_i \Delta t \quad (6.4)$$

where V_i is the contact velocity, which depends on both the translational and rotational velocities of the i^{th} particle.

Similarly, the relative shear displacement is given by:

$$\Delta U_s = (V_i - V_i^n)\Delta t \quad (6.5)$$

If a gap exists between the particles, meaning $U^n \leq 0$, both the normal and shear forces become zero.

The cement-based bonds between particles are modeled as elastic springs uniformly distributed over a circular cross-sectional area, capable of transmitting both force, F_i , and moment, M_i , between the particles. Each bond has a normal stiffness per unit area, k_n , and a shear stiffness per unit area, k_s , as well as tensile and shear strengths, σ_c and τ_c . The radius of a parallel bond, \bar{R} , is determined by the equation:

$$\bar{R} = \lambda \min(R^A, R^B) \quad (6.6)$$

where λ is the bond-radius multiplier, which was kept constant at $\lambda = 1.0$ throughout the simulation.

As with the contact forces, the total force and moment in each bond are resolved into normal and shear components relative to the contact plane. Initially, the forces and moments on the bonds are set to zero. As the particles experience relative displacements and rotations, the elastic force and moment values increase and are applied to the bonds. These incremental changes in forces and moments are expressed as:

$$\Delta \bar{F}^n = k^n A \Delta U^n \quad (6.7)$$

$$\Delta \bar{F}^s = -k^s A \Delta U^s \quad (6.8)$$

$$\Delta \bar{M}^n = -k^s J \Delta \theta^n \quad (6.9)$$

$$\Delta \bar{M}^s = -k^n I \Delta \theta^s \quad (6.10)$$

where $\Delta \theta^n$ and $\Delta \theta^s$ are the rotational increments in the normal and tangential directions, respectively, while A , I , and J represent the cross-sectional area, the moment of inertia, and the polar moment of inertia of the bonds, respectively.

The maximum stress on a bond is calculated using beam theory:

$$\sigma^{max} = \frac{-\bar{F}^n}{A} + \frac{|\bar{M}^s| \bar{R}}{I} \quad (6.11)$$

$$\tau^{max} = \frac{|\bar{F}^s|}{A} + \frac{|\bar{M}^n| \bar{R}}{J} \quad (6.12)$$

If the maximum tensile stress exceeds the tensile strength ($\sigma^{max} \geq \sigma_c$) or the maximum shear stress exceeds the shear strength ($\tau^{max} \geq \tau_c$), the spring breaks.

The ratios (K^n/K^s) and (k^n/k^s) are linked to the Poisson ratio of the material, and increasing these ratios for a given grain shape and packing increases the material's Poisson ratio.

6.3 Structure Generation

To study fractures in both ordered and disordered porous materials, two different sample generation techniques were employed.

The **ordered samples** were created by arranging monodispersed spheres in a hexagonal symmetry. Figure 6.2(a) illustrates this hexagonal structure, where each particle has a radius of 0.036 cm.

For the **disordered porous system**, spherical particles with an elastic modulus Y were deposited under gravity into a 3-dimensional box with dimensions of $1 \times 1 \times 1 \text{ cm}^3$. The radii R of the spherical particles were randomly selected from a log-normal probability distribution. These particles were allowed to settle under gravity using DEM, forming a 3-dimensional granular porous medium. The disordered system used in this study had a log-normal distribution of radii with a mean radius of 0.04 cm and a standard deviation of 0.003 cm, as depicted in Fig. 6.1(b).

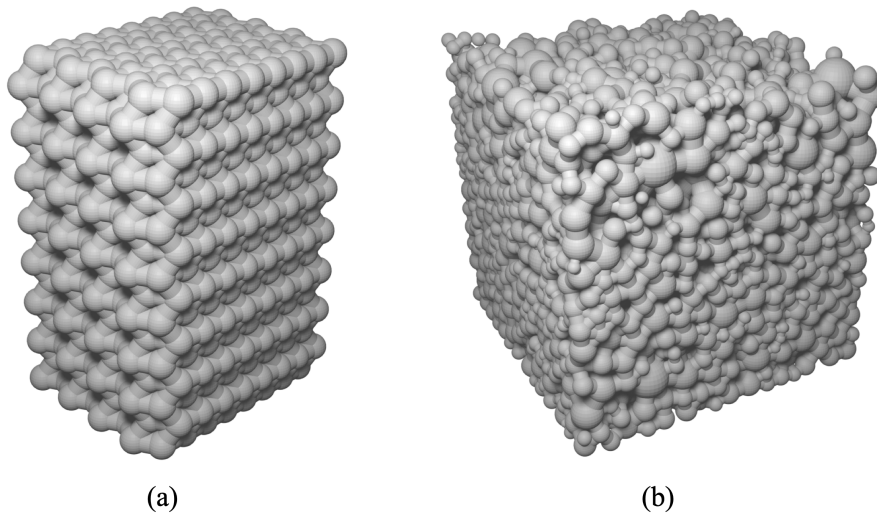


Fig. 6.2 (a) Material generated by hexagonal packing of monodispersed spheres with a radius of 0.036 cm. (b) 3-dimensional rectangular parallelepiped constructed from spheres with a log-normal distribution, mean radius of 0.04 cm, and standard deviation of 0.003 cm.

6.4 Results and Discussion

After generating the structures, axial compressive stress was applied to the top surface of the rectangular parallelepiped. A rigid wall was assumed to contact the top surface, descending at a velocity of V_w . It was further assumed that any sphere within the system could detach if all the bonds connecting it to neighboring spheres were broken. In line with the DEM scheme, the bonds between spheres could deform through either elongation or twisting. When a bond breaks, the load is redistributed among the remaining intact bonds. As more micro-cracks develop (i.e., as more bonds break), the stress on the remaining bonds increases.

Since the normal and shear stiffnesses are linked through the Poisson ratio of the material, the relation is given by:

$$k^n = \nu k^s = k_b \quad (6.13)$$

where ν is a constant, set to a value of 2.5. Additionally, the shear strength and the normal strength were taken to be the same, i.e., $\sigma_c = \tau_c$.

6.4.1 Fracture in the Hexagonal Arrangement of Spheres

Figure 6.3 shows the snapshots of the hexagonal structure at different times when subjected to uniaxial compression. The structure undergoes a failure, and the crack planes can be noticed in Fig. 6.3(c)

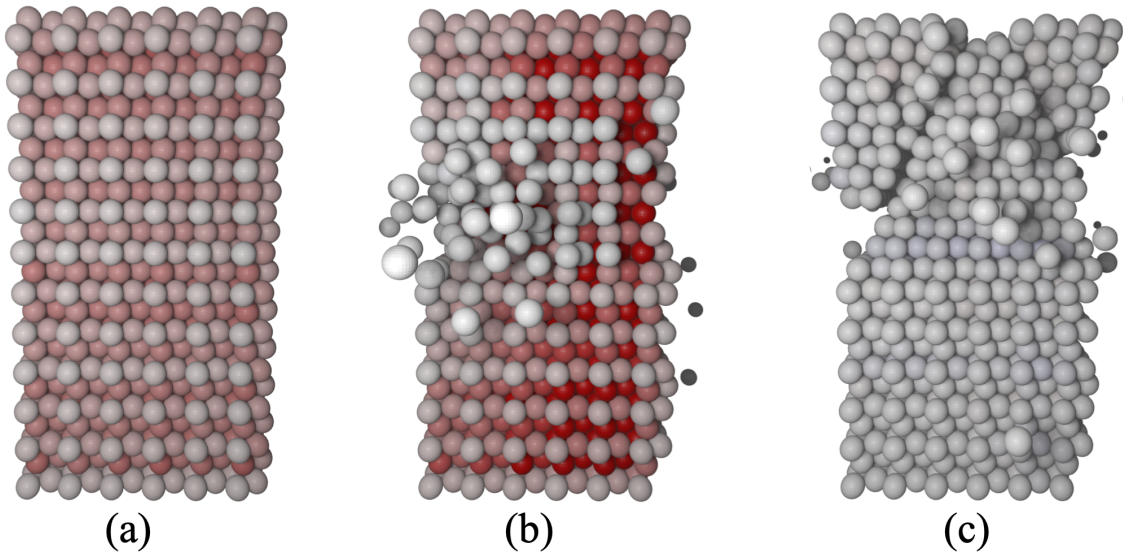


Fig. 6.3 Snapshots of the material at different times under compressive loading. Stress on the particles is color-coded.

The stress-strain behavior is illustrated in Fig. 6.4. Initially, within the elastic limit, the stress exhibits a linear relationship with strain, adhering to Hooke's law. This phase represents the material's ability to return to its original shape upon unloading. As the strain increases beyond this region, the material begins to experience irreversible deformations. Approaching the failure point, micro-cracks initiate and propagate, weakening the material's structural integrity. At the point of failure, a sudden avalanche of bond breakages is observed, Fig. 6.4(a), signifying a rapid release of stored energy. This cascade of bond failures leads to a sharp drop in stress, indicating the material's transition from an elastic to a fractured state. The behavior beyond the failure point can be associated with the formation of large-scale fractures or complete structural collapse, depending on the material properties and loading conditions. Figure 6.4(b) compares two materials with different Young modulus. The curve is steeper for

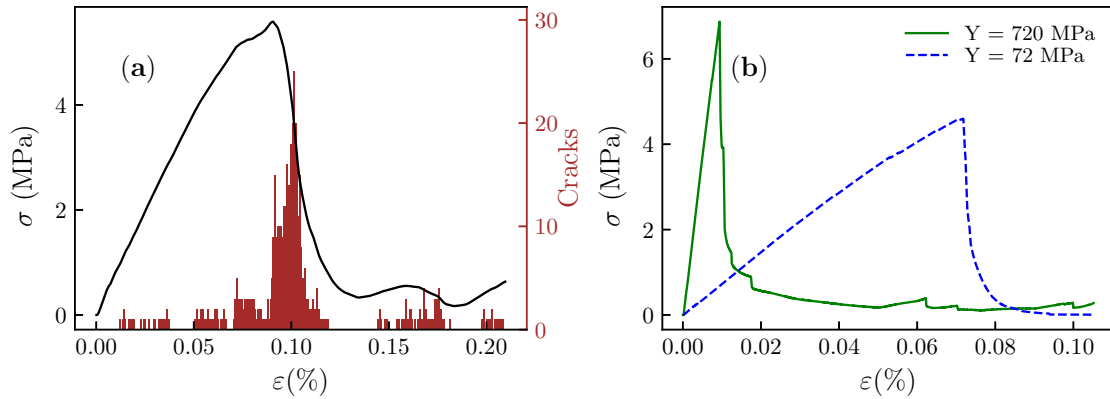


Fig. 6.4 (a) Typical stress-strain behavior of the generated materials. The red bars represent the number of bonds broken. (b) Stress-strain curve for different Young modulus, Y . A higher Young modulus shows a steeper slope.

the material with a higher Young modulus, as expected. An animated video illustrating the fracturing process can be found in Ref. [153].

6.4.2 Fracture in Disordered Systems

Although crack formation can be affected by all the intrinsic characteristics of grain and bonding material and the external loading, we only vary the cementing bond properties while studying the disordered systems. Thus, the grain (sphere) elastic properties are kept constant in this work, with $Y = 5$ MPa. We investigated crack statistics by (i) varying the stiffness constant k_b of the bond spring, keeping the bond spring threshold σ_c constant; (ii) varying the spring

threshold σ_c of the bond while keeping the spring stiffness k_b constant. The wall velocity is kept constant at 1 cm s^{-1} .

Fixed Bond Strength, Varying Stiffness Constant

Under the condition of fixed bond strength $\sigma_c = 100 \text{ MPa}$ and different values of stiffness k_b , the number of micro-cracks was plotted with increasing axial strain as shown in Fig. 6.5(a). The number of micro-cracks N^{k_b} sharply increased with an increase in strain up to a maximum peak value $N_{max}^{k_b}$, after which the crack number decreased slowly, showing a long tail. $N_{max}^{k_b}$ was found to decrease with decreasing k_b , but had longer tails. Higher bond stiffness of the springs representing the cementing material implies that many springs in the system can accumulate strain for a greater number of time steps before the breaking threshold is reached. The crack burst sizes are bigger, contributing to the higher value of $N_{max}^{k_b}$ observed in this case. The number of intact springs that survive after the maximum is smaller. These, too, survive a short time due to accumulated strain, so a shorter tail is observed here. It is observed that the strain value ϵ_{max} corresponding to $N_{max}^{k_b}$ decreased with increasing bond stiffness k_b as expected. Plotting the variation of both ϵ_{max} and $N_{max}^{k_b}$ with bond stiffness k_b showed a power-law dependence in each case as shown in Figs. 6.5(b) and (c).

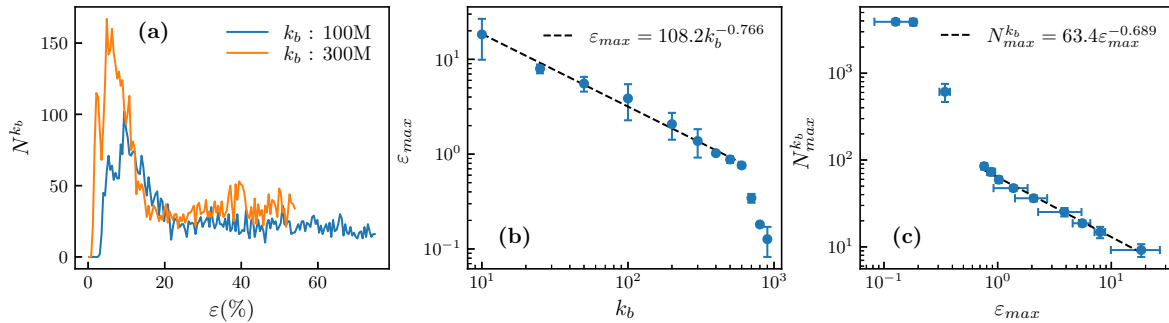


Fig. 6.5 (a) Variation of the number of cracks N^{k_b} versus axial strain for different bond stiffness and constant bond strength σ_c . (b) Log-Log plot of strain at maximum crack number $N_{max}^{k_b}$ versus bond stiffness k_b . (c) Log-Log plot of strain at maximum crack number $N_{max}^{k_b}$ versus corresponding strain.

The asymmetric distribution of the micro-cracks may be explained in the following way: with an increase in axial strain, the initial fracturing is more brittle, as manifested in the sharp growth rate of cracks. However, the cracks that begin as small bursts rapidly spread through the system as more and more load is shared by the intact bonds to compensate for the loss of broken bonds. Beyond a critical strain ϵ_{max} , the micro-cracks start merging, and the system

moves towards a percolating failure with fewer bonds getting broken with a further increase in strain. For our log-normal particle size distribution, the graphs in Figs. 6.5(b) and (c) indicate that the strain value at the maximum number of micro-cracks follows a power-law trend with a negative exponent of 0.766 as the bond stiffness increases. Additionally, a log-log plot of the maximum number of micro-cracks versus the corresponding strain value for different k_b also demonstrates a power-law relationship with a negative exponent of 0.689.

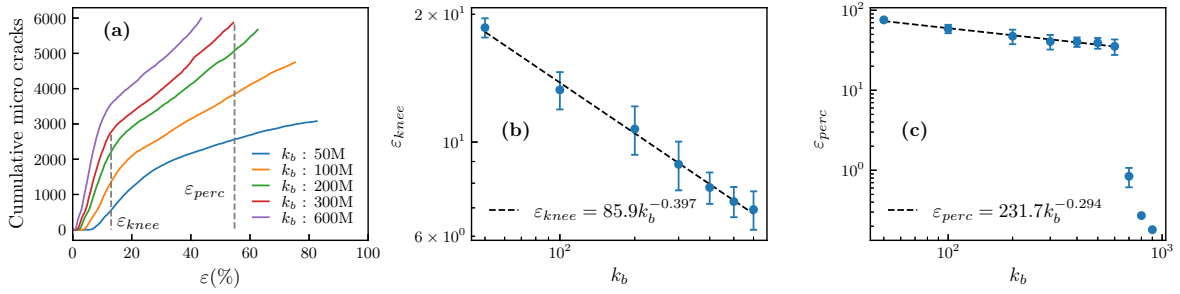


Fig. 6.6 Crack statistics for constant spring threshold $\sigma_c = 100$ MPa, and variable bond stiffness constants $k_b = 50, 100, 200, 300, 600$. Values are in units of MPa m^{-1} . (a) Cumulative micro-cracks versus strain percentage. The dotted line is indicative of the transition between different cracking modes for $k_b = 300$ MPa m^{-1} . (b) Variation of ϵ_{knee} with k_b follows a power law with exponent $m_{knee} = -0.397$ (c) Variation of ϵ_{perc} with k_b follows a power law with exponent $m_{perc} = -0.294$

Figure 6.6(a) shows that when the spring stiffness k_b is varied, keeping the bond breaking threshold $\sigma_c = 100$ MPa constant, the cumulative cracks in the system increase with the percentage of strain in the system. Every curve shows two distinctly different growth regions about a knee point, the strain at the knee being denoted by ϵ_{knee} . Interestingly, a comparison of Figs. 6.5(a) and 6.6(a) show that the maximum number of micro-cracks corresponds to the knee point strain ϵ_{knee} . The endpoint of each curve corresponds to the point of percolation in the system; the corresponding strain is denoted as ϵ_{perc} . Both ϵ_{knee} and ϵ_{perc} decrease with increasing values of k_b , and show a power-law dependence, Figs. 6.6(b) and (c), of the form:

$$\epsilon_{knee} = A k_b^{-m_{knee}} \quad (6.14)$$

and

$$\epsilon_{perc} = B k_b^{-m_{perc}} \quad (6.15)$$

The exponents have values $m_{knee} = 0.397$ and $m_{perc} = 0.294$; A and B are constants characteristic of the system. Combining Eqs. (6.14) and (6.15), we get a relation between ϵ_{knee} , ϵ_{perc} ,

m_{knee} and m_{perc} given by

$$\varepsilon_{perc} = D\varepsilon_{knee}^m \quad (6.16)$$

Thus Eq. (6.16) indicate that ε_{knee} has a power-law scaling with ε_{perc} with the exponent $m = \frac{m_{perc}}{m_{knee}} = 0.740$

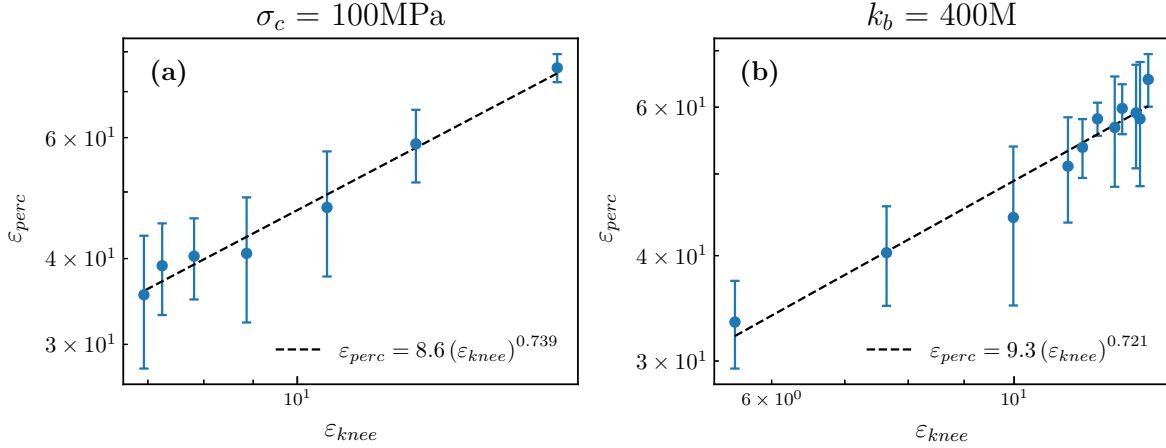


Fig. 6.7 Log-log plot of ε_{perc} versus ε_{knee} (a) For constant breaking threshold $\sigma_c = 100$ MPa and varying stiffness constant k_b . A power-law behavior is indicated with exponent $m = 0.739$. (b) For constant stiffness constant $k_b = 400$ MPa m⁻¹ and varying breaking threshold σ_c . A power-law behavior is indicated with exponent $m = 0.721$

Using the data points from our simulation, we construct the variation of ε_{perc} versus ε_{knee} as shown in Fig. 6.7(a). A power-law behaviour is observed with the exponent $m = 0.739$ agreeing almost exactly with the theoretical value of 0.740. We repeated this study with two other constant bond strength values of $\sigma_c = 500$ MPa and 1000 MPa, and variable bond stiffness constants. The nature of the cumulative cracks versus strain graphs showed similar crack statistics as observed for $\sigma_c = 100$ MPa.

Fixed Stiffness Constant, Varying Bond Strength

In the situation where crack statistics on the same system was studied for a fixed bond stiffness constant $k_b = 400$ MPa m⁻¹ and the breaking threshold of spring σ_c varying from 50 MPa to 1000 MPa, the variation of cumulative micro-cracks increased with axial strain as expected. Similar to the situation where σ_c was fixed and k_b varied, two distinctly different growth rates were observed across a knee strain, Fig. 6.8(a). The strain at the knee point ε'_{knee} and the percolation point ε'_{perc} for each plot of bond strength was noted. These values, when plotted versus bond strength on a log-log scale, could be fitted approximately by a straight line

indicative of a scaling behavior, Figs. 6.8(b) and (c). The exponents m'_{perc} and m'_{knee} had values 0.206 and 0.274 respectively.

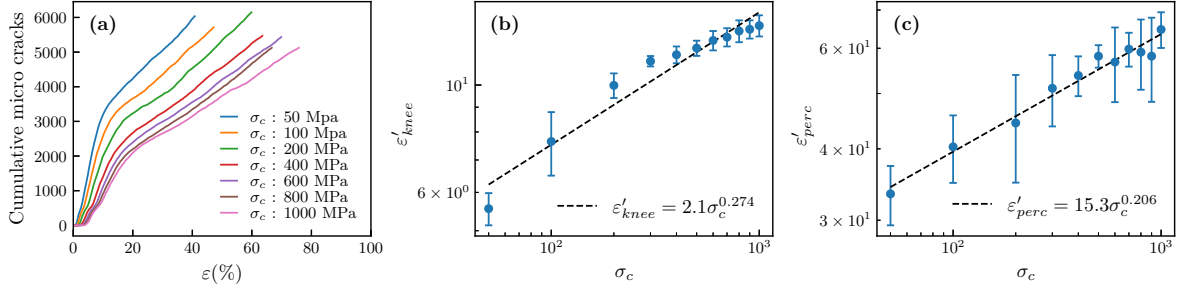


Fig. 6.8 Crack statistics for constant spring stiffness $k_b = 400$ MPa, and variable spring breaking thresholds $\sigma_c = 50, 100, 200, 400, 600, 800, 1000$. Values are in units of MPa. (a) Cumulative micro-cracks versus strain percentage. (b) Variation of ϵ'_{knee} with σ_c follows a power law with exponent $m'_{knee} = 0.274$ (c) Variation of ϵ'_{perc} with σ_c follows a power law with exponent $m'_{perc} = 0.206$

Using the same procedure as described between Eqs. (6.14) to (6.16), a relation between ϵ'_{knee} , ϵ'_{perc} , m'_{perc} and m'_{knee} was constructed :

$$\epsilon'_{perc} = D' \epsilon'_{knee}{}^{m'} \quad (6.17)$$

Thus Eq. (6.17) is similar to Eq. (6.16), i.e., ϵ'_{knee} has a power-law scaling with ϵ'_{perc} with the exponent $m' = 0.752$. Using the data points of our simulation, we constructed the variation of ϵ'_{perc} versus ϵ'_{knee} on a log-log scale as shown in Fig. 6.7(b) for constant bond strength $k_b = 400$ MPam⁻¹. A power-law behavior between the parameters was obtained with the exponent $m' = 0.721$, which is close to the theoretical predicted value of 0.752.

It may be recalled that the systems under examination are highly disordered. The size distribution of the grains adds to the complexity, and the Distinct Element Method (DEM) can be computationally expensive when applied to 3-dimensional systems. The difference between the theoretical and experimental values of the exponents m and m' can be better matched when crack statistics are calculated on a larger system.

From our results and analysis so far, we propose that the scaling relation between the strain at the knee ϵ_{knee} and at the percolating point ϵ_{perc} as given by Eqs. (6.16) and (6.17), can have useful applications as an indicative precursor to the percolating point of a 3-dimensional system. Micro-cracks are detected as acoustic signals in experiments. As DEM factors in individual particle interactions and resultant deformations in relation to the rest of the system, with all system parameters known, the exponent m/m' for a porous system can be estimated

accurately. One can detect ε_{knee} via acoustic emissions and can have an estimate of ε_{perc} . Though a percolation plane ultimately leads to complete failure in a 3-dimensional structure, the pre-knowledge of ε_{perc} certainly shall act as a red flag.

6.5 Conclusions

In this work, we investigated how material properties influence crack formation in a porous granular system under compressive strain. Using a 3D disordered model, spherical particles were bonded by cement with differing elastic properties. Compressive strain was applied, and the resulting stress-strain progression and crack dynamics were analyzed to understand how variations in bond stiffness and strength affect micro-crack development and the onset of a percolating crack.

Two scenarios were studied: (1) varying bond stiffness while keeping bond strength constant and (2) varying bond strength while keeping stiffness constant. In both cases, the cumulative crack count increased with strain, but the rate of increase shifted notably at a critical strain value, ε_{knee} . This critical strain decreased with higher bond stiffness and increased with greater bond strength, following a power-law relationship with distinct exponents in each case. The strain at percolation, ε_{perc} , followed a similar pattern, revealing a robust scaling relationship between ε_{knee} and ε_{perc} as a function of bond properties.

This scaling law, tested across different cementing materials, suggests that predicting the onset of percolation cracks is possible by monitoring micro-crack statistics. Given known values of stiffness and strength for common materials and exponents derived from simulations, this relationship enables estimating the strain threshold before percolation cracking – and ultimately system failure – occurs. Identifying this threshold provides an early warning of system damage before complete fragmentation in 3D systems.

Chapter 7

Fluid Flow in Porous Media

7.1 Introduction

Understanding flow through porous media remains a vibrant research area due to its significant real-world applications. This includes subsurface flows vital for agriculture, oil and gas extraction, CO₂ sequestration in sedimentary rocks, and various engineering uses. Fluid movement through the pore space of a 3D granular structure presents a complex non-linear challenge that relies heavily on modeling and simulation for solutions. Laboratory experiments often fail to fully replicate in-situ conditions, serving only as approximate guides. In real scenarios, like sedimentary rocks, fluid transport is characterized by system properties such as permeability or conductivity. These macro-scale properties, however, are influenced by micro- to mesoscale factors like grain size and shape, which can vary greatly. Additionally, fluid behavior in the porous matrix is impacted by surface tension, while viscosity determines whether the flow exhibits capillary or Saffman-Taylor instabilities [154, 155].

Continuum-scale models that connect permeability and capillary pressure typically assume fluid saturation [156, 157], and their results can depend on both the material and the process [158, 159]. To create constitutive models that are more widely applicable, a geometric description of the pore space and its relationship to transport properties is necessary. Efforts have been made to link the permeability of porous systems to the Euler characteristic, a topological measure, in 2D porous media [160], where grain overlap plays a crucial role. However, in real 3D systems, grain overlap is not as significant. Katz and Thomson [161] suggested that permeability (k) and electrical conductivity (σ) in porous systems are related through a characteristic length (l_c) of the system by

$$k = cl_c^2 \left(\frac{\sigma}{\sigma_0} \right) \quad (7.1)$$

where c is a constant that depends on pore geometry, and l_c represents the critical pore diameter that prevents particles with an average diameter larger than l_c from percolating through the system. Additionally, σ_0 is the fluid conductivity. Archie's law, which provides an empirical relationship between conductivity and the porosity of a porous rock, is most accurate near the percolation threshold of the porous medium and has been validated through simulations [162–164], though there are exceptions [165–167]. Interfacial energy and fluid topology also play crucial roles in influencing fluid flow through porous media [168–172]. More general solutions have been derived using integral geometry techniques [173–181]. For example, McClure et al. [182] applied a non-dimensional relationship based on the Minkowski–Steiner formula [183] to predict fluid flow based on the geometric characteristics of various porous rocks.

This work draws inspiration from Hadwiger's characterization theorem, which suggests that the structure of finite unions of convex subsets in 3-dimensional systems can be described using no more than four invariant measures, known as the Minkowski functionals [184]. Given that the grains in porous media can generally be assumed to be convex, it is reasonable to expect that transport properties, such as permeability, may be connected to these basic geometric invariants. To explore this, we simulated 3D porous structures—both stochastic and deterministic—using specific construction algorithms. For the stochastic structures, particle sizes followed a distribution around a mean size, while the deterministic structures used particles of constant size, which varied over a range.

We calculated the permeability of each structure by simulating incompressible fluid flow under constant pressure gradients, conserving mass and momentum. The topological invariant, Euler characteristic (χ), was determined for the pore space, along with the characteristic critical length (l_c), integral mean curvature (H), and the average cross-sectional area of the pore space. Our study found that permeability followed a power-law relationship with each of these geometric invariants. This consistent behavior across invariants led us to formulate an empirical relationship between permeability (k) and a combinatorial function (F) derived from the four geometric characteristics, which displayed a power-law behavior regardless of the pore size distribution.

Remarkably, the exponent of this scaling relationship was nearly identical for both a 3D self-organized disordered system at equilibrium and a 3D deterministic system with geometric symmetry. To our knowledge, this is the first instance of a unified relationship linking fluid flow with all Minkowski functionals, characterized by a unique exponent for 3D disordered porous systems. The relationship was constructed by systematically examining the variation of permeability with each geometric descriptor. Systems with cubic and hexagonal symmetries represented the upper and lower bounds of the scaling relations, while disordered systems fell between these bounds.

Our proposed scaling relations proved robust to variations in pore size and micro-geometry, with the exponent remaining consistent across both stochastic and deterministic systems.

In the following sections, I will outline the methodology for constructing both stochastic and deterministic 3D porous systems, the determination of the flow characteristic (k), and the computation of each invariant geometric measure for every structure. This will be followed by the presentation of results, discussion of the scaling relationship, and a conclusion summarizing our findings and future directions for this research.

7.2 Porous Structure Generation

To simulate fluid flow through porous structures, we generated a 3-dimensional porous stochastic structure and modeled the flow of a single fluid using a numerical finite difference solution of the steady-state Navier-Stokes equation. Since most naturally occurring porous rocks exhibit a log-normal particle size distribution [185], spherical particles with radii R were randomly selected from a log-normal distribution with a mean radius $\langle R \rangle$ and standard deviation s . The radii of these particles were constrained within the range of $\langle R \rangle/4$ to $5\langle R \rangle$ to avoid extreme particle sizes.

In addition to log-normal distributions, we constructed a second class of 3-dimensional disordered systems using a normal distribution for particle sizes. The particles were allowed to settle under gravity within an imaginary cubic box of size $L = 0.5$ cm. The forces acting on the particles during the generation of these structures were computed using the Distinct Element Method (DEM). By varying $\langle R \rangle$ and the standard deviation s , we could generate different samples, with approximately 2000 particles used to create each sample, depending on the value of $\langle R \rangle$.

For comparison, deterministic 3-dimensional structures were also generated, using spheres of equal radius and contained within cubic boxes of size L . These deterministic structures were examined for two symmetric arrangements: (i) hexagonal and (ii) cubic. Six different radii were selected to generate samples for each symmetry configuration.

7.3 Geometric Characterization of Porous Medium

Regardless of the total porosity of the samples, we considered the **effective porosity** ϕ_0 of the sample spanning channels, as this porosity alone contributes to fluid flow. To identify sample spanning clusters and the geometrical characteristics of the system, we superposed a $256 \times 256 \times 256$ cubic grid on the 3-dimensional structure with grid length $\delta x \sim 0.002$ cm. The porous structure was discretized by assigning a grid cell a value of 1 if at least 50% of

the cell was filled by the matrix. Otherwise, the grid cell was given a value of 0. This process converted the porous structure into a binary format.

An effective **critical area** $A_c = \frac{\pi}{4}l_c^2$ was calculated after the determination of the critical length scale l_c - defined as the maximum diameter of a spherical particle that can percolate through the system spanning channels. After all the system-spanning channels were identified via the Hoshen-Koppelman algorithm, a sorting algorithm was used to determine l_c for each sample.

The topological invariant, **Euler Characteristic** χ defined as an alternating sum of Betti numbers :

$$\chi = \beta_0 - \beta_1 + \beta_2 - \dots \quad (7.2)$$

where the β_0 represents the number of connected components, β_1 is the 1-dimensional holes or loops, β_2 represents the 2-dimensional voids or cavities, and so on. For 3-dimensional porous systems constructed only by spheres Eq. (7.2) can be simplified to [186]

$$\chi = M - I + N \quad (7.3)$$

where M is the number of isolated pores, I refers to the number of intersections between grains, i.e., the number of points where two grains touch each other at a point, and N is the number of grains completely enclosed by the pores. The Euler characteristic can be considered to be a measure of connectivity that yields positive values for structures with low connectivity, where M (isolated pores) exceeds I (intersections), and negative values for more highly connected structures, where M is less than I . In the DEM scenario of particles falling under gravity for the 3-dimensional construction, there is a finite probability of the intersections being circles. However, the particle overlap is assumed to be negligibly small compared to particle size and hence neglected. The Euler Characteristic χ provides a measure of the connectivity in the sample and is very relevant for fluid flow studies.

The integral **mean curvature** H of a particle is given by the surface integral

$$H = \int \frac{\kappa_1 + \kappa_2}{2} ds \quad (7.4)$$

where κ_1 and κ_2 are the principal radii of curvature of the grain. For a spherical grain $\kappa_1 = \kappa_2 = \frac{1}{R}$. The mean curvature of the void surface of an assembly of spherical particles is

$$H = \sum_i \frac{1}{R_i} 4\pi R_i^2 = 4\pi \sum_i R_i \quad (7.5)$$

7.4 Fluid Transport

Fluid transport in a porous structure under a suitable pressure gradient is described by the Navier-Stokes equation

$$\rho \frac{\delta \mathbf{V}}{\delta t} + (\mathbf{V} \cdot \nabla) \mathbf{V} + \nabla P - \mu \nabla^2 \mathbf{V} = f_e \quad (7.6)$$

where \mathbf{V} , P and f_e represent the velocity, pressure, and external force per unit volume respectively, ρ and μ are respectively the density and dynamic viscosity of the fluid. Neglecting the inertial term and assuming no external forces acting on the fluid, Eq. (7.6) simplifies to

$$\frac{\delta \mathbf{V}}{\delta t} = -\frac{1}{\rho} \nabla P + \eta \nabla^2 \mathbf{V} \quad (7.7)$$

where $\eta = \frac{\mu}{\rho}$ is the kinematic viscosity. For an incompressible fluid, the equation of continuity is

$$\nabla \cdot \mathbf{V} = 0 \quad (7.8)$$

Equations (7.7) and (7.8), when solved together, give the steady state condition of flow in the structure.

The Hoshen-Kopelman algorithm [187] was employed to identify the channels spanning the sample. The pressure and velocity fields were solved using the approach outlined by Sarkar et al. [114], with certain modifications made to better suit the specific requirements of our problem. The discretized space and time versions of Eqs. (7.7) and (7.8) were iteratively applied to reach steady-state flow conditions, as described in Sadhukhan [85]. Steady state was considered achieved when the velocity difference between consecutive time steps of iteration was less than or equal to 10^{-9} . Our simulation involved a single fluid injection, and the steady-state velocity and pressure values at all points along the spanning transport channels were recorded. The permeability was calculated according to Darcy's law

$$\mathbf{q} = \frac{k}{\mu} \nabla P \quad (7.9)$$

where \mathbf{q} is the flux, k the permeability, μ the viscosity and ∇P the pressure gradient across the sample.

7.5 Results and Discussion

The 3-dimensional porous structures were generated as previously described. We constructed two stochastic structures with particle size distributions selected from (i) log-normal and (ii)

normal distributions. These distributions were centered around mean particle sizes $\langle R \rangle$ ranging from 0.02 cm to 0.045 cm, with standard deviations s varying from 0.0025 cm to 0.015 cm. All results were averaged over 30 configurations. Since the macroscopic cubic structure's length, L , was kept constant, the number of particles, N , varied from 419 to 3656, depending on particle sizes. Additionally, we constructed two deterministic porous structures with (i) cubic and (ii) hexagonal symmetries. Figure (7.1) shows representative images of the four different types of 3D porous structures generated for this study.

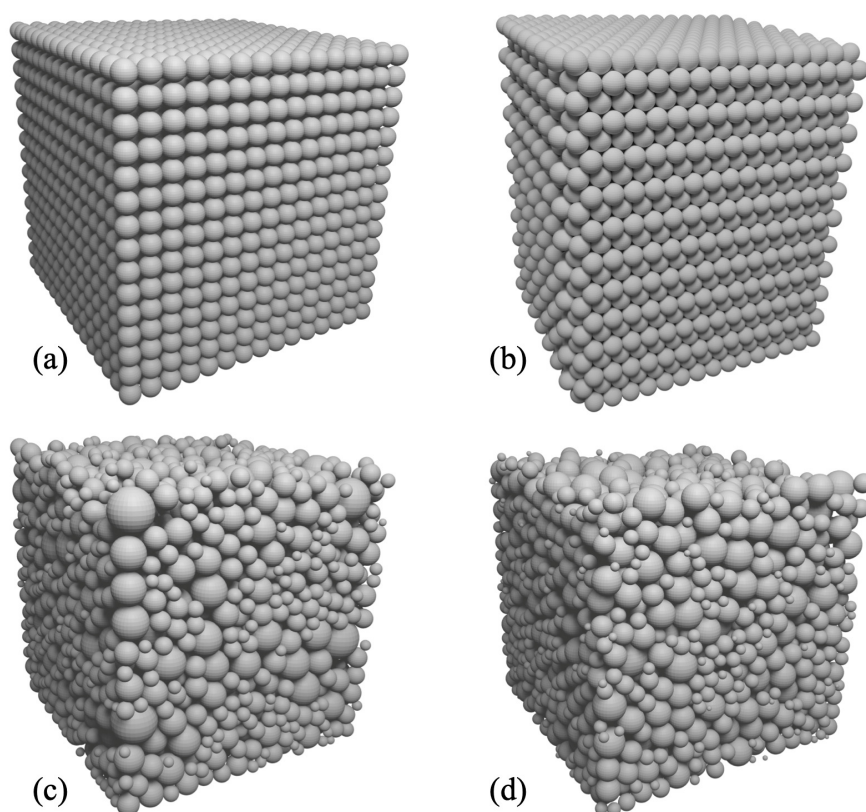


Fig. 7.1 3-dimensional porous structures generated using DEM. (a) Deterministic structure having cubic symmetry (b) Deterministic structure having hexagonal symmetry (c) Stochastic structure with particle size chosen from a log-normal distribution. (d) Stochastic structure with particle size chosen from a normal distribution.

After structure generation, the sample spanning void clusters were identified to study fluid transport. The direction of the pressure gradient was identified as the z-axis of the system and was identical to the direction of particle deposition. For the stochastic structures, we determined the 2-point density correlation function $S_2(r)$, defined by

$$S_2(r) = \langle p(r')p(r+r') \rangle \quad (7.10)$$

where $p(r)$ defines the probability of finding a void at position r . For the stochastic systems, the variation of $S_2(r)$ versus r computed along each axes for a typical sample, Fig. 7.2(a), indicates that the sample was isotropic in the transverse (x-y) plane. A slight anisotropy along the z-axis, the direction of grain deposition, is indicated.

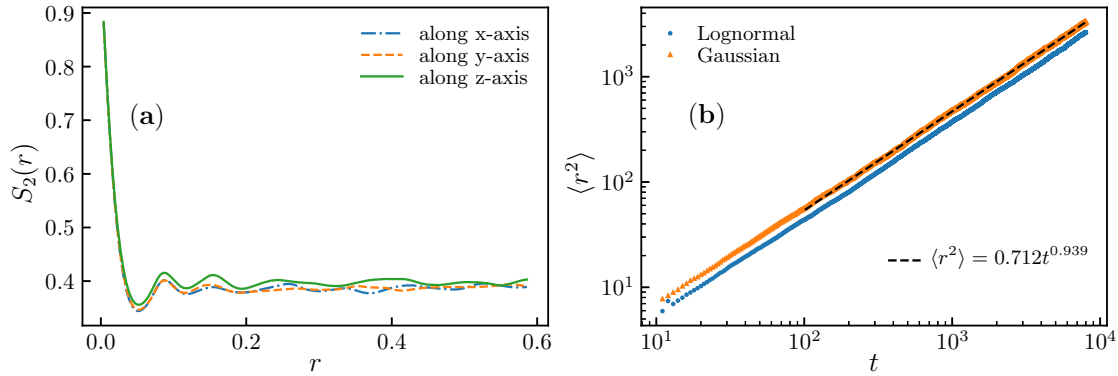


Fig. 7.2 Typical micro-geometric characteristic of 3-dimensional stochastic porous systems. Lognormal stochasticity is shown here. (a) Variation of 2-point correlation function $S_2(r)$ with r along principle axes. (b) Mean square displacement $\langle r^2 \rangle$ with time t shows subdiffusive behavior.

To understand the pore micro-geometry, we studied diffusion using a random walk algorithm; details are available in [188]. The mean square displacement $\langle r^2 \rangle$ showed a power law variation with time t , Fig. 7.2(b), indicative of subdiffusive behavior.

The geometric characteristics, including the Euler characteristic (χ), mean integral curvature, and effective porosity, were computed for each generated sample as discussed earlier. The permeability (k), a measure of fluid flow, was then determined for each sample. Steady-state flow was achieved by iteratively solving the space- and time-discretized versions of Eqs. (7.7) and (7.8), after which the pressure and velocity at every point in the sample's spanning void cluster were calculated.

To illustrate the pore space in our generated systems, Fig. 7.3(a) shows the porous structure of a disordered sample with a log-normal particle size distribution. Figure 7.3(b) depicts the percolating path through which a sphere of diameter l_c can freely pass. Figures 7.3(c) and (d) present the pressure distribution and the steady-state velocity field within the porous space when fluid flows under a constant pressure gradient. The output fluid flux was measured, and permeability for each sample was computed using Eq. (7.9).

Hadwiger's characterization theorem states that only four invariant measures are needed to describe a 3-dimensional system formed by a union of convex solids: (i) area, (ii) volume, (iii) the Euler characteristic, and (iv) integral mean curvature. Based on this, we hypothesized that

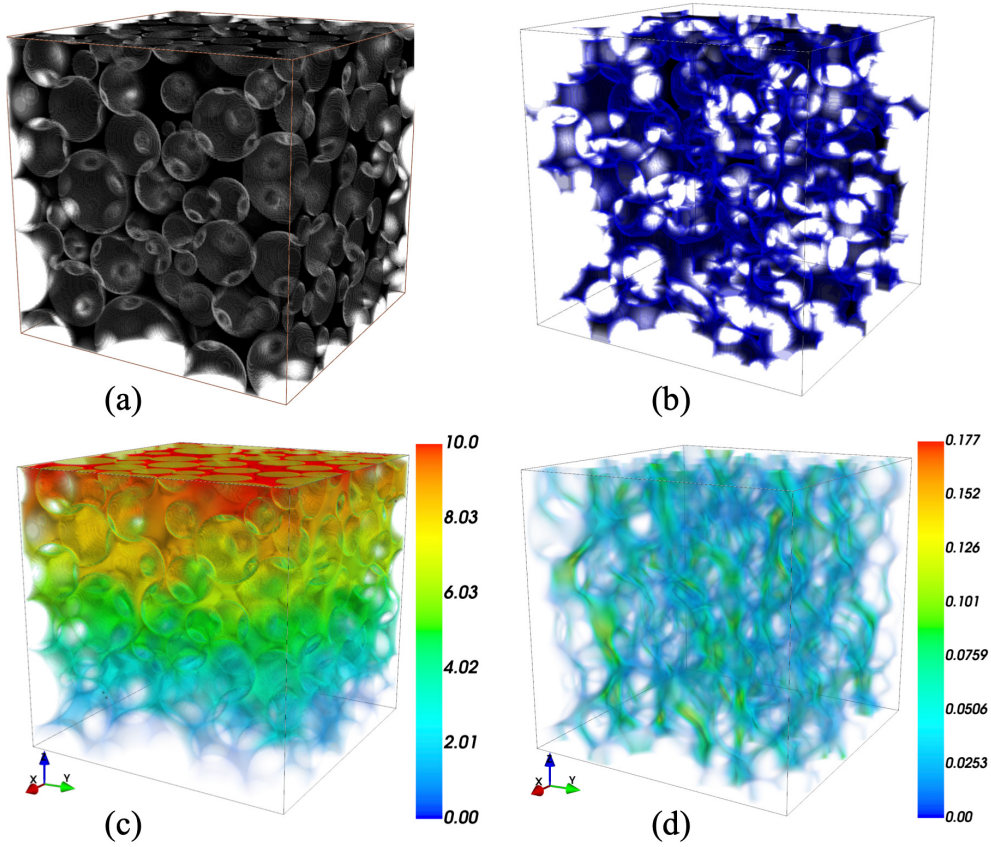


Fig. 7.3 (a) Porous structure of a log-normal stochastic sample, (b) the system-spanning path through which a sphere of diameter l_c can move freely, (c) pressure distribution inside the porous space, and (d) steady-state velocity profile across the sample. The color legends provide value scales in CGS units.

permeability could be expressed as a function of the Minkowski functionals: (i) the square of the characteristic length l_c , (ii) the integral mean curvature H , (iii) the topological measure of the Euler characteristic χ , and (iv) the effective porosity ϕ_0 , which is defined as the volume of the porous channel scaled by the system volume (a constant across all cases considered). To test this, we analyzed the variation of permeability with each of these geometric measures.

The permeability showed a power-law dependence on l_c^2 . It's worth noting that the effective cross-sectional area of the transport channel, A_c , is related to l_c^2 by the expression $A_c = \frac{\pi}{4}l_c^2$. Therefore, the variation of k with A_c follows a scaling relationship, as shown in Fig. 7.4(a):

$$k = C_1 A_c^{m_1} \quad (7.11)$$

with $m_1 \approx 1.066$. This indicates that permeability increases with A_c , meaning that larger pore throats enhance permeability, as expected.

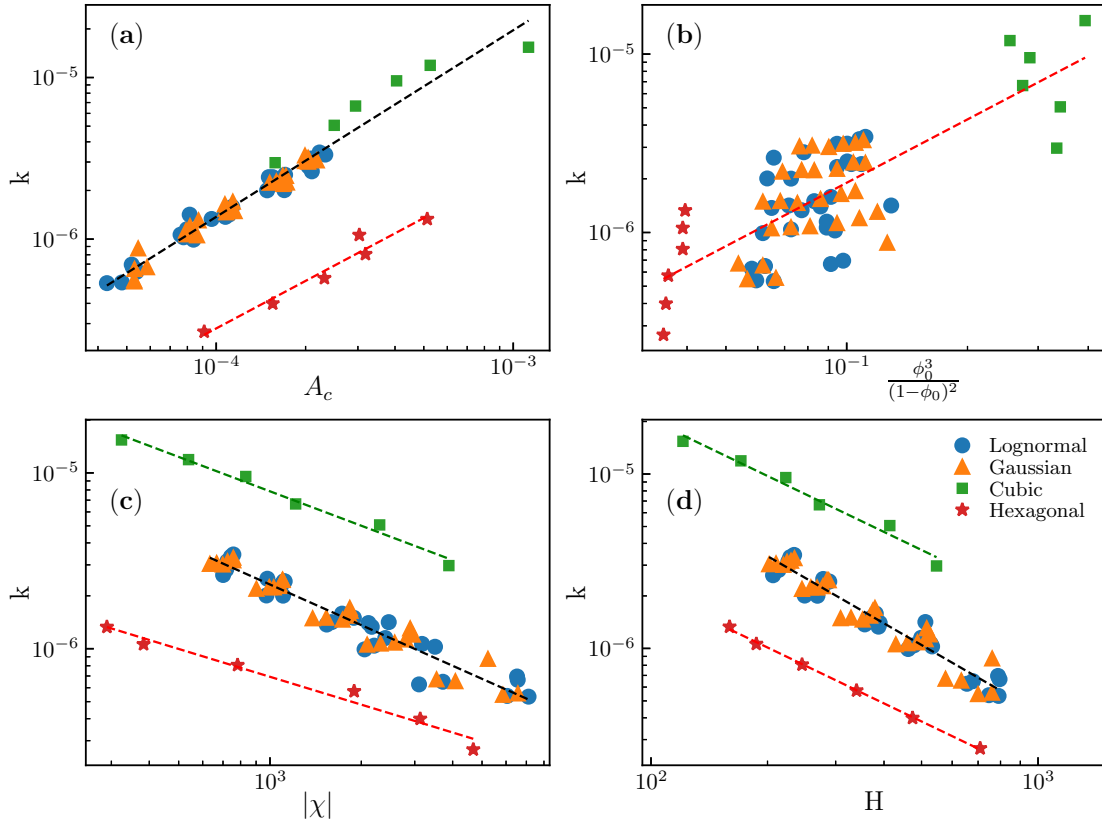


Fig. 7.4 (a) The log-log variation of permeability with A_c for the deterministic and stochastic 3-dimensional porous structures, (b) variation of permeability with porosity ϕ_0 , (c) the log-log variation of permeability with the Euler Characteristic χ , (d) the variation of permeability with the mean integral curvature.

When examining the relationship between permeability and effective porosity for the system, as shown in Fig. 7.4(b), the data points formed a cloud. Despite this, the clouds for different systems exhibited a power-law scaling of permeability, with an exponent $m_2 \approx 1.180$.

$$k = C_2 \left(\frac{\phi_0^3}{(1-\phi_0)^2} \right)^{m_2} \quad (7.12)$$

When the behavior of permeability was checked for variation in the topological connectivity measure the Euler Characteristic χ , permeability decreased with $|\chi|$ following a scaling behavior of the form, Fig. 7.4(c):

$$k = C_3 |\chi|^{-m_3} \quad (7.13)$$

The exponent $m_3 \approx 0.648$.

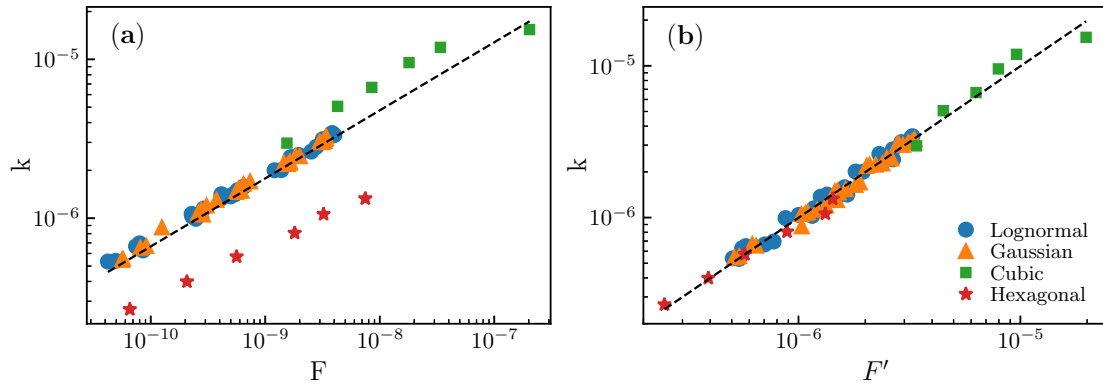


Fig. 7.5 (a) Variation of permeability k with F , a build-up function of the geometric invariants of the samples. (b) Variation of permeability k with F using regression shows a very good collapse on a single power-law scaling function irrespective of sample type.

Variation of permeability with the integral mean curvature H followed a scaling law of the form

$$k = C_4 H^{-m_4} \quad (7.14)$$

The exponent m_4 was almost identical for both the deterministic and the stochastic systems, being $m_4 \approx 1.17$, Fig. 7.4(d). Thus, smaller curvatures, i.e., larger spherical grains, left bigger voids in the system that were conducive to fluid flow.

The common features of our investigations so far have been:

- Permeability showed a power law dependence with each of the different geometric measures of the porous system, having the form:

$$k = Cx^m \quad (7.15)$$

with C a constant, x being any one of the geometric measures of the 3-dimensional system, and m being the corresponding exponent.

- In all the relations investigated, Eqs. (7.11) to (7.13), the exponents had, on average, identical values for all the systems.
- The variation of permeability with x in every case showed an upper bound for the cubic symmetry and a lower bound for the hexagonal packing. The values of k against x for the stochastic systems lay between these bounds, Fig. 7.4.

Our next step was to try and determine a single relationship between flow and the geometrical characteristics of the systems studied. Borrowing from the Kozeny-Carman equation [189]

and permeability studies in [190], and keeping in mind the Minkowski functionals, we proposed a relation between permeability and the geometrical parameters based on the behaviors obtained thus far:

$$k = A_c \frac{\phi_0^3}{(1 - \phi_0)^2} \frac{1}{|\chi|^{0.5}} \frac{1}{H} \quad (7.16)$$

where A_c is the critical cross-section that cuts off particles with cross-sections greater than A_c from percolating through the system; ϕ_0 is the effective porosity, i.e., the porosity associated with the system spanning channels. The R.H.S. of Eq. (7.16) can be clubbed together as a combinatoric $F = A_c \frac{\phi_0^3}{(1 - \phi_0)^2} \frac{1}{|\chi|^{0.5}} \frac{1}{H}$. Following Eq. (7.16), we plotted the variation of the permeability k with F on a log-log scale as shown in Fig. 7.5(a). Though there was a good suggestion of the collapse of all points for all four scenarios studied onto a single straight line, there remained a non-negligible scatter. However, for all the ordered and disordered systems studied, permeability followed a scaling relationship of the form

$$k = CF^{0.428} \quad (7.17)$$

This indicated that irrespective of the disorder in pore space for 3-dimensional systems built of spherical grains, permeability followed a scaling behavior with a combinatoric of the Minkowski functionals - A_c , ϕ_0 , χ and H , with a unique scaling exponent 0.428. The other notable part of our investigation is that the cubic and the hexagonal systems appear to provide the upper and lower bounds within which all values of k reside for their corresponding combinatoric F . While a more rigorous proof is required for the bounds to be established, one can argue that given a fixed box size (here L^3), hexagonal close packing will certainly minimize the pore volume and, therefore, permeability. On the other hand, cubic packing with uniform-sized spheres shall provide the maximum void space and increase k . Any other distribution of particle size is expected to show permeability values between these limits.

To obtain an almost perfect collapse of all data points onto a single straight line, we followed a regression of Eq. (7.16) of the form

$$k = \alpha(A_c)^a \left(\frac{\phi_0^3}{(1 - \phi_0)^2} \right)^b (|\chi|)^c H^d \quad (7.18)$$

with $\alpha = 0.0081$, $a = -0.328$; $b = 1.061$; $c = 0.075$, $d = -1.602$. If we represent the RHS of Eq. (7.18) by F' , Fig. 7.5(b) shows the variation of k with F' . It shows the power-law scaling of the form

$$k = C'(F')^{0.998} \quad (7.19)$$

We propose that the permeability of a 3-dimensional porous structure, irrespective of its pore size and distribution, follows a power-law scaling with the sample geometrical measures. Since we dealt with both ordered and disordered porous systems with various sizes and distributions of particles, the exponent 0.428 may be universal, at least for systems constructed with spherical grains.

7.6 Conclusions

Fluid flow through porous systems is a critical phenomenon that influences various aspects of everyday life. It is almost intuitive to expect that fluid transport properties like permeability and conductivity depend on the geometry of the pore space. Hadwiger's theorem, which states that any 3-dimensional system formed by a union of convex solids can be described by a linear combination of at most four geometric invariants (the Minkowski functionals), motivated us to investigate the correlation between permeability and these functionals.

We began by generating two types of disordered porous systems, both composed of spherical particles: one with a log-normal particle size distribution and the other with a normal distribution centered around specific mean sizes. At least six different mean sizes were used for this construction. To study the effect of disorder, we also created two perfectly ordered systems with different symmetries of grain arrangement: cubic and hexagonal. In order to emulate natural conditions, we allowed the particles to settle under gravity using discrete element modeling (DEM), achieving an equilibrium state. The flow of incompressible fluid through the pore clusters was simulated under a fixed pressure gradient, and steady-state velocity and pressure fields were calculated. Permeability was determined using Darcy's law.

For each generated structure, we computed four geometric characteristics: (i) critical cross-sectional area, (ii) effective porosity, (iii) integral mean curvature, and (iv) the Euler characteristic. Permeability showed power-law scaling with each of these four geometric measures. Although effective porosity (ϕ_0) did not strictly follow a power-law, we observed that the data points for all systems showed a scaling behavior with permeability. Interestingly, the exponent of the power-law scaling was nearly identical across both disordered and deterministic systems.

Inspired by Hadwiger's theorem, we formulated a combinatorial function F of these four geometric characteristics. The key finding of our research is that permeability exhibits a single scaling relationship with this combinatorial F across all systems, whether their pore geometries were ordered or disordered. The scaling exponent of 0.428 is universal for 3-dimensional porous systems made of spherical grains. To the best of our knowledge, this is the first time a unified relationship linking fluid flow to all four Minkowski functionals has been proposed,

with a consistent exponent for disordered 3D porous systems. We achieved a collapse of data points from all the systems studied through regression of the combinatorial function F .

Another noteworthy result is that the cubic and hexagonal systems set the upper and lower bounds for the scaling relations between permeability (k) and each geometric characteristic. The data for the stochastic systems fell between these bounds.

Our original goal of relating permeability to system characteristics through the four Minkowski functionals with a single exponent, regardless of particle size or distribution, suggests that the exponent is indeed universal. Future work will explore whether this exponent of 0.428 is independent of particle shape. We also intend to extend this study to other transport properties, such as electrical conductivity, and look forward to reporting on those findings soon.

Chapter 8

Summary and Future Directions

In this dissertation, I conducted a thorough investigation into the formation, evolution, and energetics of crack mosaics in various systems. I developed classification schemes based on topology and geometry and applied them to columnar joints, cyclic wetting-drying systems, and salt playas. Additionally, I examined how fractures form in porous granular systems under compressive loading using Distinct Element Methods and theoretical analysis to understand how the geometry and topology of these systems affect their flow properties. The key findings and contributions of this work are outlined as follows:

- **Geometrical and Topological Analysis of Crack Mosaics:**

The study introduces a robust framework for understanding crack mosaics through a four-parameter set (n, v, D, λ) . This compact signature captures both the topological and geometrical properties of crack mosaics, providing a clearer distinction between different crack systems than traditional topological combinatorial values (n, v) alone. This quantitative approach differentiates crack systems based on the mechanisms driving crack formation and the material properties. The identification of two topological regions, the ‘Platonic attractor’ and the ‘Voronoi attractor,’ deepens our understanding of how crack mosaics transition between different equilibrium states. This framework forms a foundation for future research into the evolution of crack patterns across a wide range of materials and systems.

- **Energy Minimization in Crack Mosaics and Pattern Formation:**

Building on this, I investigated the development of crack patterns in dynamic systems, including columnar joints and the cyclic wetting-drying of mud. Our simulations revealed that the hexagon-like tiling found in columnar joints is a result of the system’s natural drive to minimize total energy. Likewise, mud cracks evolve into Centroidal Voronoi tessellations through repeated wetting and drying cycles governed by energy minimization.

The system energy follows a power-law dependence on the isoperimetric ratio λ , with an exponent β ranging from 0.2 to 0.5. These results emphasize that the transformation of crack patterns from disordered T-junctions to Y-junctions follows predictable pathways dictated by the underlying physics of energy dissipation. By introducing a ‘Voronoi-ness’ measure based on the Hausdorff metric, I was able to quantitatively monitor this geometric evolution, showing that systems with lower elastic modulus and longer intervals between drying cycles tend to reach a mature Voronoi mosaic more efficiently.

- **Hexagon-like Ridge Patterns in Salt Playas:**

Next, I investigated the formation of hexagon-like patterns in salt playas. I used the concept that repeated wetting and drying causes the cracks to evolve toward a hexagon-like pattern as playas go under annual wetting–drying cycles. By modeling fluid transport and salinity profiles, the study establishes a relationship between salinity-driven crystallization and the emergence of Voronoi-like geometries. I also studied how ambient conditions, such as evaporation rate, salinity, and diffusion, influence crystal growth.

- **Crack Formation in Porous Granular Systems:**

I studied crack formation in porous granular systems under compressive strain, focusing on the role of material properties, particularly the elastic modulus of the cement bonding spherical grains, using DEM. Two scenarios were analyzed: varying bond stiffness while keeping bond strength constant and varying bond strength while maintaining constant stiffness. Both scenarios demonstrated a critical strain, ϵ_{knee} , at which the rate of micro-crack formation increased, with a power-law scaling relationship between ϵ_{knee} and the strain at which percolation occurred, ϵ_{perc} . This scaling was robust across different bond material properties, offering a predictive framework for determining the strain threshold before system-wide failure. These findings provide valuable insights into the progression of micro-cracks, potentially aiding in the early detection of damage in granular materials.

- **Permeability and Geometric Invariants in Porous Systems:**

The final focus of this dissertation was on fluid flow in porous systems, where I investigated the relationship between permeability and the geometric structure of the pore space. Motivated by Hadwiger’s theorem, I computed four Minkowski functionals – critical cross-sectional area, effective porosity, integral mean curvature, and the Euler characteristic – and found that permeability scales with these geometric invariants in both disordered and ordered systems. By introducing a combinatorial function F of these four characteristics, we discovered a universal scaling relationship between permeability and F , with a consistent exponent of 0.428 across all systems, regardless of their geometric order. This unified relationship underscores the geometric principles that govern fluid

transport in 3D porous systems, offering a predictive model for permeability based on geometric invariants.

In conclusion, this work advances the field by offering a unified approach to understanding the interplay between geometry, material properties, and physical processes in porous systems, providing a foundation for future studies in the physics of fracture, energy minimization, and fluid dynamics.

8.1 Future Directions

There are several potential avenues to extend and deepen the research presented in this dissertation:

1. **Machine Learning and Pattern Recognition:** The incorporation of machine learning techniques offers a promising future direction, particularly for the classification and prediction of fracture patterns based on physical and environmental inputs. Pattern recognition algorithms could be used to automatically identify specific fracture behaviors or transitions between pattern types (e.g., from Gilbert to Voronoi tessellation) in both simulated and experimental datasets.
2. **Extension of DEM to Other Granular Materials:** The current DEM model focused on spherical grains bonded by cement. Future work could explore systems with grains of irregular shapes or different size distributions (e.g., bimodal or fractal distributions), which could more accurately represent real-world materials like soils, rocks, and construction materials. Additionally, studying the effect of different particle geometries, such as ellipsoidal or polyhedral particles, could provide deeper insights into crack propagation mechanisms.
3. **Effect of Dynamic Loading:** While this study applied compressive stress in a quasi-static manner, future investigations could explore the effect of dynamic loading conditions, such as cyclic or impact loading. This would be particularly relevant for applications like earthquake engineering, where materials are subjected to rapidly changing stresses and could help better understand material failure under fatigue.
4. **Crack Healing Mechanisms:** It would be valuable to study crack healing mechanisms where micro-cracks may close under certain conditions, such as changes in temperature or chemical reactions at the particle bonds. This could inform the development of self-healing materials or better predict the lifespan of materials in civil engineering applications.

5. **Multiscale Modeling:** A multiscale approach, combining macro-scale and micro-scale models, would offer a more comprehensive understanding of how microstructural crack formation and bond strength influence the overall mechanical behavior of the system. Coupling the Distinct Element Method (DEM) with continuum mechanics methods like Finite Element Modeling (FEM) could be a promising avenue to achieve this.
6. **Extension to Different Particle Shapes:** While the fluid flow study focused on spherical grains, it remains to be seen whether the universal exponent of 0.428 holds for porous systems composed of non-spherical particles. Investigating different particle shapes, such as ellipsoids, cubes, or irregular geometries, would provide a broader understanding of the universality of the relationship between permeability and Minkowski functionals. One further improvement can be considering the particles intersecting at more than a point and using accurate expressions for the Minkowski functionals under these situations.
7. **Improving Computational Efficiency:** Enhancing the numerical methods used, such as optimizing the finite difference approach or implementing alternative computational techniques like finite element or lattice Boltzmann methods, could allow for more efficient simulations of larger or more complex systems.
8. **Study of Other Transport Properties:** Beyond fluid permeability, other transport properties like electrical conductivity, thermal conductivity, and diffusivity can be examined using similar methods. Exploring how these properties scale with the same set of geometric invariants could reveal unified scaling laws for different types of transport phenomena in porous media.
9. **Experimental Validation:** While our findings are based on simulations, experimental validation is crucial for assessing the practical applicability of the proposed scaling relations. Developing physical models or performing laboratory-based measurements on 3D-printed or naturally occurring porous systems would be valuable in confirming the robustness of the scaling exponent and the combinatorial function F .

References

- [1] Alan Arnold Griffith. The phenomena of rupture and flow in solids. *Philosophical transactions of the royal society of london. Series A, containing papers of a mathematical or physical character*, 221(582-593):163–198, 1921.
- [2] Christian André Andresen, Alex Hansen, Romain Le Goc, Philippe Davy, and Sigmund Mongstad Hope. Topology of fracture networks. *Frontiers in Physics*, 1:7, 2013.
- [3] François Boulogne, Ludovic Pauchard, Frédérique Giorgiutti-Dauphiné, Robert Botet, Ralf Schweins, Michael Sztucki, Joaquim Li, Bernard Cabane, and Lucas Goehring. Structural anisotropy of directionally dried colloids. *EPL (Europhysics Letters)*, 105(3):38005, 2014.
- [4] Yossi Cohen and Itamar Procaccia. Dynamics of cracks in torn thin sheets. *Physical Review E*, 81(6):066103, 2010.
- [5] Lucas Goehring, L Mahadevan, and Stephen W Morris. Nonequilibrium scale selection mechanism for columnar jointing. *Proceedings of the National Academy of Sciences*, 106(2):387–392, 2009.
- [6] Lucas Goehring, William J Clegg, and Alexander F Routh. Wavy cracks in drying colloidal films. *Soft Matter*, 7(18):7984–7987, 2011.
- [7] Lucas Goehring, Joaquim Li, and Pree-Cha Kiatkirakajorn. Drying paint: from micro-scale dynamics to mechanical instabilities. *Philosophical Transactions of the Royal Society A: Mathematical, Physical and Engineering Sciences*, 375(2093):20160161, 2017.
- [8] RV Gol'Dstein and RL Salganik. Brittle fracture of solids with arbitrary cracks. *International journal of Fracture*, 10(4):507–523, 1974.
- [9] O Huseby, J-F Thovert, and P M Adler. Geometry and topology of fracture systems. *Journal of Physics A: Mathematical and General*, 30(5):1415–1444, mar 1997.
- [10] George R Irwin. Analysis of stresses and strains near the end of a crack transversing a plate. *Trans. ASME, Ser. E, J. Appl. Mech.*, 24:361–364, 1957.
- [11] Jean Schmittbuhl, Stéphane Roux, Jean-Pierre Vilotte, and Knut Jorgen Måløy. Interfacial crack pinning: effect of nonlocal interactions. *Physical Review Letters*, 74(10):1787, 1995.

- [12] S. Sisavath, V. Mourzenko, P. Genthon, J.-F. Thovert, and P. M. Adler. Geometry, percolation and transport properties of fracture networks derived from line data. *Geophysical Journal International*, 157(2):917–934, 05 2004.
- [13] Tajkera Khatun, Moutushi Dutta Choudhury, Tapati Dutta, and Sujata Tarafdar. Electric-field-induced crack patterns: Experiments and simulation. *Phys. Rev. E*, 86:016114, Jul 2012.
- [14] Akio Nakahara and Yousuke Matsuo. Transition in the pattern of cracks resulting from memory effects in paste. *Physical Review E*, 74(4):045102, 2006.
- [15] Sudeshna Sircar, Sujata Tarafdar, and Tapati Dutta. Crack formation in desiccating laponite® films under ac field: Effect of varying frequency. *Applied Clay Science*, 156:69–76, 2018.
- [16] Mary Lou Zoback and Mark Zoback. State of stress in the conterminous united states. *Journal of Geophysical Research: Solid Earth*, 85(B11):6113–6156, 1980.
- [17] Mary Lou Zoback. First- and second-order patterns of stress in the lithosphere: The world stress map project. *Journal of Geophysical Research: Solid Earth*, 97(B8):11703–11728, 1992.
- [18] Agust Gudmundsson. *Extension fractures and shear fractures*, pages 233–254. Cambridge University Press, 2011.
- [19] Jon E. Olson. Sublinear scaling of fracture aperture versus length: An exception or the rule? *Journal of Geophysical Research: Solid Earth*, 108(B9), 2003.
- [20] Brian Berkowitz. Characterizing flow and transport in fractured geological media: A review. *Advances in Water Resources*, 25(8):861–884, 2002.
- [21] Shlomo P. Neuman. Trends, prospects and challenges in quantifying flow and transport through fractured rocks. *Hydrogeology Journal*, 13(1):124–147, 2005.
- [22] Lucas Goehring, Rebecca Conroy, Asad Akhter, William J. Clegg, and Alexander F. Routh. Evolution of mud-crack patterns during repeated drying cycles. *Soft Matter*, 6:3562–3567, 2010.
- [23] Yves Couder, Ludovic Pauchard, Catherine Allain, Mokhtar Adda-Bedia, and Stéphane Douady. The leaf venation as formed in a tensorial field. *The European Physical Journal B-Condensed Matter and Complex Systems*, 28(2):135–138, 2002.
- [24] Lucas Goehring, Akio Nakahara, Tapati Dutta, So Kitsunozaki, and Sujata Tarafdar. *Desiccation Cracks and their Patterns: Formation and Modelling in Science and Nature*. Statistical Physics of Fracture and Breakdown. Wiley-VCH, 2015.
- [25] Maria F Laguna, Steffen Bohn, and Eduardo A Jagla. The role of elastic stresses on leaf venation morphogenesis. *PLoS Comput Biol*, 4(4):e1000055, 2008.
- [26] Robert Osserman. The isoperimetric inequality. *Bulletin of the American Mathematical Society*, 84(6):11821238, 1978.

- [27] Ruhul A. I. Haque. Gilber tessellation. Available at https://archive.org/details/gilbert_mosaic, September 2024.
- [28] C. Bradford Barber, David P. Dobkin, and Hannu Huhdanpaa. The quickhull algorithm for convex hulls. *ACM Trans. Math. Softw.*, 22(4):469–483, 1996.
- [29] G. Bradski. The OpenCV Library. *Dr. Dobb's Journal of Software Tools*, 2000.
- [30] Gábor Domokos, Douglas J Jerolmack, Ferenc Kun, and János Török. Plato's cube and the natural geometry of fragmentation. *Proceedings of the National Academy of Sciences*, 117(31):18178–18185, 2020.
- [31] A. Roy, R. A. I. Haque, A. J. Mitra, S. Tarafdar, and T. Dutta. Combinatorial topology and geometry of fracture networks. *Phys. Rev. E*, 105:034801, Mar 2022.
- [32] Arthur Holmes. *Principles of Physical Geology*. Number 1 – 3. Wiley, New York, 3rd edition, 1978.
- [33] Gerhard Müller. Starch columns: Analog model for basalt columns. *Journal of Geophysical Research: Solid Earth*, 103(B7):15239–15253, 1998.
- [34] G. Gauthier, V. Lazarus, and L. Pauchard. Shrinkage star-shaped cracks: Explaining the transition from 90 degrees to 120 degrees. *EPL (Europhysics Letters)*, 89(2):26002, jan 2010.
- [35] Lucas Goehring. Evolving fracture patterns: columnar joints, mud cracks and polygonal terrain. *Philosophical Transactions of the Royal Society A: Mathematical, Physical and Engineering Sciences*, 371(2004):20120353, 2013.
- [36] Zdeněk P. Bažant, L. Cedolin, and Zdeněk P. Bazant. *Stability of Structures: Elastic, Inelastic, Fracture and Damage Theories*. Oxford University Press, 1991.
- [37] Paul Budkewitsch and Pierre-Yves Robin. Modelling the evolution of columnar joints. *Journal of Volcanology and Geothermal Research*, 59(3):219–239, 1994.
- [38] E. A. Jagla and A. G. Rojo. Sequential fragmentation: The origin of columnar quasi-hexagonal patterns. *Phys. Rev. E*, 65:026203, Jan 2002.
- [39] hide S. Columnar joint in tsumekisaki izu. via Wikimedia. Available at https://commons.wikimedia.org/wiki/File:Columnar_joint_In_Tsumekisaki_Izu_-_panoramio.jpg, January 2011.
- [40] Martin Hofmann, Hans-Achim Bahr, Hans-Jürgen Weiss, Ute Bahr, and Herbert Balke. Spacing of crack patterns driven by steady-state cooling or drying and influenced by a solidification boundary. *Physical Review E*, 83(3):036104, 2011.
- [41] Martin Hofmann, Robert Anderssohn, Hans-Achim Bahr, Hans-Jürgen Weiß, and Jens Nellesen. Why hexagonal basalt columns? *Phys. Rev. Lett.*, 115:154301, Oct 2015.
- [42] Michael P Ryan and Charles G Sammis. Cyclic fracture mechanisms in cooling basalt. *Geological Society of America Bulletin*, 89(9):1295–1308, 1978.

- [43] James M DeGraff and Atilla Aydin. Surface morphology of columnar joints and its significance to mechanics and direction of joint growth. *Geological Society of America Bulletin*, 99(5):605–617, 1987.
- [44] Harry C Hardee. Solidification in kilauea iki lava lake. *Journal of Volcanology and Geothermal Research*, 7(3-4):211–223, 1980.
- [45] Ruhul A. I. Haque. Simulation of crack evolution in columnar joints. Available at https://archive.org/details/columnar_joints_crack_evolution, September 2024.
- [46] T. C. Hales. The honeycomb conjecture. *Discrete & Computational Geometry*, 25(1):1–22, 2001.
- [47] Denis L Weaire and Stefan Hutzler. *The physics of foams*. Oxford University Press, 1999.
- [48] Qiang Du, Vance Faber, and Max Gunzburger. Centroidal voronoi tessellations: Applications and algorithms. *SIAM review*, 41(4):637–676, 1999.
- [49] John Snow. *On the mode of communication of cholera*. John Churchill, 2nd edition, 1855.
- [50] Hisao Honda. *Geometrical Models for Cells in Tissues*, volume 81 of *International Review of Cytology*. Academic Press, 1983.
- [51] D. Weaire and N. Rivier. Soap, cells and statistics—random patterns in two dimensions. *Contemporary Physics*, 25(1):59–99, 1984.
- [52] Takashi Hayashi and Richard W. Carthew. Surface mechanics mediate pattern formation in the developing retina. *Nature*, 431(7009):647–652, 2004.
- [53] Barry J Thompson. From genes to shape during metamorphosis: a history. *Current Opinion in Insect Science*, 43:1–10, 2021. Insect genomics * Development and regulation.
- [54] Valentina Perricone, Tobias B. Grun, Francesco Rendina, Francesco Marmo, Maria Daniela Candia Carnevali, Michal Kowalewski, Angelo Facchini, Mario De Stefano, Luigia Santella, Carla Langella, and Alessandra Micheletti. Hexagonal voronoi pattern detected in the microstructural design of the echinoid skeleton. *Journal of The Royal Society Interface*, 19(193):20220226, 2022.
- [55] Soheil Sanipour, Navid Bahrani, and Andrew Corkum. Simulation of brittle failure around canada’s mine-by experiment tunnel using 2d continuum-based voronoi tessellated models. *Rock Mechanics and Rock Engineering*, 55(10):6387–6408, 2022.
- [56] Neeraj Yadav, Julian H. Kang, Zofia K. Rybkowski, Matthew T. Yarnold, and Weiling He. Stress-weighted centroidal voronoi tessellation for structural design. *Finite Elements in Analysis and Design*, 216:103905, 2023.
- [57] James M. Degraff, Philip E. Long, and Atilla Aydin. Use of joint-growth directions and rock textures to infer thermal regimes during solidification of basaltic lava flows. *Journal of Volcanology and Geothermal Research*, 38(3):309–324, 1989.

- [58] Atilla Aydin and James M. DeGraff. Evolution of polygonal fracture patterns in lava flows. *Science*, 239(4839):471–476, 1988.
- [59] Lucas Goehring and Stephen W. Morris. Scaling of columnar joints in basalt. *Journal of Geophysical Research: Solid Earth*, 113(B10), 2008.
- [60] R. S. Sletten, B. Hallet, and R. C. Fletcher. Resurfacing time of terrestrial surfaces by the formation and maturation of polygonal patterned ground. *Journal of Geophysical Research: Planets*, 108(E4), 2003.
- [61] Ruhul A. I. Haque, Anamika Roy, Atish J. Mitra, Sujata Tarafdar, and Tapati Dutta. Evolution of tiling-like crack patterns in maturing columnar joints. *Langmuir*, 38(22):7035–7045, 2022. PMID: 35612996.
- [62] Rudolf Karch, Friederike Neumann, Martin Neumann, Paul Szawlowski, and Wolfgang Schreiner. Voronoi polyhedra analysis of optimized arterial tree models. *Annals of Biomedical Engineering*, 31(5):548–563, 2003.
- [63] Adam Runions, Martin Fuhrer, Brendan Lane, Pavol Federl, Anne-Gaëlle Rolland-Lagan, and Przemyslaw Prusinkiewicz. Modeling and visualization of leaf venation patterns. In *ACM SIGGRAPH 2005 Papers*, SIGGRAPH '05, pages 702–711, New York, NY, USA, 2005. Association for Computing Machinery.
- [64] Taehyong Kim, Murali Ramanathan, and Aidong Zhang. A graph-based approach for computational model of bone microstructure. In *Proceedings of the First ACM International Conference on Bioinformatics and Computational Biology*, BCB '10, pages 563–568, New York, NY, USA, 2010. Association for Computing Machinery.
- [65] Sara Kaliman, Christina Jayachandran, Florian Rehfeldt, and Ana-Sunčana Smith. Limits of applicability of the voronoi tessellation determined by centers of cell nuclei to epithelium morphology. *Frontiers in Physiology*, 7, 2016.
- [66] Robert I. Saye and James A. Sethian. The voronoi implicit interface method for computing multiphase physics. *Proceedings of the National Academy of Sciences*, 108(49):19498–19503, 2011.
- [67] T. Wejrzanowski, J. Skibinski, J. Szumbariski, and K.J. Kurzydowski. Structure of foams modeled by laguerre–voronoi tessellations. *Computational Materials Science*, 67:216–221, 2013.
- [68] Simone Falco, Jiawei Jiang, Francesco De Cola, and Nik Petrinic. Generation of 3d polycrystalline microstructures with a conditioned laguerre-voronoi tessellation technique. *Computational Materials Science*, 136:20–28, 2017.
- [69] Giulia Angelucci and Fabrizio Mollaioli. Voronoi-like grid systems for tall buildings. *Frontiers in Built Environment*, 4, 2018.
- [70] KS Krishnamurthy, K Kandiannan, V Srinivasan, R Dinesh, SJ Ankegowda, CK Thankamani, Nirmal Babu, and KV Peter. Climate change impact and water productivity in black pepper and cardamom. *International Journal of Innovative Horticulture*, 9(1):1–8, 2020.

- [71] Mokwon Lee, Qing Fang, Youngsong Cho, Joonghyun Ryu, Ligang Liu, and Deok-Soo Kim. Support-free hollowing for 3d printing via voronoi diagram of ellipses. *Computer-Aided Design*, 101:23–36, 2018.
- [72] Jonàs Martínez, Samuel Hornus, Haichuan Song, and Sylvain Lefebvre. Polyhedral voronoi diagrams for additive manufacturing. *ACM Trans. Graph.*, 37(4), jul 2018.
- [73] Tao Liu, Sofiane Guessasma, Jihong Zhu, and Weihong Zhang. Designing cellular structures for additive manufacturing using voronoi–monte carlo approach. *Polymers*, 11(7), 2019.
- [74] B. Boots, K. Sugihara, S.N. Chiu, and A. Okabe. *Spatial Tessellations: Concepts and Applications of Voronoi Diagrams*. Wiley Series in Probability and Statistics. Wiley, 2009.
- [75] Jana Lasser, Joanna M. Nield, Marcel Ernst, Volker Karius, Giles F. S. Wiggs, Matthew R. Threadgold, Cédric Beaume, and Lucas Goehring. Salt polygons and porous media convection. *Phys. Rev. X*, 13:011025, Feb 2023.
- [76] Gerhard Müller. Experimental simulation of basalt columns. *Journal of Volcanology and Geothermal Research*, 86(1):93–96, 1998.
- [77] Supti Sadhukhan, Tapati Dutta, and Sujata Tarafdar. Crack formation in composites through a spring model. *Physica A: Statistical Mechanics and its Applications*, 390(4):731–740, 2011.
- [78] F. Giorgiutti-Dauphiné and L. Pauchard. Drying drops. *The European Physical Journal E*, 41(3):32, 2018.
- [79] S Bohn, L Pauchard, and Y Couder. Hierarchical crack pattern as formed by successive domain divisions. *Physical Review E*, 71(4):046214, 2005.
- [80] EN Gilbert and B Noble. Surface films of needle-shaped crystals. *Applications of undergraduate mathematics in engineering*, pages 329–346, 1967.
- [81] J. E. Bolander and N. Sukumar. Irregular lattice model for quasistatic crack propagation. *Phys. Rev. B*, 71:094106, Mar 2005.
- [82] So Kitsunozaki. Cracking condition of cohesionless porous materials in drying processes. *Phys. Rev. E*, 87:052805, May 2013.
- [83] Sujata Tarafdar and Tapati Dutta. Formation of desiccation crack patterns in electric fields: a review. *Philos. Trans. R. Soc., A*, 377(2136):20170398, 2019.
- [84] Supti Sadhukhan, Ankush Kumar, Giridhar U. Kulkarni, Sujata Tarafdar, and Tapati Dutta. A spring network simulation in three dimensions for designing optimal crack pattern template to fabricate transparent conducting electrodes. *Bulletin of Materials Science*, 42(5):197, 2019.
- [85] Supti Sadhukhan, Shashwati Roy Majumder, Dibyendu Mal, Tapati Dutta, and Sujata Tarafdar. Desiccation cracks on different substrates: simulation by a spring network model. *J. Phys.: Condens. Matter*, 19(35):356206, aug 2007.

- [86] Ruhul A. I. Haque. Evolution of mud cracks due repeated wetting and drying. Available at https://archive.org/details/mud_crack_evolution, September 2024.
- [87] V. Senthil Kumar and V. Kumaran. Voronoi cell volume distribution and configurational entropy of hard-spheres. *The Journal of Chemical Physics*, 123(11):114501, 09 2005.
- [88] Marc Barthélemy. Spatial networks. *Physics Reports*, 499(1):1–101, 2011.
- [89] A. V. Limaye, R. D. Narhe, A. M. Dhote, and S. B. Ogale. Evidence for convective effects in breath figure formation on volatile fluid surfaces. *Phys. Rev. Lett.*, 76:3762–3765, May 1996.
- [90] Irina Legchenkova, Mark Frenkel, Nir Shvalb, Shraga Shoval, Oleg V. Gendelman, and Edward Bormashenko. From chaos to ordering: New studies in the shannon entropy of 2d patterns. *Entropy*, 24(6), 2022.
- [91] S.N. Chiu. Aboav-weaire’s and lewis’ laws—a review. *Materials Characterization*, 34(2):149–165, 1995.
- [92] J. Saraiva, P. Pina, L. Bandeira, and J. Antunes. Polygonal networks on the surface of mars; applicability of lewis, desch and aboav–weaire laws. *Philosophical Magazine Letters*, 89(3):185–193, 2009.
- [93] A. Steyer, P. Guenoun, D. Beysens, and C. M. Knobler. Two-dimensional ordering during droplet growth on a liquid surface. *Phys. Rev. B*, 42:1086–1089, Jul 1990.
- [94] D.A Aboav. The arrangement of grains in a polycrystal. *Metallography*, 3(4):383–390, 1970.
- [95] D Weaire. Some remarks on the arrangement of grains in a polycrystal. *Metallography*, 7(2):157–160, 1974.
- [96] J. C. M. Mombach, Rita M. C. de Almeida, and J. R. Iglesias. Mitosis and growth in biological tissues. *Phys. Rev. E*, 48:598–602, Jul 1993.
- [97] Athol D. Abrahams Anthony J. Parsons, Athol D. Editors Anthony J. Parsons. *Geomorphology of Desert Environments*. Springer Dordrecht, 2 edition, 2009.
- [98] Tim K. Lowenstein and Lawrence A. Hardie. Criteria for the recognition of salt-pan evaporites. *Sedimentology*, 32(5):627–644, 1985.
- [99] D Krinsley. A geomorphological and paleoclimatological study of the playas of iran. *US Geol. Surv. Rep.*, 1970.
- [100] Lawrence A. Hardie, Joseph P. Smoot, and Hans P. Eugster. *Saline Lakes and their Deposits: A Sedimentological Approach*, pages 7–41. John Wiley & Sons, Ltd, 1978.
- [101] S.L. Rettig, B.F. Jones, and F. Risacher. Geochemical evolution of brines in the salar of uyuni, bolivia. *Chem. Geol.*, 30(1):57–79, 1980.
- [102] Wayne A. Wurtsbaugh, Craig Miller, Sarah E. Null, R. Justin DeRose, Peter Wilcock, Maura Hahnenberger, Frank Howe, and Johnnie Moore. Decline of the world’s saline lakes. *Nat. Geosci.*, 10(11):816–821, 2017.

- [103] F. W. Christiansen. Polygonal fracture and fold systems in the salt crust, great salt lake desert, utah. *Science*, 139(3555):607–609, 1963.
- [104] Joanna M. Nield, Robert G. Bryant, Giles F.S. Wiggs, James King, David S.G. Thomas, Frank D. Eckardt, and Richard Washington. The dynamism of salt crust patterns on playas. *Geology*, 43(1):31–34, 01 2015.
- [105] R. A. Wooding. Rayleigh instability of a thermal boundary layer in flow through a porous medium. *J. Fluid Mech.*, 9(2):183–192, 1960.
- [106] George M. Homsy and Albert E. Sherwood. Convective instabilities in porous media with through flow. *AIChE J.*, 22(1):168–174, 1976.
- [107] R. A. Wooding, Scott W. Tyler, Ian White, and P. A. Anderson. Convection in groundwater below an evaporating salt lake: 2. evolution of fingers or plumes. *Water Resour. Res.*, 33(6):1219–1228, 1997.
- [108] Robin A. Wooding. Variable-density saturated flow with modified darcy’s law: The salt lake problem and circulation. *Water Resour. Res.*, 43(2), 2007.
- [109] Remke L. Van Dam, Craig T. Simmons, David W. Hyndman, and Warren W. Wood. Natural free convection in porous media: First field documentation in groundwater. *Geophys. Res. Lett.*, 36(11), 2009.
- [110] Joel D. Stevens, John M. Sharp, Craig T. Simmons, and T.R. Fenstemaker. Evidence of free convection in groundwater: Field-based measurements beneath wind-tidal flats. *J. Hydrol.*, 375(3):394–409, 2009.
- [111] Anouchka Unel. This is the salar of uyuni, in bolivia. via Wikimedia Commons. Available at https://commons.wikimedia.org/wiki/File:Salar_Uyuni_au01.jpg, November 2004.
- [112] Ruhul A. I. Haque, Atish J. Mitra, Sujata Tarafdar, and Tapati Dutta. Evolution of polygonal crack patterns in mud when subjected to repeated wetting–drying cycles. *Chaos, Solitons Fractals*, 174:113894, 2023.
- [113] Khalid Aziz and Antonin Settari. *Petroleum reservoir simulation*. Springer Netherlands, 1979.
- [114] Sudipta Sarkar, M Nafi Toksoz, and Daniel R Burns. Fluid flow modeling in fractures. Technical report, Massachusetts Institute of Technology. Earth Resources Laboratory, 2004.
- [115] S Sadhukhan and T Dutta. Existence of convective threshold and its role on temperature in reactive flow through fractured rocks: a simulation study in 2d. *J. Phys. Commun.*, 2(4):045033, apr 2018.
- [116] Moutushi Dutta Choudhury, Tapati Dutta, and Sujata Tarafdar. Growth kinetics of nacl crystals in a drying drop of gelatin: transition from faceted to dendritic growth. *Soft Matter*, 11:6938–6947, 2015.
- [117] Kent Brooks. Lithium minerals. *Geology Today*, 36(5):192–197, 2020.

- [118] Ruhul A. I. Haque. Simulation of ridge patterns in salt playa. Available at https://archive.org/details/salt_playa_crystal_growth, September 2024.
- [119] E. R. Lapwood. Convection of a fluid in a porous medium. *Math. Proc. Cambridge Philos. Soc.*, 44(4):508–521, 1948.
- [120] Donald A. Nield. Onset of thermohaline convection in a porous medium. *Water Resour. Res.*, 4:553–560, 1968.
- [121] Huang Qi, Teh-Lung Ku, and Fred M. Phillips. Evolutionary characteristics of lakes and palaeoclimatic undulation in the qaidam basin, china. *Chin. J. Oceanol. Limnol.*, 11(1):34–45, 1993.
- [122] Kai Wang, Yu Zhang, Jiahuan Han, Lichun Ma, Mianping Zheng, Yue Wu, and Banwang Yang. Distribution and genesis of potassium-bearing minerals in lop nor playa, xinjiang, china. *Minerals*, 13(4), 2023.
- [123] Soumyajyoti Biswas, Purusattam Ray, and Bikas K Chakrabarti. *Statistical physics of fracture, breakdown, and earthquake: effects of disorder and heterogeneity*. John Wiley & Sons, 2015.
- [124] JC Jaeger and NGW Cook. *Fundamentals of rock mechanics*. Chapman & Hall, 2 edition, 1976.
- [125] Srutarshi Pradhan, Alex Hansen, and Bikas K. Chakrabarti. Failure processes in elastic fiber bundles. *Rev. Mod. Phys.*, 82:499–555, Mar 2010.
- [126] G. Timár, J. Blömer, F. Kun, and H. J. Herrmann. New universality class for the fragmentation of plastic materials. *Phys. Rev. Lett.*, 104:095502, Mar 2010.
- [127] Elisabeth Bouchaud, Dominique Jeulin, Claude Prioul, and Stéphane Roux. *Physical Aspects of Fracture*. Kluwer Academic Publishers, New York, 1 edition, 2001.
- [128] C.D. Martini, R.S. Read, and J.B. Martino. Observations of brittle failure around a circular test tunnel. *International Journal of Rock Mechanics and Mining Sciences*, 34(7):1065–1073, 1997.
- [129] E. Eberhardt, D. Stead, B. Stimpson, and R.S. Read. Changes in acoustic event properties with progressive fracture damage. *International Journal of Rock Mechanics and Mining Sciences*, 34(3):71.e1–71.e12, 1997.
- [130] D. A. Lockner, J. D. Byerlee, V. Kuksenko, A. Ponomarev, and A. Sidorin. Quasi-static fault growth and shear fracture energy in granite. *Nature*, 350(6313):39–42, 1991.
- [131] Philip M Benson, Sergio Vinciguerra, Philip G Meredith, and R Paul Young. Laboratory simulation of volcano seismicity. *Science*, 322(5899):249–252, 2008.
- [132] PK Kaiser and B-H Kim. Rock mechanics challenges in underground construction and mining. In Y Potvin, J Carter, A Dyskin, and R Jeffrey, editors, *SHIRMS 2008: Proceedings of the First Southern Hemisphere International Rock Mechanics Symposium*, pages 23–38. Australian Centre for Geomechanics, 2008.

- [133] Mervyn S Paterson and Teng-fong Wong. *Experimental rock deformation: the brittle field*, volume 348. Springer, 2005.
- [134] Hans J Herrmann and Stéphane Roux. *Statistical models for the fracture of disordered media*. Elsevier, 2014.
- [135] F. Tzschichholz and H. J. Herrmann. Simulations of pressure fluctuations and acoustic emission in hydraulic fracturing. *Phys. Rev. E*, 51:1961–1970, Mar 1995.
- [136] Stefano Zapperi, Purusattam Ray, H. Eugene Stanley, and Alessandro Vespignani. First-order transition in the breakdown of disordered media. *Phys. Rev. Lett.*, 78:1408–1411, Feb 1997.
- [137] Guido Caldarelli, Francesco D. Di Tolla, and Alberto Petri. Self-organization and annealed disorder in a fracturing process. *Phys. Rev. Lett.*, 77:2503–2506, Sep 1996.
- [138] A Hansen and P C Hemmer. Criticality in fracture: the burst distribution. Technical report, Trondheim TU. Inst. Phys., Trondheim, 1994.
- [139] A. Garcimartín, A. Guarino, L. Bellon, and S. Ciliberto. Statistical properties of fracture precursors. *Phys. Rev. Lett.*, 79:3202–3205, Oct 1997.
- [140] C. Maes, A. Van Moffaert, H. Frederix, and H. Strauven. Criticality in creep experiments on cellular glass. *Phys. Rev. B*, 57:4987–4990, Mar 1998.
- [141] P. Diodati, F. Marchesoni, and S. Piazza. Acoustic emission from volcanic rocks: An example of self-organized criticality. *Phys. Rev. Lett.*, 67:2239–2243, Oct 1991.
- [142] Beno Gutenberg. The energy of earthquakes. *Quarterly Journal of the Geological Society of London*, 112(1-4):1–14, 1956.
- [143] Jordi Baró and Jörn Davidsen. Universal avalanche statistics and triggering close to failure in a mean-field model of rheological fracture. *Phys. Rev. E*, 97:033002, Mar 2018.
- [144] Diksha, Sumanta Kundu, Bikas K. Chakrabarti, and Soumyajyoti Biswas. Inequality of avalanche sizes in models of fracture. *Phys. Rev. E*, 108:014103, Jul 2023.
- [145] Lucilla de Arcangelis, S Redner, and HJ Herrmann. A random fuse model for breaking processes. *Journal de Physique Lettres*, 46(13):585–590, 1985.
- [146] B. Kahng, G. G. Batrouni, S. Redner, L. de Arcangelis, and H. J. Herrmann. Electrical breakdown in a fuse network with random, continuously distributed breaking strengths. *Phys. Rev. B*, 37:7625–7637, May 1988.
- [147] P. Ray and G. Date. Spatial scaling in fracture propagation in dilute systems. *Physica A: Statistical Mechanics and its Applications*, 229(1):26–35, 1996.
- [148] A. Lisjak and G. Grasselli. A review of discrete modeling techniques for fracturing processes in discontinuous rock masses. *Journal of Rock Mechanics and Geotechnical Engineering*, 6(4):301–314, 2014.

- [149] D.O. Potyondy and P.A. Cundall. A bonded-particle model for rock. *International Journal of Rock Mechanics and Mining Sciences*, 41(8):1329–1364, 2004. Rock Mechanics Results from the Underground Research Laboratory, Canada.
- [150] Narendra Kumar Bodaballa, Soumyajyoti Biswas, and Parongama Sen. Avalanche shapes in the fiber bundle model. *Phys. Rev. E*, 110:014129, Jul 2024.
- [151] Ferenc Kun and Hans J. Herrmann. Transition from damage to fragmentation in collision of solids. *Phys. Rev. E*, 59:2623–2632, Mar 1999.
- [152] Ferenc Kun, Imre Varga, Sabine Lennartz-Sassinek, and Ian G. Main. Rupture cascades in a discrete element model of a porous sedimentary rock. *Phys. Rev. Lett.*, 112:065501, Feb 2014.
- [153] Ruhul A. I. Haque. Compressive strain driven fracture in granular porous media. Available at https://archive.org/details/compressive_loading, September 2024.
- [154] Roland Lenormand and Cesar Zircon. Capillary fingering: Percolation and fractal dimension. *Transport in Porous Media*, 4(6):599–612, 1989.
- [155] Philip Geoffrey Saffman and Geoffrey Ingram Taylor. The penetration of a fluid into a porous medium or hele-shaw cell containing a more viscous liquid. *Proceedings of the Royal Society of London. Series A. Mathematical and Physical Sciences*, 245(1242):312–329, 1958.
- [156] Francis AL Dullien. *Porous media: fluid transport and pore structure*. Academic press, 2012.
- [157] Jacob Bear. *Introduction to modeling of transport phenomena in porous media*, volume 4. Springer Science & Business Media, 2012.
- [158] M.C. Leverett. Capillary Behavior in Porous Solids. *Transactions of the AIME*, 142(01):152–169, 12 1941.
- [159] M. Th. van Genuchten. A closed-form equation for predicting the hydraulic conductivity of unsaturated soils. *Soil Science Society of America Journal*, 44(5):892–898, 1980.
- [160] Christian Scholz, Frank Wirner, Jan Götz, Ulrich Ruede, Gerd E. Schröder-Turk, Klaus Mecke, and Clemens Bechinger. Permeability of porous materials determined from the euler characteristic. *Phys. Rev. Lett.*, 109:264504, Dec 2012.
- [161] A. J. Katz and A. H. Thompson. Quantitative prediction of permeability in porous rock. *Phys. Rev. B*, 34:8179–8181, Dec 1986.
- [162] Scott Kirkpatrick. Percolation and conduction. *Rev. Mod. Phys.*, 45:574–588, Oct 1973.
- [163] B. I. Halperin, Shechao Feng, and P. N. Sen. Differences between lattice and continuum percolation transport exponents. *Phys. Rev. Lett.*, 54:2391–2394, Jun 1985.
- [164] Jan Tobochnik, David Laing, and Gary Wilson. Random-walk calculation of conductivity in continuum percolation. *Phys. Rev. A*, 41:3052–3058, Mar 1990.

- [165] P. N. Sen, J. N. Roberts, and B. I. Halperin. Nonuniversal critical exponents for transport in percolating systems with a distribution of bond strengths. *Phys. Rev. B*, 32:3306–3308, Sep 1985.
- [166] Armin Bunde, Harald Harder, and Shlomo Havlin. Nonuniversality of diffusion exponents in percolation systems. *Phys. Rev. B*, 34:3540–3542, Sep 1986.
- [167] M. Octavio, A. Octavio, J. Aponte, R. Medina, and C. J. Lobb. Nonuniversal critical behavior in the critical current of superconducting composites. *Phys. Rev. B*, 37:9292–9297, Jun 1988.
- [168] V. Joekar-Niasar, F. Doster, R. T. Armstrong, D. Wildenschild, and M. A. Celia. Trapping and hysteresis in two-phase flow in porous media: A pore-network study. *Water Resources Research*, 49(7):4244–4256, 2013.
- [169] Steffen Berg, Holger Ott, Stephan A. Klapp, Alex Schwing, Rob Neiteler, Niels Brussee, Axel Makurat, Leon Leu, Frieder Enzmann, Jens-Oliver Schwarz, Michael Kersten, Sarah Irvine, and Marco Stampanoni. Real-time 3d imaging of haines jumps in porous media flow. *Proceedings of the National Academy of Sciences*, 110(10):3755–3759, 2013.
- [170] Martin J. Blunt, Branko Bijeljic, Hu Dong, Oussama Gharbi, Stefan Iglauer, Peyman Mostaghimi, Adriana Paluszny, and Christopher Pentland. Pore-scale imaging and modelling. *Advances in Water Resources*, 51:197–216, 2013. 35th Year Anniversary Issue.
- [171] M. Rücker, S. Berg, R. T. Armstrong, A. Georgiadis, H. Ott, A. Schwing, R. Neiteler, N. Brussee, A. Makurat, L. Leu, M. Wolf, F. Khan, F. Enzmann, and M. Kersten. From connected pathway flow to ganglion dynamics. *Geophysical Research Letters*, 42(10):3888–3894, 2015.
- [172] Rudolf J. Held and Michael A. Celia. Modeling support of functional relationships between capillary pressure, saturation, interfacial area and common lines. *Advances in Water Resources*, 24(3):325–343, 2001. Pore Scale Modeling.
- [173] H.-J. Vogel, U. Weller, and S. Schlüter. Quantification of soil structure based on minkowski functions. *Computers & Geosciences*, 36(10):1236–1245, 2010.
- [174] R. Hilfer. Review on scale dependent characterization of the microstructure of porous media. *Transport in Porous Media*, 46(2):373–390, 2002.
- [175] C.H. Arns, M.A. Knackstedt, and K. Mecke. 3d structural analysis: sensitivity of minkowski functionals. *Journal of Microscopy*, 240(3):181–196, 2010.
- [176] Steffen Schlüter and Hans-Jörg Vogel. On the reconstruction of structural and functional properties in random heterogeneous media. *Advances in Water Resources*, 34(2):314–325, 2011.
- [177] P. Lehmann, M. Berchtold, B. Ahrenholz, J. Tölke, A. Kaestner, M. Krafczyk, H. Flüher, and H.R. Künsch. Impact of geometrical properties on permeability and fluid phase distribution in porous media. *Advances in Water Resources*, 31(9):1188–1204, 2008. Quantitative links between porous media structures and flow behavior across scales.

- [178] G E Schröder-Turk, W Mickel, S C Kapfer, F M Schaller, B Breidenbach, D Hug, and K Mecke. Minkowski tensors of anisotropic spatial structure. *New Journal of Physics*, 15(8):083028, aug 2013.
- [179] Ryan T. Armstrong, James E. McClure, Vanessa Robins, Zhishang Liu, Christoph H. Arns, Steffen Schlüter, and Steffen Berg. Porous media characterization using minkowski functionals: Theories, applications and future directions. *Transport in Porous Media*, 130(1):305–335, 2019.
- [180] Prakash Purswani, Miral S. Tawfik, Zuleima T. Karpyn, and Russell T. Johns. On the development of a relative permeability equation of state. *Computational Geosciences*, 24(2):807–818, 2020.
- [181] Per Arne Slotte, Carl Fredrik Berg, and Hamid Hosseinzade Khanamiri. Predicting resistivity and permeability of porous media using minkowski functionals. *Transport in Porous Media*, 131(2):705–722, 2020.
- [182] James E. McClure, Thomas Ramstad, Zhe Li, Ryan T. Armstrong, and Steffen Berg. Modeling geometric state for fluids in porous media: Evolution of the euler characteristic. *Transport in Porous Media*, 133(2):229–250, 2020.
- [183] Herbert Federer. Curvature measures. *Transactions of the American Mathematical Society*, 93(3):418–491, 1959.
- [184] Hugo Hadwiger. *Vorlesungen über inhalt, oberfläche und isoperimetrie*, volume 93. Springer-Verlag, 2013.
- [185] A. R. DEXTER and D. W. TANNER. Packing densities of mixtures of spheres with log-normal size distributions. *Nature Physical Science*, 238(80):31–32, 1972.
- [186] Hans-Jörg Vogel. *Topological Characterization of Porous Media*, pages 75–92. Springer Berlin Heidelberg, Berlin, Heidelberg, 2002.
- [187] J. Hoshen and R. Kopelman. Percolation and cluster distribution. i. cluster multiple labeling technique and critical concentration algorithm. *Phys. Rev. B*, 14:3438–3445, Oct 1976.
- [188] Abhra Giri, Sujata Tarafdar, Philippe Gouze, and Tapati Dutta. Fractal geometry of sedimentary rocks: simulation in 3-D using a Relaxed Bidisperse Ballistic Deposition Model. *Geophysical Journal International*, 192(3):1059–1069, 12 2012.
- [189] Antonio Costa. Permeability-porosity relationship: A reexamination of the kozeny-carman equation based on a fractal pore-space geometry assumption. *Geophysical Research Letters*, 33(2), 2006.
- [190] P. Coussot. Scaling approach of the convective drying of a porous medium. *The European Physical Journal B - Condensed Matter and Complex Systems*, 15(3):557–566, 2000.

Appendix A

Spring model and elasticity

When a solid deforms, the atoms at various positions shift and oscillate around their equilibrium positions to minimize the potential energy. The total energy of the system can be expressed as a function of all atom positions, expanded around the equilibrium position of each displaced atom, as follows:

$$\phi(u_{ni}) = \phi(u_0) + \frac{1}{2} \sum_{mi} \frac{\partial^2 \phi}{\partial u_{mi} \partial u_{nj}} u_{mi} u_{nj} + \dots \quad (\text{A.1})$$

In the expansion of the energy function around the equilibrium position, the linear term in u_{mi} vanishes because the expansion is centered at the minimum energy state. Here, u_0 represents the equilibrium energy, and (m, n, \dots) denote the atomic positions, with i representing any of the three spatial directions. For long-wavelength vibrations, the displacements between neighboring atoms are approximately equal, allowing us to describe the deformation of the solid using continuum theory. In this model, each atom is connected to its neighbors via Hookean springs with a spring constant k . Although this model is not entirely accurate for representing shear deformations, it is adequate for analyzing longitudinal strain situations.

For a linear chain of atoms, the equation of motion becomes

$$M\ddot{u}_n = k(u_{n+1} - u_n) - k(u_n - u_{n-1}) \quad (\text{A.2})$$

For small displacements u of atoms at position n relative to their nearest neighbors at positions $(n+1)$ and $(n-1)$, with a constant separation distance a , the differences can be approximated by the differential quotients as follows:

$$(u_{n+1} - u_n) - (u_n - u_{n-1}) = a^2 \frac{\partial^2 u}{\partial x^2} \quad (\text{A.3})$$

where $i = x$.

The derivative

$$\varepsilon_{11} = \frac{\partial u_1}{\partial x_1} \quad (\text{A.4})$$

is the strain which is a continuum quantity. If the atomic masses are replaced by their mass density $\rho = M/a^3$, the continuum equation of motion for longitudinal vibration becomes from Eqs. A.7 and A.3,

$$\rho \ddot{u} = c_{11} \frac{\partial^2 u}{\partial x^2} \quad (\text{A.5})$$

with $c_{11} = \frac{k}{a}$. c_{11} is an elastic modulus that describes a force per unit area in the x-direction in response to a deformation along the same axis. The elastic energy becomes

$$E = \frac{1}{2} c_{11} \varepsilon_{11}^2 \quad (\text{A.6})$$

The derivative

$$\varepsilon_{11} = \frac{\partial u_1}{\partial x_1} \quad (\text{A.7})$$

represents the strain, which is a continuum quantity. When replacing the atomic masses with their mass density $\rho = \frac{M}{a^3}$, the continuum equation of motion for longitudinal vibration, derived from Eqs. A.7 and A.3, becomes

$$\rho \ddot{u} = c_{11} \frac{\partial^2 u}{\partial x^2} \quad (\text{A.8})$$

where $c_{11} = \frac{k}{a}$. Here, c_{11} is an elastic modulus that quantifies the force per unit area in the x-direction in response to deformation along the same axis. The elastic energy is given by

$$E = \frac{1}{2} c_{11} \varepsilon_{11}^2 \quad (\text{A.9})$$